

**UNIFORMITY OF AIRFLOW IN AUTOMOTIVE AIR
FILTER TEST HOUSINGS AND ITS EFFECTS
ON THE EFFICIENCY OF
FIBROUS FILTERS**

By

ROBERT A. NEWMAN

Bachelor of Science

Oklahoma State University

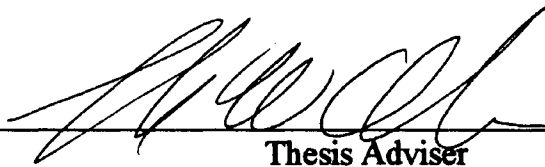
Stillwater, Oklahoma

1990

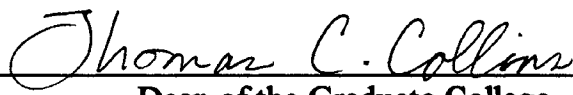
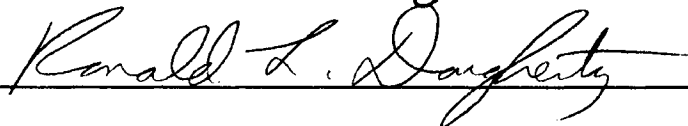
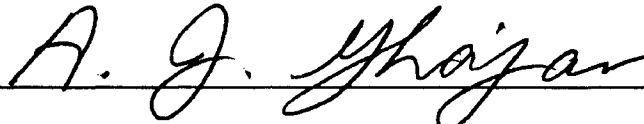
Submitted to the Faculty of the
Graduate College of the
Oklahoma State University
in partial fulfillment of
the requirements for
the Degree of
MASTER OF SCIENCE
December, 1994

**UNIFORMITY OF AIRFLOW IN AUTOMOTIVE AIR
FILTER TEST HOUSINGS AND ITS EFFECTS
ON THE EFFICIENCY OF
FIBROUS FILTERS**

Thesis Approved:



Thesis Adviser



Dean of the Graduate College

ACKNOWLEDGMENTS

I would like to thank my major adviser, Dr. F.W. Chambers, for his kind help, constructive guidance, advice, and support with this project and throughout my two years as a graduate student at Oklahoma State University. I would especially like to thank him for his help in securing the interview that led to my present position. I would also like to thank Dr. R.L. Dougherty for his very helpful advice and encouragement during my first few months back to school and his continued help throughout my career as a graduate student. My sincere appreciation also extends to Dr. A.J. Ghajar whose guidance, assistance, and encouragement has been invaluable.

Sincere thanks goes to my colleague Faqiu Liang for his friendship and help with this project. I would also like to thank my other colleagues R.D. Sabnis, M. Haldhani, R. Duran, C. Tebbutt, B. Natarajan, and Q. Cai who were all quite helpful with this project.

The financial support provided by Purolator Products, Inc. and the Oklahoma Center for the Advancement of Science and Technology (OCAST) is greatly appreciated. I would like to thank Dr. G. Ferrell and all those at Purolator Products for their help and insight into the world of automotive air filtration.

I would also like to give a very special thank you to my wife, Kathy, for her love, encouragement, and patience throughout my studies and my life. Thanks go to my parents, Bob and Pat Newman, and Kathy's parents, Robert and Josephine Artlip, for their support.

TABLE OF CONTENTS

Chapter	Page
I. INTRODUCTION	1
1.1 BACKGROUND	1
1.2 THE SAE STANDARD AIR CLEANER TEST CODE (J726) ..	2
1.2.1 <i>Uniformity of air flow in the universal panel filter test housing</i>	3
1.3 FIBROUS FILTRATION THEORY	3
1.3.1 <i>Collection efficiency of a fibrous filter bed</i>	5
1.3.2 <i>Mechanisms of collection by a single fiber</i>	7
1.3.3 <i>Kuwabara flow field around a cylinder</i>	9
1.3.4 <i>Deposition of particles on a cylindrical collector by interception</i>	11
1.3.5 <i>Deposition of particles on a cylindrical collector by inertial impaction and interception</i>	13
1.3.6 <i>Empirical formulæ for inertial interception and impaction</i>	18
1.3.7 <i>Independence of interception and impaction</i>	19
1.3.8 <i>Air velocity inside pleated filter media</i>	24
1.3.9 <i>Adhesion of particles to fiber surfaces</i>	25
1.3.10 <i>Previous work on filtration efficiency and the J726 housing</i>	30
1.3.11 <i>Measured particle number density in the prototype housing and the J726 housing</i>	31
1.4 CURRENT STUDY	32
II. EXPERIMENTAL SETUP FOR VELOCITY MEASUREMENTS AND FLOW VISUALIZATIONS	34
2.1 VELOCITY MEASUREMENTS	36

Chapter	Page
2.1.1 <i>Laser Doppler velocimeter basics</i>	36
2.1.2 <i>Laser Doppler velocimeter setup parameters</i>	40
2.1.3 <i>Equipment list</i>	42
2.1.4 <i>Experimental setup and procedure</i>	46
2.2 FLOW VISUALIZATIONS	54
2.2.1 <i>Laser sheet lighting of water particles</i>	54
2.2.2 <i>Tufts</i>	55
III. RESULTS AND DISCUSSION OF LASER DOPPLER VELOCITY MEASUREMENTS AND FLOW VISUALIZATIONS	56
3.1 LASER DOPPLER VELOCIMETER MEASUREMENTS	56
3.1.1 <i>Two-dimensional representations of velocity measurements</i>	57
3.1.2 <i>Comparison of prototype housing data with J726 housing data in a two-dimensional format</i>	60
3.1.3 <i>Three-dimensional representations of velocity measurements</i>	63
3.1.4 <i>Comparison of prototype housing data with J726 housing data in a three-dimensional format</i>	73
3.1.5 <i>Turbulence intensities near the filter</i>	74
3.2 FLOW VISUALIZATIONS	78
3.2.1 <i>Laser sheet flow visualization</i>	78
3.2.2 <i>Flow visualization with tufts</i>	79
3.3 SUMMARY OF RESULTS	79
IV. FILTRATION EFFICIENCIES	80
4.1 EFFICIENCIES OF PLEATED AIR FILTERS	80

Chapter	Page
4.1.1 Assumptions	80
4.1.2 Single fiber efficiencies within pleated fibrous filter media	81
4.1.3 Bed efficiencies across pleated fibrous filter media	83
4.1.4 Comparison of elemental bed efficiencies in the prototype housing to those in the J726 housing	86
4.1.5 Overall filter efficiency comparisons	92
4.1.6 Adhesion considerations	93
4.1.7 Particle number distribution considerations	95
4.2 SUMMARY	97
V. CONCLUSIONS AND RECOMMENDATIONS	99
5.1 CONCLUSIONS	99
5.2 RECOMMENDATIONS FOR FUTURE WORK	100
REFERENCES	101
APPENDICES	105
A COMPARISON OF AEROSOL PARTICLE GENERATION TECHNIQUES AND NUMBER OF SAMPLES PER RUN	105
B SYMMETRY OF VELOCITY PROFILES IN THE PROTOTYPE HOUSING AND ITS RELATIONSHIP TO FILTER PLEAT CURVATURE AND HOUSING EXIT LOCATIONS	108
C COMPUTER PROGRAM FOR THE CALCULATION OF FIBROUS FILTER PARTICLE COLLECTION EFFICIENCIES	110
D FILTER SPECIFICATIONS	118
E TEST DUST SPECIFICATIONS	119

LIST OF TABLES

Table	Page
4.1 Overall filter efficiencies calculated for the prototype and J726 housing velocity distributions and a uniform velocity distribution, particle number distribution assumed constant	92
4.2 Overall filter efficiencies calculated for the prototype and J726 housing velocity distributions and a uniform velocity distribution, accounting for non-perfect adhesion of particles to fiber surfaces, particle number distribution assumed constant	94
4.3 Overall filter efficiencies calculated for the prototype and J726 housing velocity distributions and a uniform velocity distribution, using Equation (4.1) for particle number distribution values	97
D.1 Filter specifications	118
E.1 Test dust specifications, particle size distribution by volume	119
E.2 Test dust specifications, particle size distribution by weight	119

LIST OF FIGURES

Figure	Page
1.1 SAE J726 panel filter test housing (SAE 1987)	2
1.2 Penetration of mono-disperse particles through a simple filter as a function of particle size (Brown 1993)	4
1.3 Section of a filter illustrating the scale of particles and fibers (Brown 1993)	4
1.4 Particle capture mechanisms: A, particle capture by interception; B, particle captured by inertial impaction; C, particle captured by diffusional deposition. (Brown 1993)	8
1.5 The Kuwabara flow field (Flagan & Seinfeld 1988)	11
1.6 Geometry of collection by inertial impaction (Flagan & Seinfeld 1988)	14
1.7 Collection of a particle by impaction and inertial interception	20
1.8 Approximate and exact (Flagan & Seinfeld 1988), and Eq. (1.42) collection efficiencies for inertial impaction and interception by a cylinder	23
1.9 Comparison of empirical filtration efficiency methods with theory	23
1.10 Filter pleat geometry	25
1.11 Sphere attached to a plane by capillary forces (Brown 1993)	27
1.12 Distribution of adhesion energies of quartz particles deposited at a filtration velocity of 0.42 m/s, on polyamide fibers; (1) 15.1 μm particles; (2) 10.3 μm particles; (3) 8.3 μm particles; (4) 5.1 μm particles (Brown 1993)	29
2.1 Shallow angle prototype panel filter test housing	35
2.2 Example of a Doppler burst signal	37
2.3 Schematic of the discrete Fourier transform method applied to a one bit sample (Aerometrics 1992)	38
2.4 Diagram of a particle passing through probe volume	41
2.5 (a) an example of a vertical Doppler burst signal with pedestal removed and (b) a horizontal Doppler burst signal with pedestal removed	41
2.6 Schematic of the Laser Doppler Velocimetry system	48
2.7 Schematic of airflow through test housing and related equipment	49

Figure	Page
2.8 Velocity measurement planes	50
2.9 Velocity measurement grid	51
2.10 Sign convention and coordinate system for velocity measurements	52
2.11 Diagram of relative positions of filter housing and transceiver during tests ..	53
3.1 Comparison of axial and transverse velocity profile slices in prototype housing at $y = 0$	59
3.2 Comparison of the prototype housing axial velocity data with axial velocity data from the J726 housing, 13 mm upstream of the filter	61
3.3 Comparison of the prototype housing transverse velocity data with transverse velocity data from the J726 housing, 13 mm upstream of the filter	62
3.4 Axial velocity distribution 102 mm upstream of the filter	67
3.5 Transverse velocity distribution 102 mm upstream of the filter	68
3.6 Axial velocity distribution 51 mm upstream of the filter	69
3.7 Transverse velocity distribution 51 mm upstream of the filter	70
3.8 Axial velocity distribution 13 mm upstream of the filter	71
3.9 Transverse velocity distribution 13 mm upstream of the filter	72
3.10 Axial velocity distribution in prototype housing 13 mm upstream of the filter	75
3.11 Axial velocity distribution in J726 housing 13 mm upstream of the filter	75
3.12 Transverse velocity distribution in prototype housing, 13 mm upstream of the filter	76
3.13 Transverse velocity distribution in J726 housing, 13 mm upstream of the filter	76
3.14 Axial Turbulence Intensity 13 mm upstream of filter for J726 housing (Sabnis 1993)	77
3.15 Axial turbulence intensity 13 mm upstream of the filter for the prototype housing	77
3.16 Laser sheet lighting of water particles in the prototype housing	78
4.1 Single fiber efficiencies, prototype housing, 5 μm particles	82
4.2 Single fiber efficiencies, J726 housing, 5 μm particles	82

Figure	Page
4.3 Elemental efficiencies for filter AF3192, prototype housing, 1 μm particle size	84
4.4 Elemental efficiencies for filter AF3192, prototype housing, 2.5 μm particle size	84
4.5 Elemental efficiencies for filter AF3192, prototype housing, 5 μm particle size	85
4.6 Elemental efficiencies for filter AF3192, prototype housing, 9.2 μm particle size	85
4.7 Elemental efficiencies for filter AF3192, prototype housing, 1 μm particle size	88
4.8 Elemental efficiencies for filter AF3192, J726 housing, 1 μm particle size	88
4.9 Elemental efficiencies for filter AF3192, prototype housing, 2.5 μm particle size	89
4.10 Elemental efficiencies for filter AF3192, J726 housing, 2.5 μm particle size	89
4.11 Elemental efficiencies for filter AF3192, prototype housing, 5 μm particle size	90
4.12 Elemental efficiencies for filter AF3192, J726 housing, 5 μm particle size	90
4.13 Elemental efficiencies for filter AF3192, prototype housing, 9.2 μm particle size	91
4.14 Elemental efficiencies for filter AF3192, J726 housing, 9.2 μm particle size	91
4.15 Comparison of elemental efficiencies with consideration and without consideration of the effects of adhesion along the y-centerline of the prototype housing for several different particle sizes	95
4.16 Particle concentration upstream of filter (prototype housing, 0.966 μm particles)	96
A.1 Reliability of data, prototype housing, 13 mm upstream of center of the filter, using 2 ultrasonic humidifiers as particle generators	106

Figure	Page
A.2 Reliability of data, prototype housing, 13 mm upstream of center of the filter, using TSI atomizer loaded with 100 ppm PSL suspension as particle generator	106
A.3 Reliability of data, prototype housing, 13 mm upstream of center of the filter, using TSI atomizer loaded with 200 ppm PSL suspension as particle generator	107
B.1 Symmetry of data, 200 ppm PSL suspension, TSI atomizer, y-centerline prototype housing, 13 mm upstream of filter	109

NOMENCLATURE

a_e	elemental area (m^2)
a_0, b_0, c_0	adhesive probability constants
A_1	Hamaker constant
b	x position where $u_x = u_\infty$ (m)
c	solid fraction of fibrous media, or the packing density
C	local particle concentration ($\#/m^3$)
C_e	slip correction factor
C_e	elemental particle number density ($\#/m^3$)
d	distance between interference fringes (m)
D_p	particle diameter (m)
D_f	fiber diameter (m)
f	frequency (Hz)
F	adhesive force (N)
h	filter depth (m)
i	the imaginary number
I_p	interception parameter

k	a counter
Kn	Knudsen number
Ku	Kuwabara hydrodynamic factor
L_f	total length of fibers in bed (m)
n	discrete frequency
N	total number of samples
N_p	particle flux (#/m²/s)
p	pitch of filter (m)
P_e	elemental penetration
q	particle charge (coulomb)
r, θ	radial and tangential cylindrical coordinates (m)
R_s	radius of the particle surface asperity that is closest to the fiber (m)
Re_f	Reynolds number based on fiber diameter
Re_p	dimensionless number similar to Reynolds number based on particle density
R_f	fiber radius (m)
R_p	particle radius (m)
r'	dimensionless radial coordinate

St	Stokes number
t	time (s)
t*	dimensionless time based on τ
u	fluid velocity (m/s)
u_r, u_θ	radial and tangential velocity components (m/s)
u_x, u_y	cartesian velocity components (m/s)
u₀	axial aerosol velocity upstream of filter (m/s)
u_∞	mean aerosol velocity in the filter (m/s)
v	velocity (m/s)
v	particle velocity (m/s)
v₀	transverse aerosol velocity upstream of filter (m/s)
V_{ip}	aerosol velocity inside pleat (m/s)
V_{op}	aerosol velocity outside pleat (m/s)
x, y	cartesian coordinates
x(k)	complex, filtered, sampled data
y₀	distance between the center line of a fiber and the streamline below which all particles are collected by inertial impaction (m)

y_1	distance between the center line of a fiber and the streamline below which all particles are collected by inertial impaction and interception (m)
Y	distance between the center line of a fiber and the streamline below which all particles are collected by interception (m)
z_0	distance between a particle and a fiber (m)
z_1, z_2	dimensionless cartesian coordinates based on fiber diameter
γ	Euler's constant
γ_0	adhesive probability
δ	charge density depth (m)
ϵ_0	permittivity of free space
η	single fiber particle collection efficiency; fiber collision efficiency
η_1, η_2	two independent collection efficiencies
η_b	overall particle collection efficiency of filter bed
η_e	elemental particle collection efficiency
η_i	single fiber particle collection efficiency by inertial impaction and interception
η_I	single fiber particle collection efficiency by inertial impaction
η_R	single fiber particle collection efficiency by interception
λ	mean free path of air (m)

μ	dynamic viscosity of air (Pa·s)
ρ	density of air (kg/m ³)
ρ_p	density of aerosol particle (kg/m ³)
τ	the characteristic time for a particle to approach motion (s)
τ_T	surface tension (N/m)
Ψ	stream function
Ψ'	dimensionless stream function based on fiber radius
$\bar{\Psi}$	dimensionless stream function based on fiber diameter

CHAPTER I

INTRODUCTION

1.1 BACKGROUND

The cleaning of induction air is critical to the endurance and performance of automotive engines. Automotive engine air cleaners come in a variety of forms. Most commonly, they consist of a non-woven, cellulose (paper) fibrous mat that is pleated then mounted in either two circular end-seals to form a cylindrical filter or a single rectangular end-seal to form a panel filter. These filters must provide a very high dust removal efficiency and dust holding capacity while introducing as little flow restriction as possible into the induction system. This must be accomplished with the added burdens of variable flow rates, high aerosol velocities, and non-uniform particle size distributions and concentrations.

The efficiency of a fibrous filter is a strong function of the velocity of the fluid passing through the filter. A non-uniform velocity profile across the face of the filter creates areas of varying efficiency in the filter. The housing that the filter is mounted in is the dominant factor determining the flow field that the filter will encounter. The testing of automotive engine air filters is governed by the Society of Automotive Engineers' (SAE) *J726 Air Cleaner Test Code*. Test code J726 specifies standard test housings for both cylindrical and panel air filter cartridges. This thesis considers the pleated paper air filter in general and the panel air filter specifically.

1.2 THE SAE STANDARD AIR CLEANER TEST CODE (J726)

To maintain a uniformity of standards for testing the pressure drop, efficiency, and dust holding capacity characteristics of automotive filters, the Society of Automotive Engineers have produced the "Air Cleaner Test Code," J726. This code governs the testing of dry and oil bath type air filters. Test equipment and procedures for the test are specified in J726. Figure 1.1 is a diagram of the universal panel filter test housing.

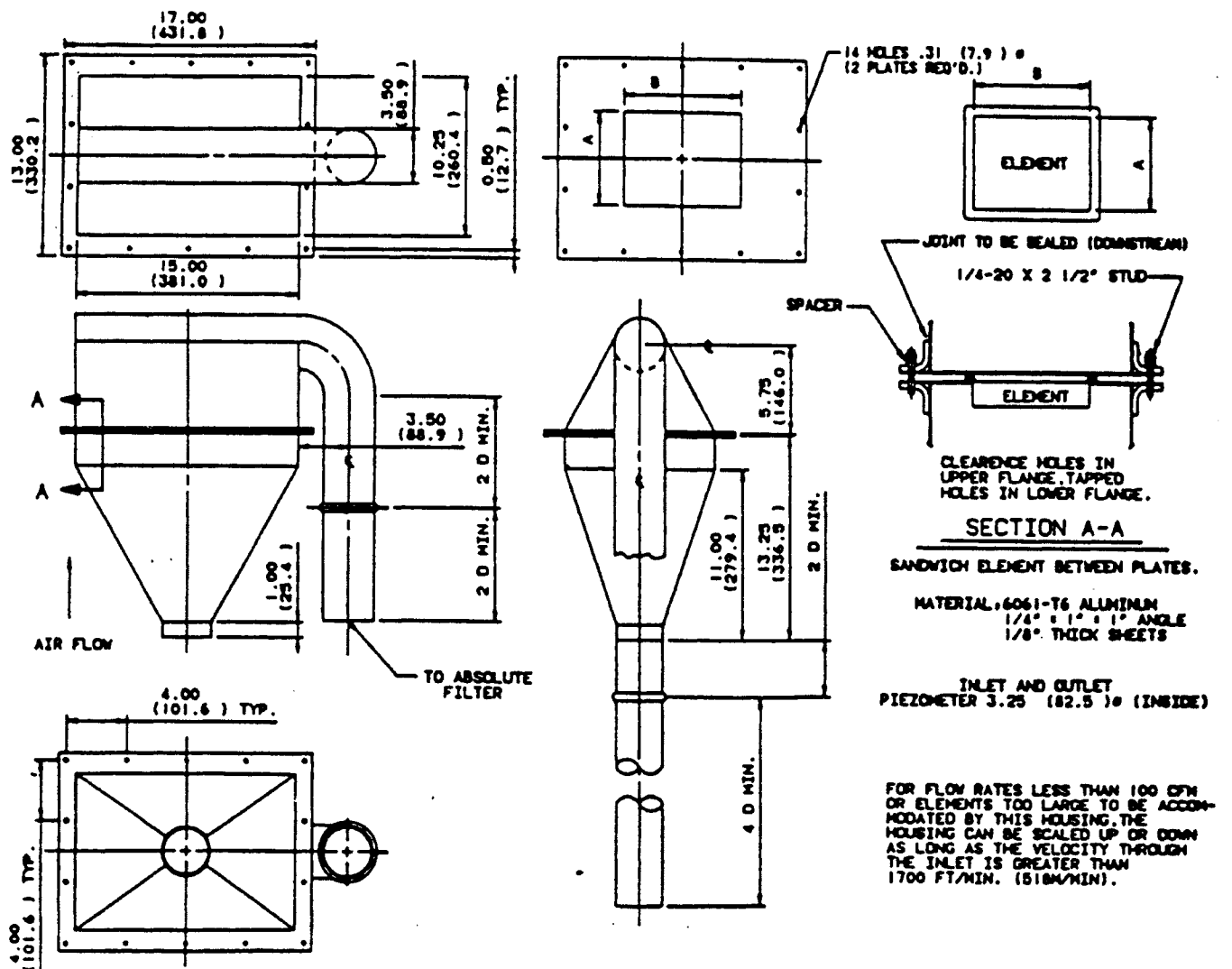


Fig. 1.1 SAE J726 panel filter test housing (SAE 1987)

1.2.1 Uniformity of air flow in the universal panel filter test housing

Sabnis (1993), using laser doppler velocimetry and flow visualizations, concluded that the universal panel filter test housing specified in SAE J726 operates like a diffuser in the jet flow regime, providing strongly recirculating separated flow at the walls of the housing. Filters tested in the housing will experience very non-uniform flow that resembles that of an impinging jet.

1.3 FIBROUS FILTRATION THEORY

As described by Brown (1993), fibrous filters, although performing a similar function to a net, do not work in the same fashion as a net. A net works as a sieve capturing 100% of the particles that are larger than the size of the holes in the net. Two identical nets in series will perform no better than one net, this means that the performance of a net can be studied by looking at the surface alone. This process is called *surface capture* or *surface filtration*. Capture of particles in a fibrous filter occurs throughout the depth of the filter, a thick fibrous filter is therefore more efficient than a thin one, but no fibrous filter is 100% efficient.

A fibrous filter can be thought of as a large number of layers with each layer being populated with fibers. Even if one layer has only a very small capture efficiency, the filter as a whole can perform quite well. This process of particle capture throughout the filter is termed *depth filtration*. Depth filters are able to capture particles that are too small to be sieved out. Particles of only a few microns in diameter are efficiently captured, as shown in Figure 1.2, by filters consisting of sparsely packed fibers 20 μm in diameter. The filter structure, shown in Figure 1.3, is so open that even a 10 μm particle would be very

unlikely to touch more than one fiber at a time. The capture of a particle, therefore, involves only one fiber.

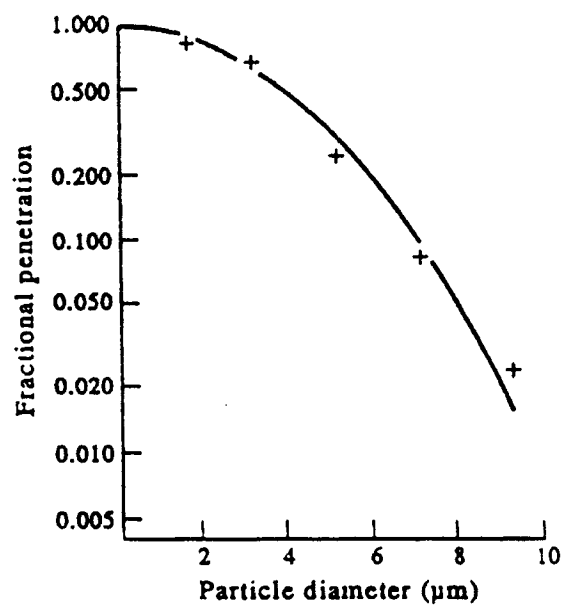


Fig. 1.2 Penetration of mono-disperse particles through a simple filter as a function of particle size (Brown 1993)

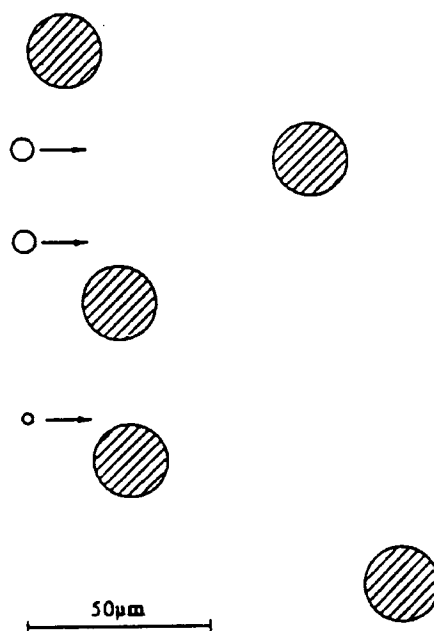


Fig. 1.3 Section of a filter illustrating the scale of particles and fibers (Brown 1993)

Fibrous filters have been modeled in several different ways that are described by Davies (1973). The most common method used to describe the fibrous filter is the *single fiber theory*. This method regards the filter as a certain length of a cylindrical obstacle to the flow. A fibrous filter could also be modeled as an *isolated fiber*. Using the isolated fiber method, the effects of surrounding fibers on the collection efficiency of a given fiber are neglected; but with the single fiber method, these effects are not neglected.

1.3.1 Collection efficiency of a fibrous filter bed

A fibrous filter, as described by Flagan & Seinfeld (1988), can be thought of as a loosely packed assemblage of single cylinders. It is assumed that fibers surrounding an individual fiber will affect the efficiency of that fiber. To compute the efficiency of a fiber bed, the efficiency of a single fiber can be multiplied by the number of fibers per unit volume of the bed. The solid fraction, c , or packing density, of the filter bed can be expressed in terms of the fiber diameter, D_f , and the total length of fibers in the bed, L_f , as:

$$c = \frac{\pi D_f L_f}{4} \quad (1.1)$$

The gas velocity inside the filter is greater than the velocity approaching the filter due to the volume change caused by the filter fibers. The mean velocity in the filter can be related to the upstream velocity by:

$$u_\infty = \frac{u}{1 - c} \quad (1.2)$$

where u is the upstream velocity.

The overall efficiency of the bed is given by:

$$\eta_b = 1 - \exp\left[-\frac{4c\eta h}{\pi(1-c)D_f}\right] \quad (1.3)$$

where η is the single fiber efficiency, h is the depth of the filter bed, and D_f is the diameter of the filter fiber.

If the filter is broken into many different elements all with their own velocity, u_{∞} , the elemental mean velocity for the given element, then Equation (1.3) can be thought of as the elemental efficiency, in that it will be appropriate for a given element only. In that case the elemental efficiency, η_e is the same as η_b . The elemental penetration can then be given as, Sabnis (1993):

$$P_e = 1 - \eta_e \quad (1.4)$$

The overall efficiency of the filter can be given as one minus the weighted average of the elemental penetrations, using the particle number density above the element, the area of the element, and the measured elemental velocity as the weighting functions.

$$\eta_f = 1 - \frac{\sum_{i=1}^n [P_e(C_e a_e u_{\infty})]}{\sum_{i=1}^n [C_e a_e u_{\infty}]} \quad (1.5)$$

where C_e is the particle number density, number of particles per meter cubed, over an elemental area upstream of the filter, and a_e is the area of the element in question.

1.3.2 Mechanisms of collection by a single fiber

There are three main mechanisms, as described by Flagan & Seinfeld (1988) and illustrated in Figure 1.4, by which a single fiber can act as a filter:

1. The *Brownian diffusion* mechanism of fibrous filtration treats particles like they were molecules in a diffusive concentration gradient. Due to random motion as particles are carried past the fiber by the aerosol flow, some particles will come into contact with the fiber through Brownian diffusion; random motion caused by collisions of submicron particles with surrounding molecules. By removing a few particles from the air stream a concentration gradient is created that acts as a driving force, increasing the rate of deposition over that which would occur without Brownian motion. This removal mechanism is most important for very small particles ($<1 \mu\text{m}$) transported in a very low velocity flow field. Submicron particles are often called diffusive particles for this reason.
2. *Interception* occurs when a particle, following a streamline, is large enough that it comes into contact with the fiber. The particle's path does not deviate from the streamline. If the streamline that the particle is following is within one particle radius, or $D_p/2$, of the fiber surface, the particle is collected. Thus if the particle surface touches the fiber surface, then the particle is collected. In the analysis of this mechanism, particles are treated as though they have size but no mass.
3. *Inertial impaction* occurs to a particle of significant mass that is unable to follow a streamline as it rapidly curves around a fiber. Due to its own momentum, the

particle deviates from the streamline and strikes the fiber. Particles are treated as though they have mass but no size.

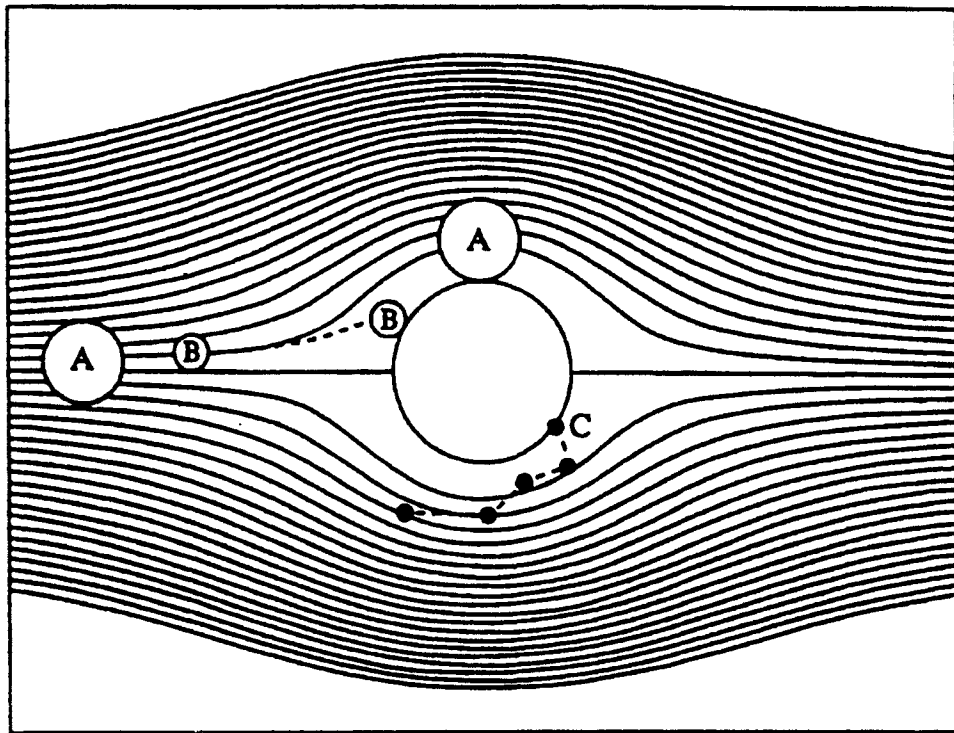


Fig. 1.4 Particle capture mechanisms: A, particle capture by interception; B, particle captured by inertial impaction; C, particle captured by diffusional deposition. (Brown 1993)

Collection could also occur by electrostatic attraction between the particle and the fiber when either the particle or the fiber or both are electrostatically charged. This is usually not the case, unless a charge is deliberately introduced, and is not considered here.

Many authors analyze the mechanisms of collection separately and then combine the individual efficiencies to get an overall efficiency. Suppose that we have two independent collection mechanisms giving us collection efficiencies η_1 and η_2 . The probability that a particle will escape mechanism 1 is $(1-\eta_1)$ and the probability that it will escape

mechanism 2 is $(1-\eta_2)$. The probability that it will escape collection from either mechanism is $(1-\eta_1)(1-\eta_2)$. Then the probability that the particle will be collected is:

$$\eta = 1 - (1 - \eta_1)(1 - \eta_2) \quad (1.6)$$

or

$$\eta = \eta_1 + \eta_2 - \eta_1\eta_2 \quad (1.7)$$

In many cases one collection mechanism will be dominant over another one in a particular particle size range. In that case Equation (1.7) is often approximated as $\eta = \eta_1 + \eta_2$.

1.3.3 Kuwabara Flow Field around a Cylinder

One parameter that is important to the flow field is the Reynolds number, based on cylinder (or fiber) diameter,

$$\text{Re}_f = \frac{D_f u_\infty \rho}{\mu} \quad (1.8)$$

where ρ is the density of air, and μ is the dynamic viscosity of air. For typical fibrous filter flow, the Reynolds number is usually on the order of one or smaller.

Kuwabara (1959) proposed a flow field in which fibers are modeled as infinitely many circular cylinders that are distributed at random and homogeneously in a viscous flow at small Reynolds numbers. To simulate the condition of random and homogeneous distribution of cylinders, Kuwabara used a model in which each cylinder is surrounded by an imaginary coaxial cylinder, or cell, with a radius determined by requiring the ratio of cell fluid to fiber volume to be the same ratio as the fluid to fiber ratio of the fibrous

medium. On the surface of the cell, both the normal fluid velocity and the vorticity vanish.

The Kuwabara flow field solution is:

$$u_r = \frac{u_\infty}{2Ku} \left[1 - 2 \ln \frac{2r}{D_f} - c - \frac{D_f^2}{4r^2} \left(1 - \frac{c}{2} \right) - \frac{2cr^2}{D_f^2} \right] \cos \theta \quad (1.9)$$

$$u_\theta = \frac{u_\infty}{2Ku} \left[1 - 2 \ln \frac{2r}{D_f} + c - \frac{D_f^2}{4r^2} \left(1 - \frac{c}{2} \right) - \frac{6cr^2}{D_f^2} \right] \sin \theta \quad (1.10)$$

where r and θ are the cylindrical coordinates, and Ku , the Kuwabara hydrodynamic factor is given by

$$Ku = c - \frac{3}{4} - \frac{c^2}{4} - \frac{1}{2} \ln c \quad (1.11)$$

The stream function for this velocity field is

$$\Psi = \frac{u_\infty r}{2Ku} \left[1 - 2 \ln \frac{2r}{D_f} - c - \frac{D_f^2}{4r^2} \left(1 - \frac{c}{2} \right) + \frac{2cr^2}{D_f^2} \right] \sin \theta \quad (1.12)$$

Streamlines of the Kuwabara flow field, expressed as $\Psi = \Psi/u_\infty D_f$, are shown in Figure 1.5.

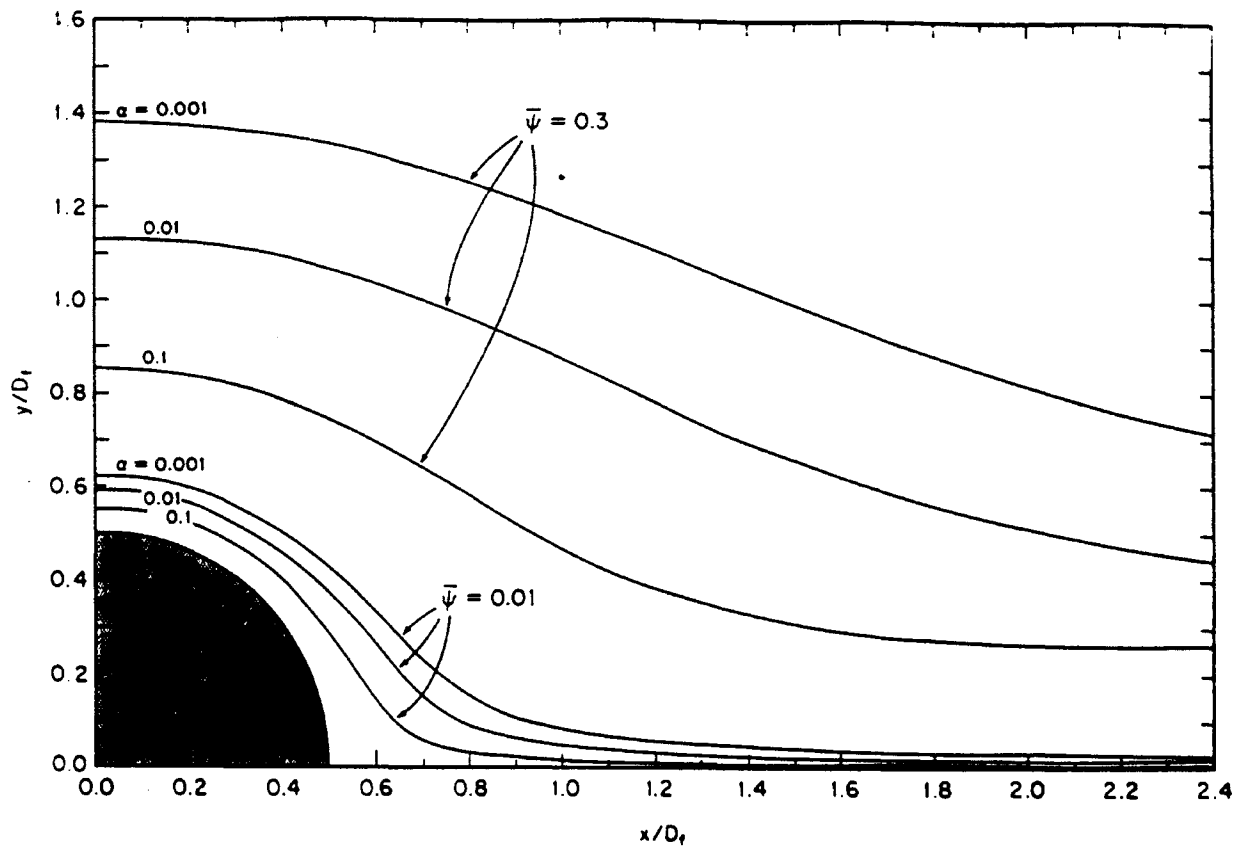


Fig. 1.5 The Kuwabara flow field (Flagan & Seinfeld 1988)

1.3.4 Deposition of particles on a cylindrical collector by interception

Collection by interception occurs when the particle has a finite size. If the particle center approaches a fiber within a distance of $D_p/2$, collection occurs. Lee and Liu (1982b) define the single fiber efficiency due to interception as

$$\eta_R = \frac{Y}{D_f/2} \quad (1.13)$$

or

$$\eta_R = \frac{\Psi}{u_\infty(D_f/2)} \quad (1.14)$$

where Y is the distance between the center line of the fiber and the streamline below which all particles are collected. By substituting the Kuwabara flow equation for stream function into Equation (1.13), they deduced

$$\eta_R = \frac{1+I_p}{2Ku} \left[2 \ln(1+I_p) - 1 + c + \left(\frac{1}{1+I_p} \right)^2 \left(1 - \frac{c}{2} \right) - \frac{c}{2}(1+I_p)^2 \right] \quad (1.15)$$

Where I_p is the interception parameter which is given by

$$I_p = \frac{D_p}{D_f} \quad (1.16)$$

By introducing the dimensionless quantities $r' = r/R_f$ and $\Psi' = \Psi/u_\infty R_f$, the Kuwabara stream function can be given as

$$\Psi' = \left(\frac{r'}{2Ku} \right) \left[\left(2 \ln r' - 1 + \frac{1}{r'^2} \right) - c \left(-1 + \frac{1}{2r'^2} + \frac{1}{2} r'^2 \right) \right] \sin \theta \quad (1.17)$$

The series expansion for $\ln r'$, valid for $r' > 1/2$, is

$$\ln r' = \frac{r'-1}{r'} + \frac{1}{2} \left(\frac{r'-1}{r'} \right)^2 + \frac{1}{3} \left(\frac{r'-1}{r'} \right)^3 + \dots \quad (1.18)$$

Using the first two terms as an approximation, gives

$$\Psi' \cong \frac{r'}{2Ku} \left[\frac{2(r'-1)^2}{r'^2} - c \frac{(r'^2-1)^2}{2r'^2} \right] \sin \theta \quad (1.19)$$

Note that r' has been assumed to be close to unity, therefore this approximation is only valid near the surface of the fiber. To make the expression for stream function even simpler, Equation (1.17) can be further approximated as

$$\Psi' \cong \frac{r'}{Ku} \left[\frac{(r' - 1)^2}{r'^2} - c \frac{(r' - 1)^2}{r'^2} \right] \sin \theta \quad (1.20)$$

assuming that $r' \sim 1$ and $c \sim 0$. The error for these approximations approaches zero as c approaches $1/3$. The velocity components can easily be obtained from the stream function.

By substituting Equation (1.19) into Equation (1.14), we can obtain an approximation for Equation (1.15) given by

$$\eta_R = \frac{1+c}{Ku} \frac{I_p^2}{1+I_p} \quad (1.21)$$

as presented by Lee & Liu (1982b).

1.3.5 Deposition of particles on a cylindrical collector by inertial impaction and interception

The mechanism of inertial impaction, as described by Flagan & Seinfeld (1988), results because particles with sufficient mass cannot follow the curvilinear motion of the fluid as it passes around the fiber. Instead, they tend to deviate from the streamline that they were following by taking a straighter path towards the fiber and in doing so strike the fiber. To analyze inertial impaction, trajectories of particles in the flow must be analyzed to determine from what upstream locations those particles that were collected originated.

Figure 1.6 shows the geometry of collection by inertial impaction. The trajectory of a particle initially at a distance y_1 is highlighted. The streamline passing through y_1 is the *limiting streamline*. All particles below y_1 will be collected by inertial impaction, and all particles above y_1 will escape collection. The particle trajectory through y_1 is the *limiting or critical trajectory*.

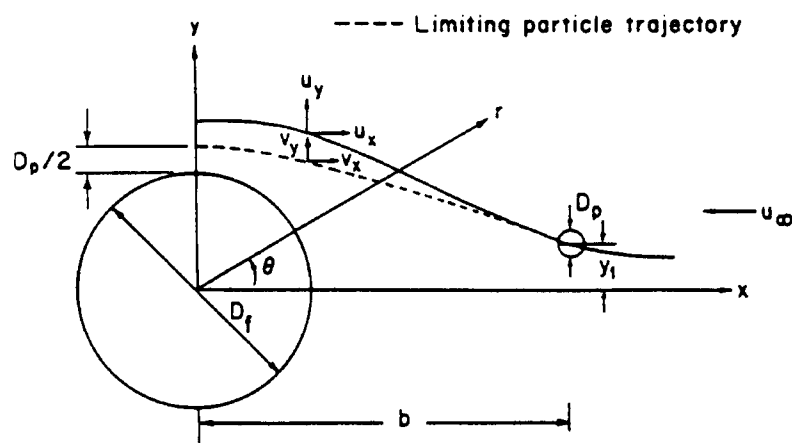


Fig. 1.6 Geometry of collection by inertial impaction (Flagan & Seinfeld 1988)

Once y_1 is determined, the collection efficiency is simply

$$\eta_I = \frac{2y_1}{D_f} \quad (1.22)$$

If the limiting trajectory is taken as that passing within a distance $D_p/2$ of the cylinder surface rather than a trajectory just touching the surface, then interception is automatically included in the analysis.

Mathematically the trajectory of a particle can be tracked by inserting the Kuwbara flow field velocities into the equation of motion of a particle. Following Flagan & Seinfeld (1988), the trajectory of particles in fibrous media can be developed. Neglecting external forces, the equation of motion for a particle is given by

$$\tau \frac{dv}{dt} = u - v \quad (1.23)$$

where u is the velocity of air, v is the particle velocity, and τ is the characteristic time for the particle to approach steady motion, and is given by

$$\tau = \frac{\rho_p C_c D_p^2}{18\mu} \quad (1.24)$$

Here ρ_p is the particle density, C_c is the slip correction factor, D_p is the particle diameter, and μ is the viscosity of air. C_c is approximated by

$$C_c = 1 + 1.257Kn \quad \text{for } R_p \gg \lambda \quad (1.25)$$

where $Kn = \frac{\lambda}{R_p}$ is the Knudsen number, R_p is the particle radius, and λ is the mean free path of air.

In cartesian coordinates Equation (1.23) becomes,

$$\tau \frac{d^2x}{dt^2} + \frac{dx}{dt} = u_x \quad (1.26)$$

$$\tau \frac{d^2 y}{dt^2} + \frac{dy}{dt} = u_y \quad (1.27)$$

to be solved with the initial conditions

$$x(0) = b \quad \frac{dx}{dt}_{t=0} = u_x(b, y_1) \quad (1.28)$$

$$y(0) = y_1 \quad \frac{dy}{dt}_{t=0} = u_y(b, y_1) \quad (1.29)$$

b is the x position where $u_x = u_\infty$ and is given by

$$b = \frac{D_f}{2\sqrt{c}} \quad (1.30)$$

The Kuwabara flow field can be given in cartesian coordinates as

$$u_x = -\frac{u_\infty Ku}{2} \left(\ln \left(\frac{4(x^2+y^2)}{D_f^2} \right) + c - c \frac{x^2+3y^2}{D_f^2/2} + \frac{y^2-x^2}{x^2+y^2} + \frac{D_f^2}{4} \left(1 - \frac{c}{2} \right) \frac{x^2-y^2}{(x^2+y^2)^2} \right) \quad (1.31)$$

$$u_y = \frac{u_\infty Ku}{2} \left[\frac{2xy}{x^2+y^2} - \frac{D_f^2 xy}{2(x^2+y^2)^2} \left(1 - \frac{c}{2} \right) - \frac{4cxy}{D_f^2} \right] \quad (1.32)$$

We can now put everything in dimensionless form by letting $z_1 = x/D_p$, $z_2 = y/D_p$, $t^* = t/\tau$,

and St be the Stokes number, which is given by

$$St = \frac{D_p^2 \rho_p C_c u_\infty}{9\mu R_f} \quad (1.33)$$

to obtain

$$\frac{d^2 z_1}{dt^{*2}} + \frac{dz_1}{dt^*} = -\frac{St}{2Ku} \left[\begin{aligned} &\ln\left(4(z_1^2 + z_2^2)\right) + c - 2c(z_1^2 + 3z_2^2) + \frac{z_2^2 - z_1^2}{z_1^2 + z_2^2} \\ &+ \frac{1}{4}\left(1 - \frac{c}{2}\right) \frac{z_1^2 - z_2^2}{(z_1^2 + z_2^2)^2} \end{aligned} \right] \quad (1.34)$$

$$\frac{d^2 z_2}{dt^{*2}} + \frac{dz_2}{dt^*} = \frac{St}{2Ku} \left[\begin{aligned} &\frac{2z_1 z_2}{z_1^2 + z_2^2} - \left(1 - \frac{c}{2}\right) \frac{z_1 z_2}{2(z_1^2 + z_2^2)^2} - 4cz_1 z_2 \end{aligned} \right] \quad (1.35)$$

to be solved subject to

$$z_1(0) = \frac{1}{2\sqrt{c}} \quad \frac{dz_1}{dt^*} \Big|_{t^*=0} = \frac{u_x(b, y_1)\tau}{D_f} \quad (1.36)$$

$$z_2(0) = \frac{y_1}{D_f} \quad \frac{dz_2}{dt^*} \Big|_{t^*=0} = 0 \quad (1.37)$$

The differential equations must be solved numerically using an ordinary differential equation solving algorithm such as the Runge-Kutta method.

1.3.6 Empirical formulæ for inertial interception and impaction

Landahl & Herrmann (1949) derived an empirical equation for inertial interception and impaction using the method described in section 1.3.5 but with velocity data calculated by Thom (1933) for viscous flow around an isolated cylinder rather than the Kuwbara flow field. This equation is thus an application of the isolated fiber theory of fibrous filtration. The equation is given by

$$\eta_I = \frac{St^3}{St^3 + 0.77St^2 + 0.22} \quad (1.38)$$

This equation was derived for $Re_f = 10$ and $I_p = 0$.

Suneja & Lee's (1974) equation for inertial interception is given by

$$\eta_I = \frac{1}{\left[1 + \left(1.53 - 0.23 \ln Re_f + 0.167(\ln Re_f)^2 \right) / St \right]^2} + \frac{2 I_p}{3 St} \quad (1.39)$$

The complete Navier-Stokes equations were solved numerically to find the flow field around a fiber. This flow field was then used with the trajectory method described in section 1.3.5 to obtain filtration efficiencies. Equation (1.34) was derived from the calculated efficiencies. This equation represents an isolated fiber approach to the solution of filtration efficiencies rather than the single fiber approach.

Ptak & Jaroszczyk (1990) proposed the following empirical equation

$$\eta_I = \frac{\left(St - 0.75Re_f^{0.2}\right)^2}{(St + 0.4)^2} \quad (1.40)$$

The flow field for this equation was found by numerically solving the Navier-Stokes equations for a circular cylinder set cross-wise to the flow. This is then another example of isolated fiber filtration theory. To account for the effects of neighboring fibers on the efficiency of any given fiber, Ptak & Jaroszczyk multiplied the isolated fiber efficiency by a simple function to give the single fiber efficiency.

$$\eta = \eta_I f(c) \quad (1.41)$$

where

$$f(c) = \frac{0.9}{c^{0.3}}$$

1.3.7 Independence of interception and impaction

The collection efficiency, as given by Equation (1.22), implies that any particle that is released within a distance y_1 of the centerline of the fiber will be captured by the fiber using an inertial interception and impaction model (see Figure 1.7).

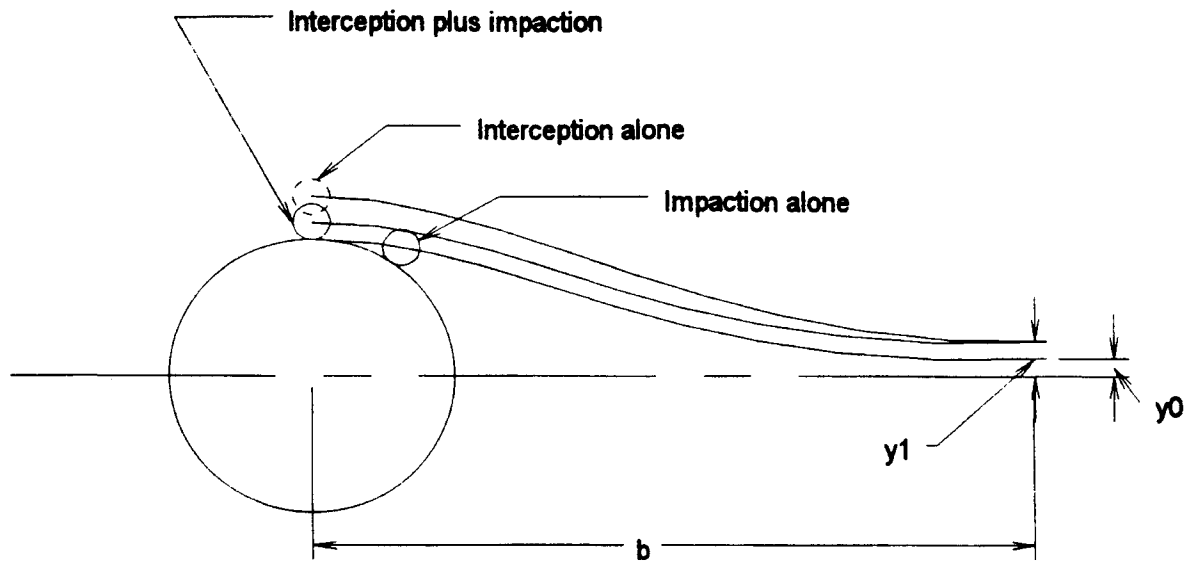


Fig. 1.7 Collection of a particle by impaction and inertial interception.

By using the impaction model alone, a particle released at a distance y_1 from the centerline of the fiber would not be captured in the model. In the impaction model, particles are treated as if they have mass but no size. Thus, a particle released from y_1 would not touch the fiber at all and would have to be released closer to the centerline of the fiber to be captured. This would lower the predicted efficiency. The interception model treats particles as if they have no mass but do have size. This model predicts that all particles follow the streamlines of the flow. If a particle does not deviate from the flow streamline that it has been following, it will not strike the surface of the fiber when released from the distance y_1 . The release point would again have to be moved closer to the centerline in order for the particle to be captured, thus lowering the predicted efficiency of the fiber.

Only by combining the inertial impaction and interception models can you obtain a model that includes capture of particles with both size and mass.

Sabnis (1993) combined Equation (1.21), developed for pure interception neglecting particle momentum, with Equation (1.38), developed for pure inertial impaction neglecting particle size, using Equation (1.6) to obtain this expression for the single fiber efficiency

$$\eta_I = 1 - \left(1 - \frac{1-c}{Ku} \frac{I_p^2}{1+I_p} \right) \left(1 - \frac{St^3}{St^3 + 0.77St^2 + 0.22} \right) \quad (1.42)$$

By using Equation (1.6) he assumed that collection by interception and collection by impaction are independent of each other. Is this really the case? Probably not. By studying the geometry of the situation in Figure 1.2, it is easy to see that interception and impaction are not easily separated. Particles that are released close enough to the centerline of the fiber that would be captured by either the impaction model or the interception model are actually counted twice. This increases the predicted efficiency of the combined models. It is also relatively obvious that those particles that would be captured by inertial interception are not included in this combined model. A particle whose mass and size are large enough that it would deviate from the streamline that it is following, when that streamline curves around the fiber, and touch the fiber, even when released from a distance from the centerline greater than y_0 but less than y_1 , will not be captured in this combined model. This decreases the predicted efficiency of the model. These increases in efficiency and decreases in efficiency combined in Sabnis' model could

possibly wash out and predict an efficiency similar to one that would be predicted by following the trajectory of a particle with size and mass in the Kuwabara flow field. Figure 1.8 shows just that. The method employed by Sabnis compares quite favorably to the trajectory and approximate methods used by Flagan & Seinfeld. Flagan & Seinfeld felt that it was appropriate to use their approximate method because the Kuwabara flow field is approximate in nature, and the maximum difference they found between their approximate method and the trajectory method was less than 75%. Using their logic, Eq (1.42) is a better approximation than Flagan & Seinfeld's; the difference between Equation (1.42) and the trajectory method is much less than 75%. I believe that it is satisfactory to use Equation (1.42), even though impaction and interception are not truly independent of each other. As seen in Figure 1.9 Sabnis' method, Equation (1.42), follows the theoretical method more closely than the empirical methods and will be used as the preferred model in this study.

1.3.8 Air velocity inside pleated filter media

As described by Brown (1993), pleating the filter media increases the available area of filtration media within a fixed volume, reducing the filtration velocity and the pressure drop for a fixed volume flow rate. Considering an element of width x and length y , as shown in Figure 1.10, the surface area of the media contained in the element can be given by

$$a_e = x \sqrt{\left(\frac{2hy}{p}\right)^2 + y^2} \quad (1.43)$$

If you assume that air flowing through the pleated filter media is uniformly distributed within the pleat, you can obtain the velocity of the fluid inside the media by means of continuity. Equating the total flow entering the element to the total flow entering the media contained within that element thus gives the velocity inside the media

$$u_\infty a_e = u_0 xy \quad (1.44)$$

or

$$u_\infty = \frac{u_0 xy}{a_e} \quad (1.45)$$

where u_0 is the axial velocity upstream of the filter.

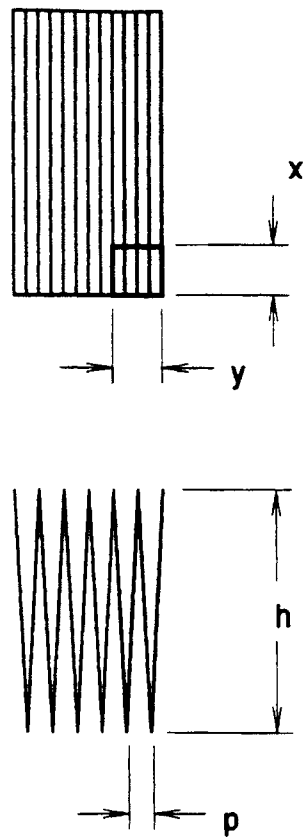


Fig. 1.10 Filter pleat geometry

1.3.9 Adhesion of particles to fiber surfaces

In the previous sections, a particle that struck or somehow found its way to the surface of a fiber was assumed to stick to the fiber and be separated from the air flow. This may not always be the case. If a particle strikes the fiber surface with sufficient velocity, it may rebound with reduced kinetic energy and be reentrained into the flow. This bouncing of particles at high air velocities will reduce the efficiency of the filter. Aerodynamic and possible other forces are at work on a particle when it strikes a fiber. These forces attempt to dislodge the particle from the fiber. At initial impact, the particle will also have the energy of restitution aiding in its attempt to free itself. The energy of restitution comes from the complex elastic/plastic process that occurs upon impact. Thus,

if a particle does not bounce upon impact with a fiber, it is very likely not to be reentrained because this is the point in time when the combined forces attempting to dislodge the particle from the fiber are at their greatest magnitude.

Particles could also be reentrained that have previously been stuck to a fiber. This may be unlikely due to the lack of available energy after impact, but a change in the velocity of the flow or direction of the flow will increase the chances of a particle becoming dislodged after attachment to a fiber.

There are three principle forces, as given by Löffler (1971) and Brown (1993), attaching particles to fibers:

- (a) van der Waals forces,
- (b) electrostatic forces as a result of excess charging,
- (c) and capillary forces in liquid bridges.

Van der Waals forces between atoms are caused by the fluctuating electric dipole moment present in an atom. The dipole induces an electric field that attracts the dipole in a neighboring atom. Normally van der Waals forces between macroscopic bodies are expressed with the Hamaker constant, A_1 .

$$F = \frac{A_1 R_p}{6z_0^2} \quad (1.46)$$

where R_p is the radius of the particle surface asperity that is closest to the fiber, and z_0 is the distance between the particle and the fiber. Electrostatic forces can occur when a

particle of radius, R_p , has taken a charge, q , before making contact with the fiber. The force of adhesion due to electrostatic charge is given by

$$F = \frac{q^2}{16\pi\epsilon_0 R_p \delta} \frac{\ln\left(1 + \frac{\delta}{z_0}\right)}{\left[\gamma + \frac{1}{2} \ln\left(\frac{2R_p}{z_0}\right)\right] \left[\gamma + \frac{1}{2} \ln\left(\frac{2R_p}{z_0 + \delta}\right)\right]} \quad (1.47)$$

Where δ is the depth at which the charge density falls to e^{-1} of that at the surface, ϵ_0 is the permittivity of free space, γ is Euler's constant, and z_0 is the distance between the particle and the fiber. Figure 1.11 shows a sphere attached to a plane by means of a liquid bridge.

If the angle of contact is zero, the force between them is given by

$$F = 4\pi\tau_T R_a \quad (1.48)$$

Where τ_T is the surface tension of the liquid bridge.

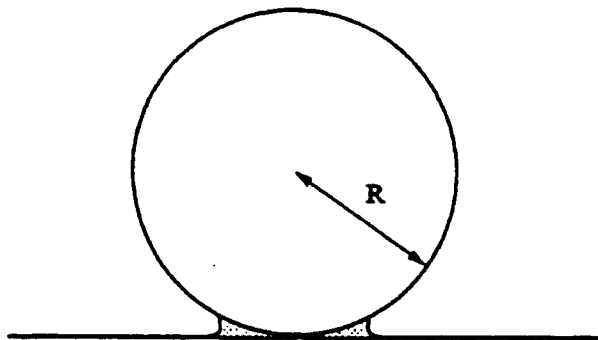


Fig. 1.11 Sphere attached to a plane by capillary forces (Brown 1993)

Löffler (1971) and Brown (1993) both show that the van der Waals force is most probably the most important adhesion force. The van der Waals force is ever present in the system and is a very strong short range force. Electrostatic forces have a longer range than that of the other adhesion forces and may induce adhesion while the van der Waals force maintains adhesion. Electric forces may not persist if both the particle and the filter media are conducting, thus leaving the van der Waals force to maintain the adhesion of a particle. Capillary forces vary with conditions and cannot be counted on to provide a strong adhesive force below a relative humidity of about 80%.

As shown in Figure 1.12, adhesion forces are stronger on larger particles, but the drag exerted on them is also greater. Large particles or agglomerates can be detached by a lower airflow than that which will detach smaller particles. The adhesion of particles to fibers is greater for particles that have been captured at a higher filtration velocity. This higher velocity does make bounce more likely, but those particles that are captured are more tightly bound to the fiber (Brown 1993).

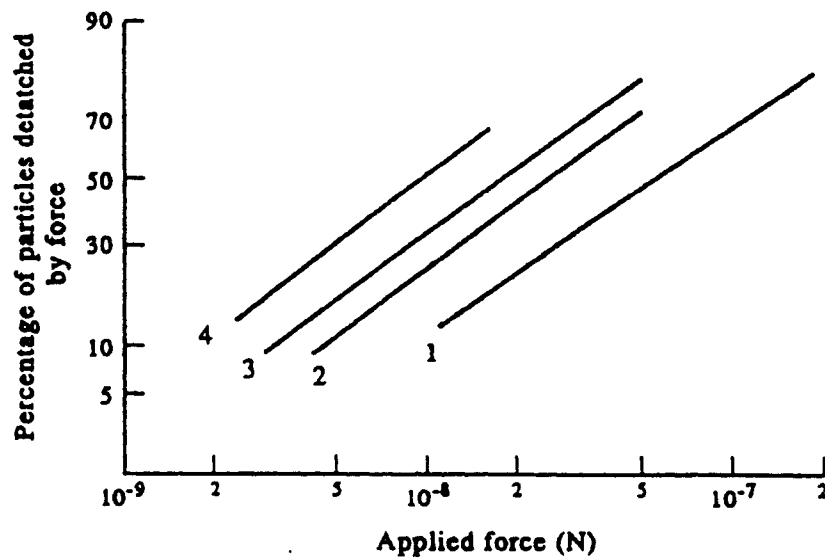


Fig. 1.12 Distribution of adhesion energies of quartz particles deposited at a filtration velocity of 0.42 m/s, on polyamide fibers; (1) 15.1 μm particles; (2) 10.3 μm particles; (3) 8.3 μm particles; (4) 5.1 μm particles (Brown 1993)

Ptak & Jaroszczyk introduced an empirical value for the probability of adhesion, γ_0 , in their 1990 paper. They felt that the collection efficiency of a fiber, η_I , is related to the collision efficiency, η , of the fiber and the adhesion efficiency of the fiber as given in Equation (1.49).

$$\eta_I = \eta\gamma_0 \quad (1.49)$$

where the adhesion efficiency is dependent upon the particle density and diameter, the air velocity and viscosity, and the diameter of the collecting fiber as illustrated in Equation (1.50).

$$\gamma_0 = f(\rho_p, d_p, u_\infty, \mu_0, d_f) \quad (1.50)$$

Using dimensional analysis, two dimensionless numbers were determined as

$$\text{St} = \frac{d_p^2 \rho_p u_\infty}{18 \mu_0 d_f} \quad \text{and} \quad \text{Re}_p = \frac{\rho_p d_p u_\infty}{\mu_0} \quad (1.51)$$

The adhesive probability factor should fall in a range of $0 \leq \gamma_0 \leq 1$. The expression given by Ptak and Jaroszczyk for the adhesive probability factor is

$$\gamma_0 = \frac{a_0}{(\text{St} \cdot \text{Re}_p)^{b_0} + c_0} \quad (1.52)$$

where $a_0 = c_0$ and $b_0 > 0$. The constants a_0 and b_0 were determined experimentally, and the final form of Equation (1.52) is given as Equation (1.53).

$$\gamma_0 = \frac{190}{(\text{St} \cdot \text{Re}_p)^{0.68} + 190} \quad (1.53)$$

Good correlation between experimental results and calculated values was found by Ptak when Equation (1.53) was used with a collection efficiency relation, Equation (1.40), in Equation (1.49).

1.3.10 Previous work on filtration efficiency and the J726 housing

Using laser doppler velocimetry with a transparent model of the J726 housing, Sabnis (1993) measured the flow field within the housing in several horizontal planes for two different sizes of panel filters. He found that the flow inside the housing was very turbulent, recirculating, and separated from the walls of the housing using either filter. LDV

measurements were backed up by flow visualizations in the housing that also show the flow to be highly recirculatory and separated from the walls of the housing. Examples of the flow field found by Sabnis in the J726 housing for the AF3192 filter can be found in Chapter 3 of this document. The filter receives a very non-uniform flow distribution with much higher velocities in the center of the filter than along the sides of the filter. By applying simple filtration theories to the measured aerosol velocities found in the housing, Sabnis was able to calculate the local initial filtration efficiencies for mono-disperse particles. His calculations predict that for larger particles the filtration efficiencies with a uniform flow distribution are better than that with non-uniform flow distributions. For very small particles the filtration efficiency was shown to decrease for the uniform flow distribution.

1.3.11 Measured particle number density in the prototype housing and the J726 housing

Liang et al. (1994) presented particle number density, or concentration, data collected from above and below the filter in the prototype housing, used in this study, and the J726 housing. With this data they were able to produce elemental particle collection efficiencies for the filter. They found that the overall filtration efficiency using either housing was higher than expected when using very small, 0.966 μm , particles and lower than expected when using larger, 5.3 μm , particles.

Sabnis (1993) offered several suggestions for particle distributions in filter housings. His first was a uniform particle number density distribution. This assumption says that the particle flux, N_p , or number of particles passing through a unit area per unit time, at the filter surface is related to the local particle concentration, C , by

$$N_p = Cu_0 \quad (1.54)$$

where, in this case, C is equal to a constant. It was also suggested that the particle concentration may be proportional to velocity. In this case C would not be constant but could be related to velocity as in

$$C = f(u_0) \quad (1.55)$$

A third assumption would be to represent the product of the particle concentration and the aerosol velocity as a constant. In this case C would be represented by

$$C = \frac{\text{const.}}{u_0} \quad (1.56)$$

Sabnis (1993) reasoned that this assumption was a less probable scenario than the other two.

1.4 CURRENT STUDY

One objective of this project is to study the effects of uniform airflow on the efficiency of fibrous filters. To further this aim, a transparent prototype housing was built with the thought in mind of providing the most uniform flow possible to an AF3192 panel filter. The flow field in this housing was measured using *Laser Doppler Velocimetry* at many different locations in several different horizontal planes of the housing for a constant volumetric flow rate. Flow visualizations were also performed to corroborate the LDV measurements. Using measurements from the LDV system, filtration efficiencies were

calculated using a method similar to Sabnis (1993) to provide local initial efficiencies with mono-disperse particle distributions. Overall efficiencies were also determined for several different particle sizes. The calculated efficiencies for the prototype housing were compared to similar efficiencies calculated for the J726 housing and a hypothetical uniform flow.

Another objective was to study the effects of adhesion and bounce on the overall efficiency of fibrous filters. By using Equation (1.49) and Equation (1.50), the effect of adhesion and bounce has been compared to the efficiencies calculated for perfect adhesion.

CHAPTER II

EXPERIMENTAL SETUP FOR VELOCITY MEASUREMENTS AND FLOW VISUALIZATIONS

The prototype shallow angle diffuser type panel filter test housing shown in Figure 2.1 was built to provide a more uniform flow to the filter being tested. This housing retains the exit, or section downstream of the filter, from the panel filter universal test housing specified by SAE J726 and shown in Figure 1.1. The housing was built from 1/4" clear acrylic sheet to facilitate velocity measurements by laser Doppler velocimetry. This housing was specifically built for the Purolator AF3192 panel air filter cartridge. Flow separation from the walls of the housing was not expected due to the very shallow angles of the diffuser section, 2.8° and 0.6°. Velocity measurements by laser Doppler velocimetry and flow visualizations using tufts and laser sheet lighting of water droplets were performed to analyze the flow characteristics of the housing.

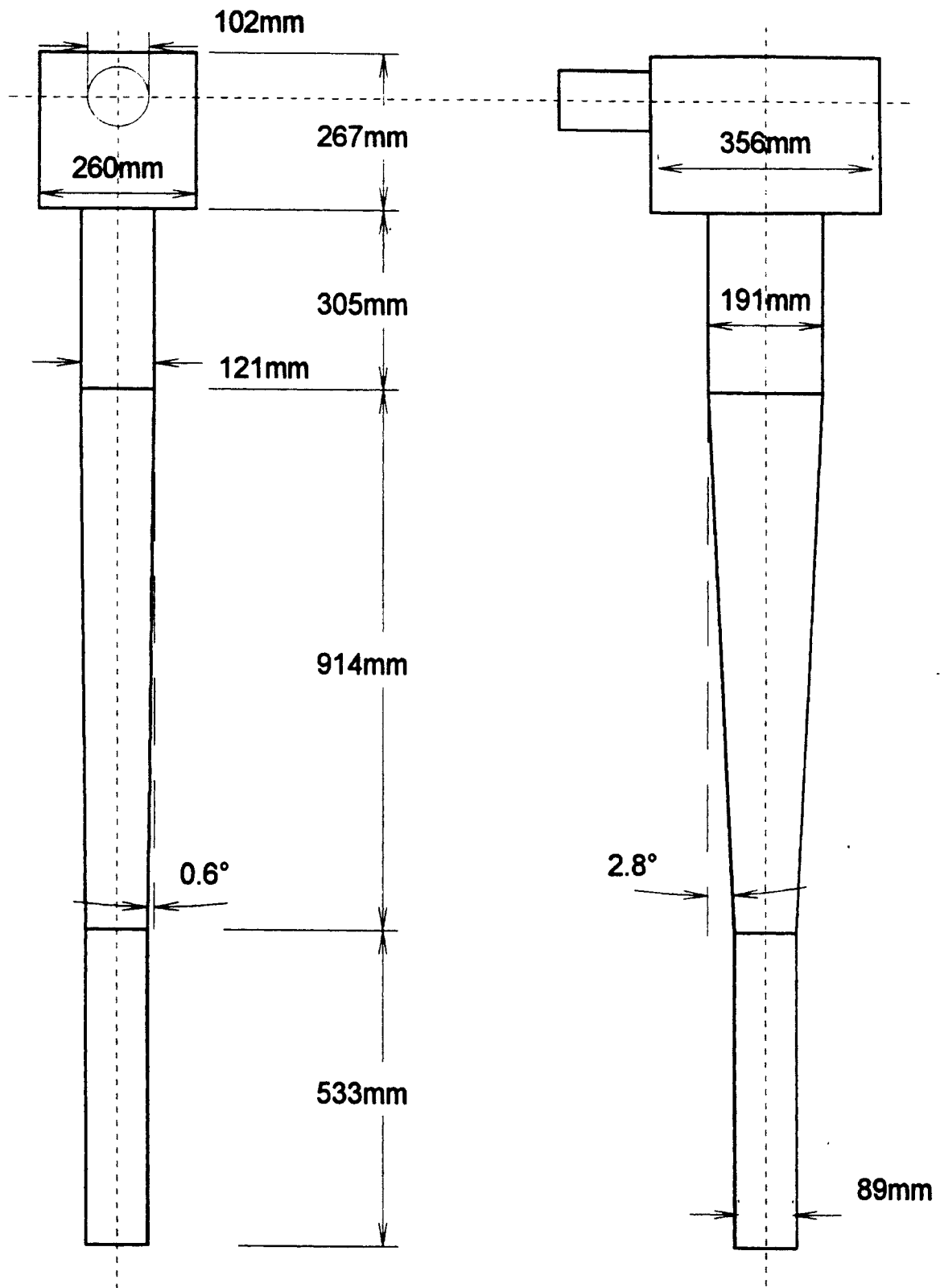


Fig. 2.1 Shallow angle prototype panel filter test housing.

2.1 VELOCITY MEASUREMENTS

Velocity measurements were performed in three separate horizontal planes of the test housing using a laser Doppler velocimeter (LDV) system.

2.1.1 Laser Doppler velocimeter basics

A laser Doppler velocimeter makes use of the fringe pattern of light and dark bands created by the crossing of two like-colored beams of light to determine the velocity of a particle that passes through the fringe pattern. When two beams of light intersect at a given angle, they produce interference fringes in a volume of space called the *probe volume* where in some areas the light is increased by wave addition producing a light band and in some areas waves cancel each other out producing a dark band. The distance between the light or dark bands, d , is known from the angle at which the two beams cross and the frequency of the light in the beams.

As a seed particle passes through the probe volume, it scatters light in all directions. The scattered light signal is called the *Doppler burst signal* and consists of intensity maxima and minima that correspond to the light and dark bands of the probe volume. The Doppler signal is collected by a lens and is transmitted through fiber optics to a photodetector that converts the optical signal to an analog electrical one and passes it on to the *Doppler Signal Analyzer (DSA)*. The Aerometrics DSA hardware and software take the raw Doppler burst signal, which may be considered as a sine wave superimposed on a Gaussian envelope or pedestal, as shown in Figure 2.2, and removes the pedestal component to produce a symmetric signal. An analog to digital converter (ADC) then produces

a square wave with the same frequency as the original signal. A discrete Fourier transform (DFT) is performed on the converted signal to determine its frequency.

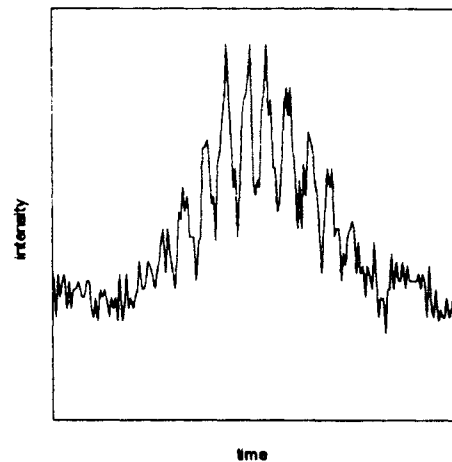


Fig. 2.2 Example of a Doppler burst signal

The DFT is given by

$$f(n) = \frac{1}{N} \sum_{k=0}^{N-1} x(k) \left[\cos \frac{2\pi nk}{N} - i \left(\sin \frac{2\pi nk}{N} \right) \right] \quad (2.1)$$

where n is the discrete frequency, N is the total number of samples, $x(k)$ is the complex, filtered, sampled data from the ADC, and i is the imaginary number. The DFT has the effect of multiplying the sampled wave by sine waves of N different frequencies. When the sampled signal and the sine wave have similar frequencies, the product will be large which appears as a maximum power in the frequency domain. The power is given by the sum of the squares of the products of the sine and cosine with the sampled data. A schematic of the discrete Fourier transform method applied to a one bit sample is given in Fig 2.3.

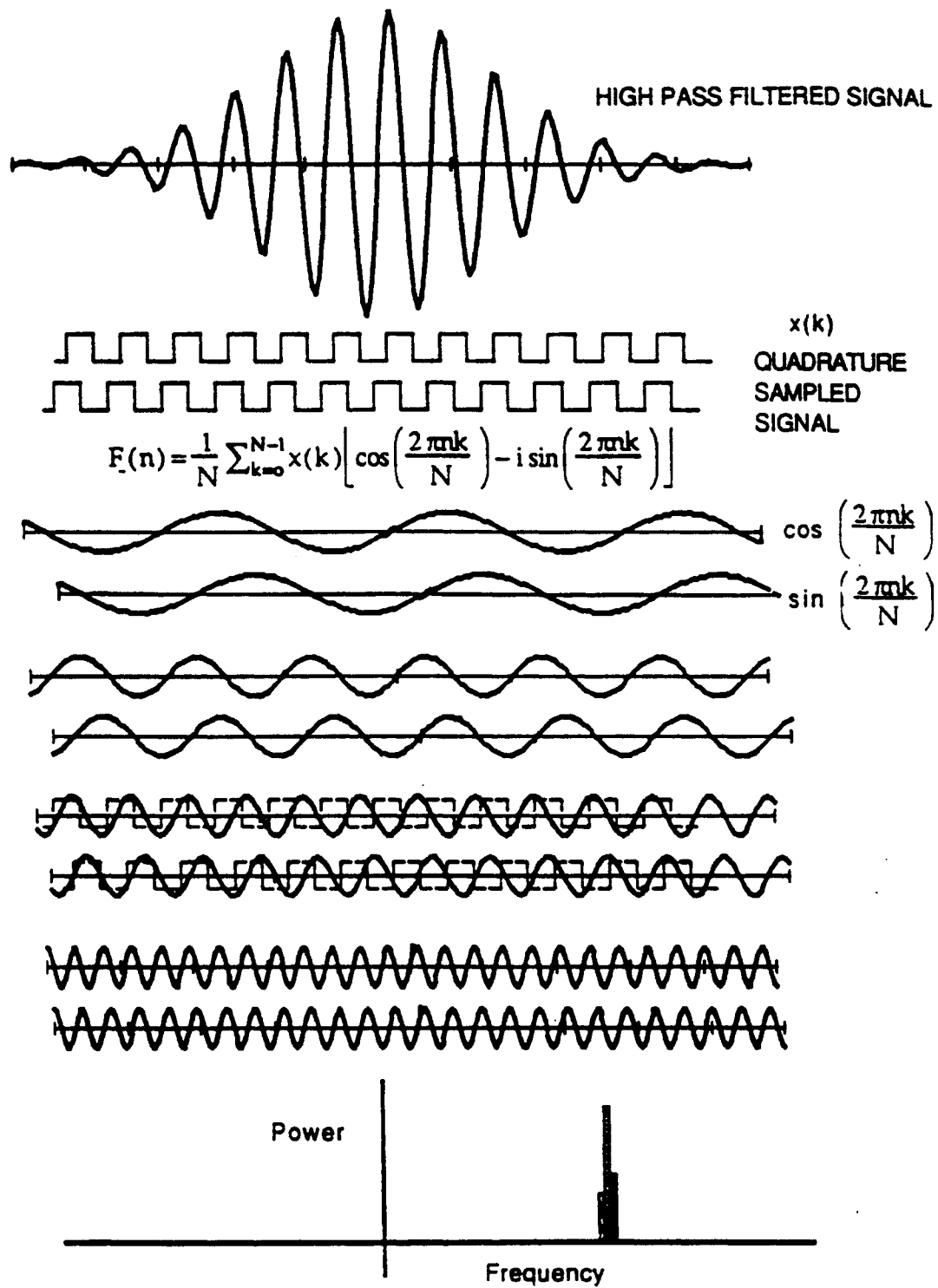


Fig. 2.3 Schematic of the discrete Fourier transform method applied to a one bit sample (Aerometrics 1992)

By knowing the frequency, f , and the distance between fringes, d , the velocity, v , is easily obtained with the relation

$$v = fd \quad (2.2)$$

By shifting the frequency of one of the two beams a certain amount the fringe pattern will move through the probe volume with a certain known velocity. This allows the LDV system to detect particles with a velocity of zero and to determine the direction of the particle motion. A second pair of beams of a different color, crossing at the same point, is used to measure a perpendicular component of the velocity.

When making velocity measurements, the transceiver, which both emits the laser beams and receives the scattered signal, was rotated in such a manner that the horizontal and vertical velocities were measured directly. It is easily seen from Figure 2.4, which illustrates a particle passing through a portion of the probe volume, that the seed particle will pass through many horizontal bands but only a few vertical bands. This in turn produces a very nice looking signal for the vertical velocity, Figure 2.5 (a), but a rather poor looking one for the horizontal velocity as shown in Figure 2.5 (b). Because the vertical velocity is the dominant one in our case, this possible problem was neglected. If it were desired to know the small horizontal velocity very accurately, it would be possible to rotate the fringe pattern through 45 degrees and then perform a vector analysis on the resultant measured velocities to obtain velocities in the original coordinate system. The moving fringes created by the Bragg cell frequency shift improve low velocity

measurements. With the moving fringes, the particle will cross many more fringes than it would if the fringes were stationary.

As pointed out by Gould & Loseke (1993), the probability of a seed particle entering the probe volume, and thus the probability of a measurement being made, is higher for particles with a velocity greater than the average velocity. The probability of a particle with a velocity slower than the average flow velocity passing through the probe volume at any given time is lower. By measuring more high velocity particles than low velocity particles, the data becomes biased toward the higher velocities. This biasing problem has been found to be relatively insignificant for low turbulence levels. Multiple realizations, or more than one measurement from the same particle, are most often caused by frequency shifting. This has been called Bragg cell bias. Slow particles may stay in the probe volume long enough for the processor to count them more than once. Over-counting slow particles tends to reduce the effect of velocity bias. There are several different ways to counter the velocity bias problem, but no velocity bias correction of the collected LDV signals was performed on the data.

2.1.2 Laser Doppler velocimeter setup parameters

When using the LDV system, it is required that several parameters in the software be set in order to obtain accurate data. Several tests were run using different values of samples per data point to determine what the most accurate yet least time consuming value would be. This number was found to be 1000 samples per data point. A summary of the data obtained in these tests can be found in Appendix A.

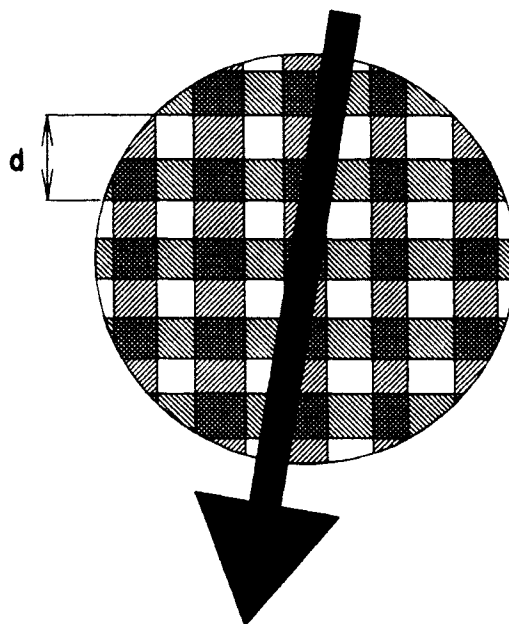


Fig 2.4 Diagram of a particle passing through probe volume

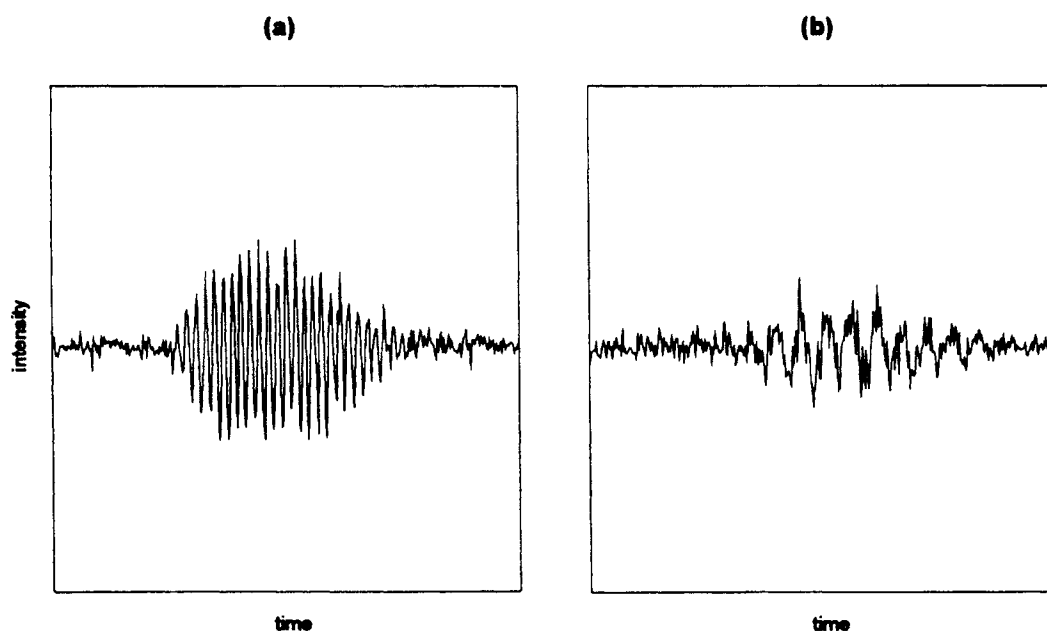


Fig. 2.5 (a) an example of a vertical Doppler burst signal with pedestal removed and (b) a horizontal Doppler burst signal with pedestal removed

2.1.3 Equipment List

1. **PSL particles:** Duke Scientific Corporation Uniform Polystyrene Latex (PSL) Microspheres 0.966 μm in diameter were used as seed particles for the LDV system. The particles are packaged in a 10% by volume suspension; 90% being distilled water and 10% being PSL particles. By mixing 2 parts PSL suspension with 1000 parts distilled water, a 200 parts per million suspension was created. It was found that with this mixture the LDV system required 2 to 3 minutes per measurement point. PSL particles were chosen for seed particles by comparing the repeatability of data points measured with PSL particles dispersed with an atomizer to points measured with water droplets produced with a humidifier, as used by Sabnis. A summary of data obtained in these tests can be found in Appendix B.
2. **Atomizer:** A TSI Incorporated Model 9306 6-Jet Atomizer was used to generate the PSL aerosol. The atomizer was operated using all six jets at a regulated air pressure of 25 psig.
3. **Shallow Angle Test Housing:** A transparent test housing was constructed of 6 mm clear acrylic sheet by myself of a design by my colleague F. Liang. Liang had previously made a similar housing. Acrylic sheet, or Plexiglas, was chosen because of its uniform optical qualities, cost, and ease of construction. The test housing dimensions are shown in Figure 2.1. The use of a very shallow angle diffuser section prior to the flat walled test section was expected to produce a very uniform non-separating flow. The test section dimensions were specifically made to fit the AF3192 filter. This housing would not be suitable for other filters. The exit or

discharge plenum of the housing is based on that of the universal test housing from SAE J726. All joints were glued with an acrylic solvent type cement and then tested with soapy water to find any leaks. The test housing was then mounted upside down, as compared to the J726 standard, for test purposes.

4. **Filter:** Purolator AF3192 panel air filters were used in the velocity measurement tests. The filters have a projected surface area of 120.65 mm by 190.5 mm. Other specifications for these filters can be found in Appendix D. They are made from a resin impregnated cellulose fiber paper mat that is first embossed and scored, glue is then applied to the edges of the paper and the paper is folded, creating the pleats and sealing the ends. After folding, the pleats are counted and a paper pack is cut, pleated, and end sealed, then mounted in a rubber holder or gasket. The filter pack is then heated to cure the resin so that the pleats will hold their shape. Cured paper packs can then be placed into molds containing a liquid endseal material. Most manufacturers place a screen into the endseal material then position a paper pack over the screen. This screen helps the filter maintain its structural integrity in the event of engine backfire or if the filter paper should become wetted. After curing of the endseal material, the finished filter is released from the mold, marked, dated, and packed.
5. **Centrifugal Blower:** A 1.5 hp centrifugal blower capable of producing a maximum flow rate of 225 SCFM through the test housing and flow meter assembly was used for velocity field measurements.

6. **Mass Flow Sensor:** A TSI Incorporated Series 2010 Mass Flowmeter was used to measure the flow rate through the test housing. The flow sensor has a maximum measurable flow rate of 500 SCFM. Calibration with a 76 mm ASME flow nozzle was performed before using the flow sensor in the velocity field measurement tests.
7. **Laser:** A Coherent 4 Watt (optical) laser consisting of an argon ion plasma tube powered by an Innova 70-A power supply. The intensity of the beam was controlled by a remote controller.
8. **Bragg Cell & Driver:** An IntraAction Bragg cell driver model ME-40H controlled the Bragg cell mounted inside the fiber drive. The light beam from the plasma tube was directed by steering mirrors into the fiber drive and through the Bragg cell. The Bragg cell split the beam into two beams, with one of them shifted by 40 MHz.
9. **Fiber Drive:** An Aerometrics model FBD.1240 fiber drive used beam splitting prisms to split the shifted and unshifted beams into a green and a blue shifted and a green and a blue unshifted beam giving a total of 4 beams. Mirrors direct each of the four beams into its own fiber coupler that used a lens to focus the beam onto an optical fiber.
10. **Transceiver:** The Aerometrics model XRV.1212 transceiver received the four beams from the fiber drive through fiber optic cables. The pair of blue beams and the pair of green beams are projected in mutually exclusive perpendicular planes through a lens with a focal length of 500 mm. The beams are focused by the lens at its focal point producing the interference fringe probe volume. Particles passing through the light and dark fringes of the probe volume create Doppler bursts by

scattering light from the interference fringes in all directions. The Doppler bursts are received by the transceiver lens and are focused on another optical fiber that transmits the light to the photodetector.

11. **Photodetector Unit:** The Aerometrics photodetector unit model ROM.2200.L contains two photomultipliers, one for each light wavelength (green and blue). The photomultipliers convert the optical signal to an analog electrical signal and pass it on to the DSA.
12. **Doppler Signal Analyzer (DSA):** The Doppler burst signal is analyzed by the Aerometrics Doppler Signal Analyzer model DSA.3220. The signal is first high pass filtered to remove the pedestal from the Doppler burst signal then low pass filtered to remove noise. A peak detector in conjunction with a burst detector locates the center of the signal. Programmable mixers are used to reduce the signal frequency before it is presented to the analog to digital converter. The ADC converts the complex, filtered, sampled signal to a square wave of the same frequency as the input signal. A *Digital Signal Processor* (DSP) is used in the computer to perform the *discrete Fourier transform* (DFT) using the *fast Fourier transform* (FFT) algorithm. The DSP is a dedicated processor that is programmed to compute the Fourier transforms at a high rate and pass the results to the system software for statistical analysis and presentation of the velocity information of the particles in histogram form.
13. **Personal Computer:** An Intel 486 DX/2 compatible personal computer running at 66 MHz is used to control the entire DSA system. Aerometrics DSA software

takes the velocity information from the DSA hardware and performs statistical analysis on the information to provide the velocity information in histogram form. The mean velocity, rms velocity, angle of the flow, and the mean total velocity for each run are also presented, along with other statistical data such as run time and turbulence intensity. The data from each run can be stored on disk. This stored data can then be reduced to provide the user with data that is needed, in tabular form, with a separate program.

14. Automated Traverse Table: The transceiver is mounted on a Daedal two component traverse table system. This allows the user to move the transceiver in very precise (0.001 inch) steps, in two perpendicular directions. The table has been automated by attaching stepper motors to each lead screw. The stepper motors are controlled through computer software written by myself. The software is written so that a user can move the traverse in either direction by steps or to an absolute location. The program uses a graphical user interface and each location can be saved in tabular (x,y) form to a file.

The LDV system consists of items 7 through 13 and is shown in schematic form in Figure 2.6.

2.1.4 Experimental setup and procedure

Figure 2.7 pictures a schematic of the system used to regulate and seed the flow through the test housing. Air is drawn through the housing by the blower which exhausts through a 6 meter length of straight 152 mm PVC pipe into the TSI flowmeter. A valve on the exhaust side of the blower is used to regulate the flow. Seed particles are produced

with the atomizer and are introduced into the system along with the air. Measurements were taken in three different horizontal planes of the test housing; 13 mm, 51 mm, and 102 mm upstream of the filter surface, the peaks of the filter pleats, as shown in Figure 2.8. In each plane measurements were taken using the grid shown in Figure 2.9. Figure 2.10 shows the coordinate system that was used for measurements. A particle with a positive axial velocity will tend to be moving in the downward direction through the housing. A particle with a positive transverse velocity will tend to be moving to the right as it passes through the housing.

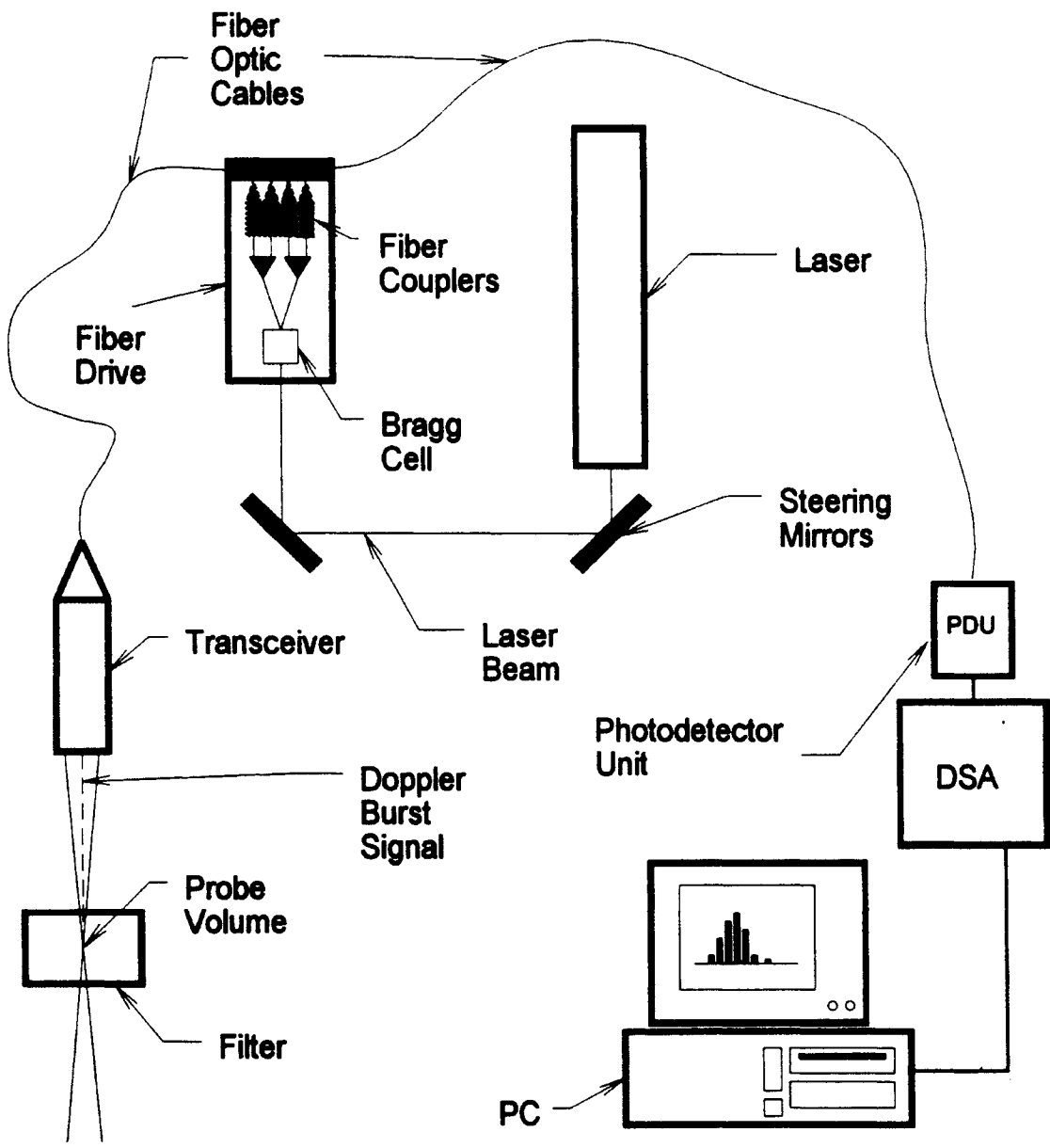


Fig. 2.6 Schematic of the Laser Doppler Velocimetry system

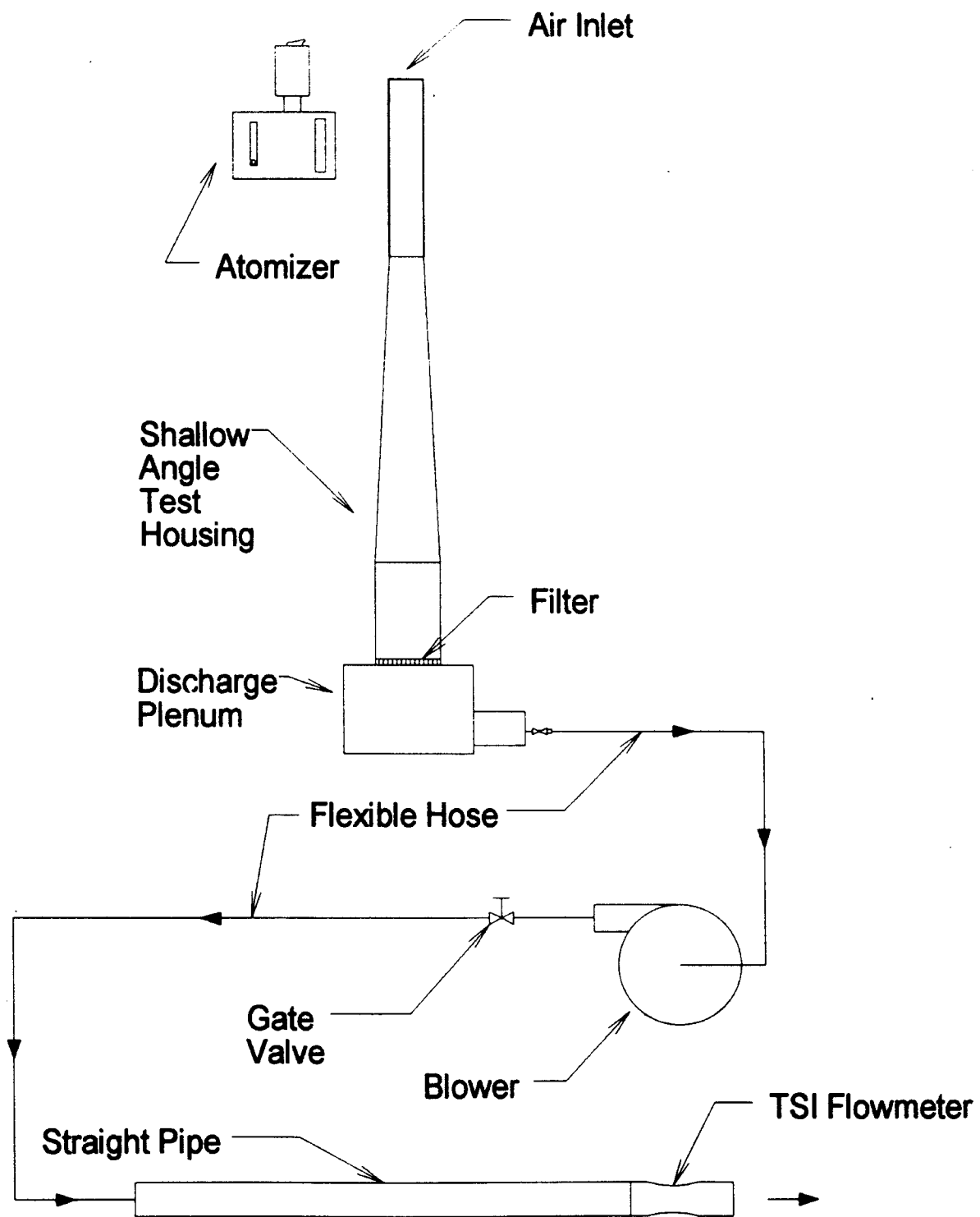


Fig. 2.7 Schematic of airflow through test housing and related equipment

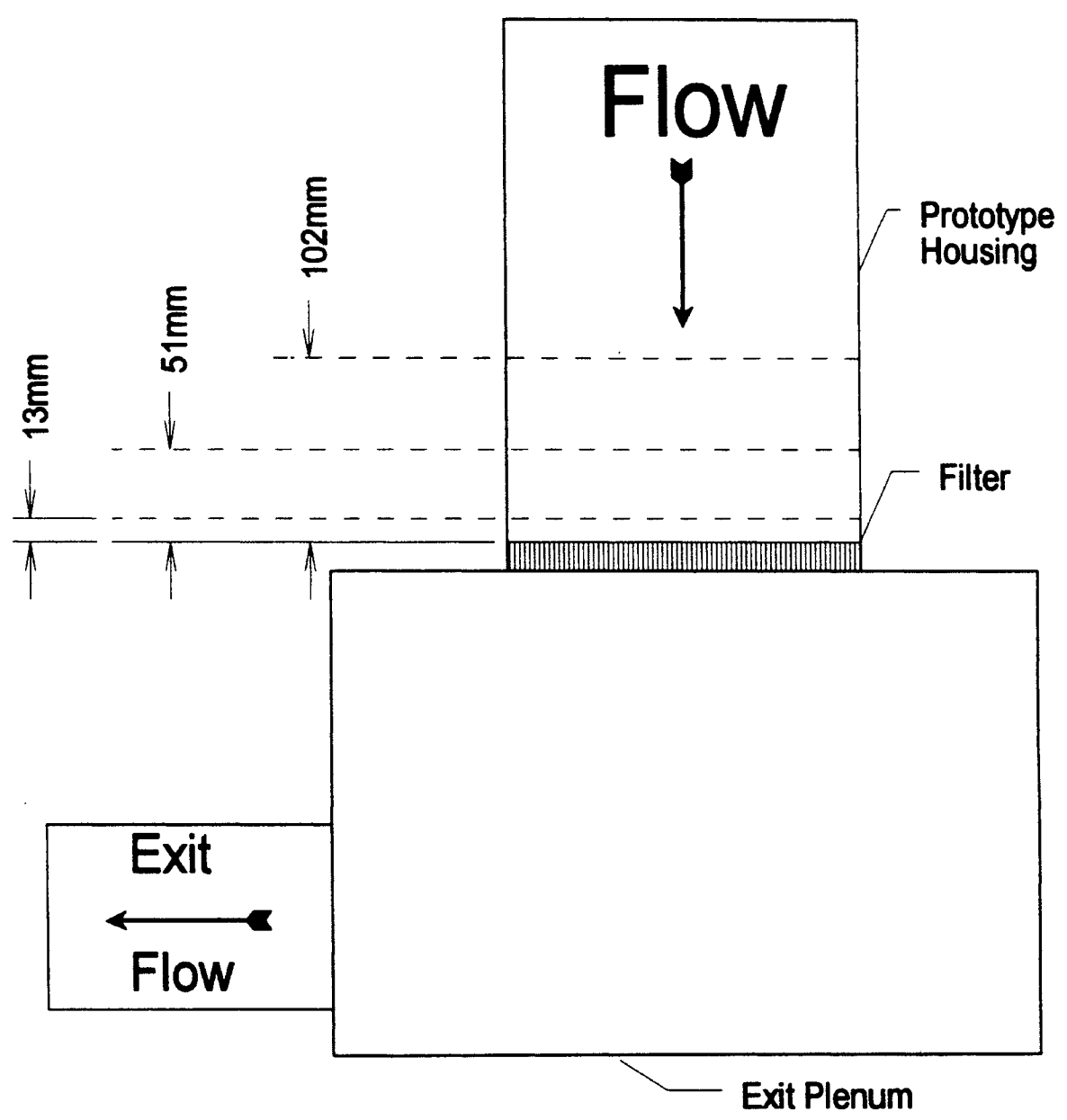


Fig. 2.8 Velocity measurement planes

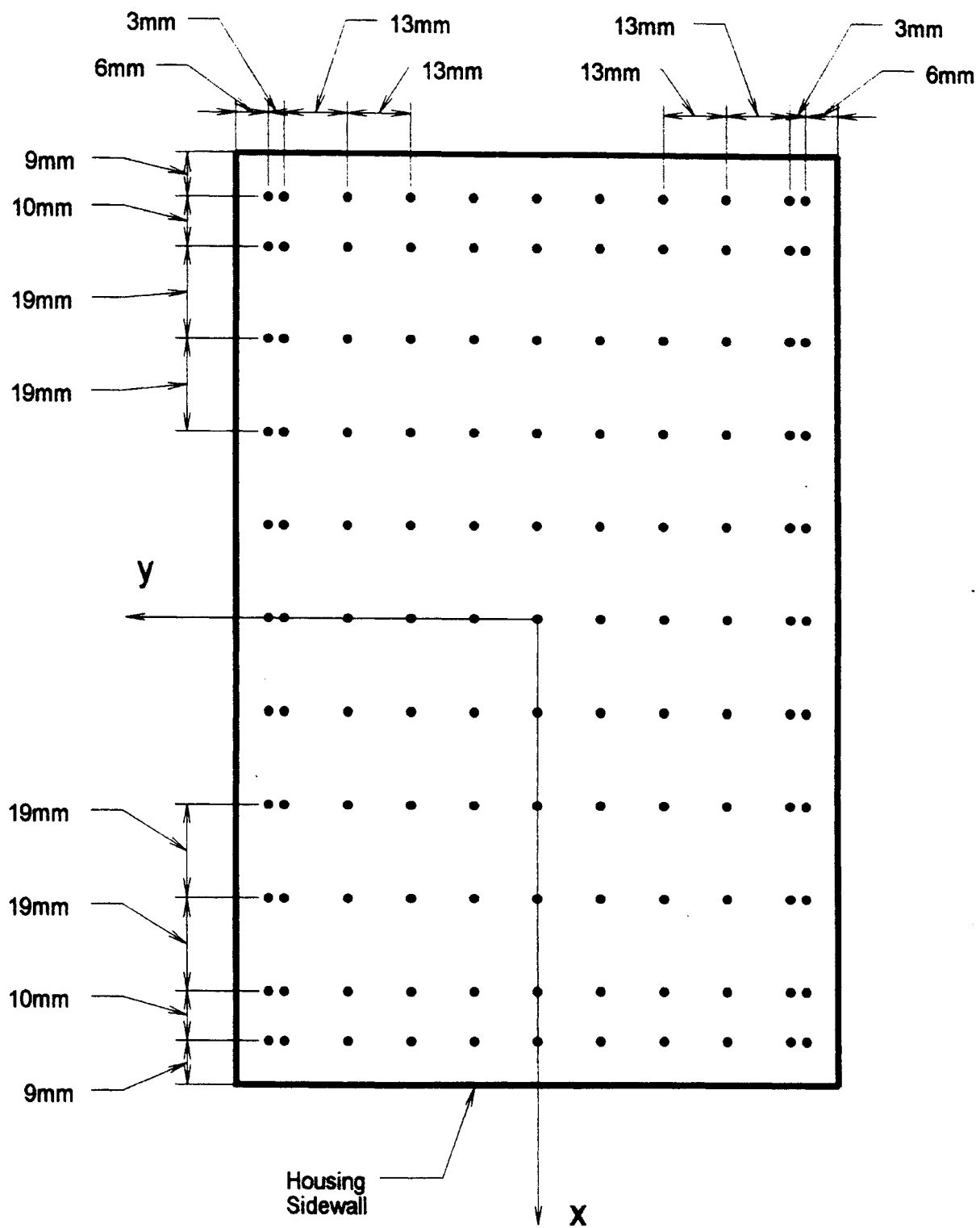


Fig. 2.9 Velocity measurement grid

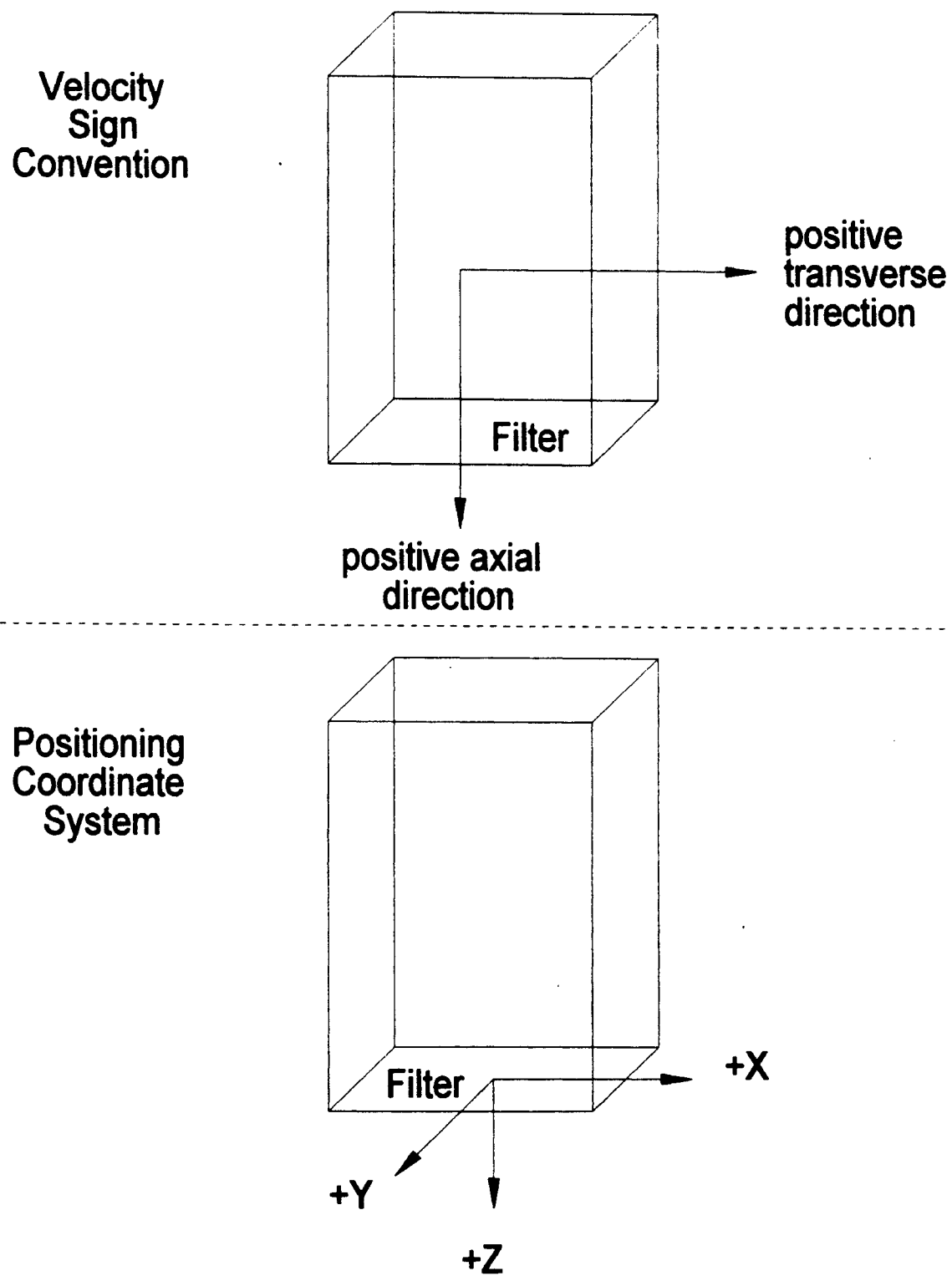


Fig. 2.10 Sign convention and coordinate system for velocity measurements

Figure 2.11 shows the relative alignment of the test housing to the transceiver. The test housing was aligned longitudinally with the transceiver by marking vertical centerlines on two opposing sides of the test housing with removable ink, thus establishing the center of the housing in the x-direction. The housing was then moved until both vertical laser beams passed through both lines at the same time. This procedure was also used to align the housing in the horizontal plane by drawing horizontal lines on two opposing sides of the housing, again in removable ink, and moving the housing up or down until the two horizontal beams passed through both lines at the same time. The use of two beams for each alignment procedure ensured that measurement plane was level as well as aligned with the transceiver.

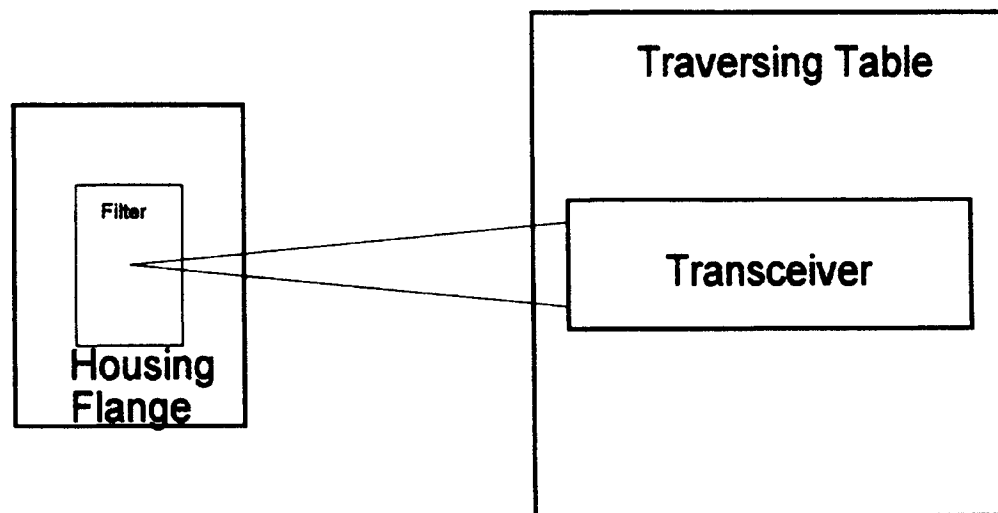


Fig. 2.11 Diagram of relative positions of filter housing and transceiver during tests

To find the approximate center of the housing, the LDV system was used. Air flow was seeded and induced through the housing to provide a signal to the LDV system. Then by moving the traverse so that the probe volume was situated in a position close to

the near perpendicular wall, it was easy to find a position very close to the wall. This was accomplished by moving the probe volume, in very small steps, closer to the wall until the LDV system no longer picked up Doppler burst signals. When this point was reached, it was assumed that the probe volume was situated on the inside surface of the wall. By then moving the traverse -60.325 mm (-2.375 inches) in the y-direction, the approximate center of the housing is found. The center of the housing in the x-direction was already defined by the centerline marks used to align the housing. This approximate center of the housing was given the coordinates $(x,y) = (0, 0)$. I estimate that this approximate center was accurate to $(x,y) \pm (0.8 \text{ mm}, 0.0254 \text{ mm})$.

2.2 FLOW VISUALIZATIONS

Flow visualizations have long been used as a very effective method of qualitatively analyzing flow fields. A flow visualization technique using laser sheet lighting of water particles mixed into the flow was used on the housing. Tufts were also used. Black and white along with color still photography was used to document the laser sheet tests. The laser sheet flow visualization was also captured on video tape.

2.2.1 Laser sheet lighting of water particles

A sheet of laser light was produced by projecting a very powerful beam of laser light, 3 to 4 optical watts, through a cylindrical lens. This creates a sheet of laser light that fans out from the lens in a plane that may be a horizontal, vertical, or some angle between horizontal and vertical depending upon how the lens is oriented. When this sheet passes through the housing, which is made from clear acrylic sheet, it illuminates a two-

dimensional slice of the flow field. Great care must be used when performing a flow visualization in this manner to avoid reflecting powerful laser light into one's eyes.

2.2.2 Tufts

Tufts of yarn and thread were attached to the housing at regular intervals in an attempt to prove that the flow was not separating from the walls of the housing. The tufts were first oriented so that the end of the each tuft was facing downstream. This, however, did not produce very good results. The shear stress exerted on the tufts by the flow was so low that the tufts would wiggle a small amount but do little else, giving very little information about flow. A few of the tufts were then turned so that the free end pointed upstream, or into the flow. With the tufts oriented in this manner it was fairly obvious that there was a shear stress at the wall in the positive axial direction because the ends of the tufts pointed downstream when the flow was present.

CHAPTER III

RESULTS AND DISCUSSION OF LASER DOPPLER VELOCITY MEASUREMENTS AND FLOW VISUALIZATIONS

3.1 LASER DOPPLER VELOCIMETER MEASUREMENTS

The flow field velocity measurements will be represented here in the form of two-dimensional (2-D) plots and three-dimensional (3-D) plots. Each of the two measured components of the velocity are represented separately. The 2-D plots offer more detail than the 3-D plots but only for a slice of the flow field; whereas, the 3-D plots offer a better overall picture of the flow. In all of the plots presented here, the edges of the X or Y axes represent the edges of the filter. So in a 2-D plot, the right edge of the plot represents the right edge of the filter and the left edge of the plot represents the left edge of the filter and for 3-D plots, the bottom surface of the plot represents the surface area of the filter. Data taken in this study when plotted represents the full width, front to back, of the filter. Data taken by Sabnis (1993) represents only the front half of the filter and is plotted in the same manner as the current data with the rear half of the plot missing.

After all the measurements were taken a major air leak was found in the blower. This caused the measured flow rate to be off by about 10%. This corresponds to an actual flow rate of around 3.14 m³/minute (111 scfm) rather than the 3.54 m³/minute (125 scfm) as measured by the TSI flowmeter. The flowmeter has subsequently been moved to a

position upstream of the blower. This should not make major difference to the results presented here. The measured velocities should scale for different flow rates.

3.1.1 Two-dimensional representations of velocity measurements

Fig. 3.1 illustrates the axial and transverse velocity profiles through a center-line slice of the flow, $y = 0$, at the three measured planes. The figure shows that all the profiles are quite similar even though the 13 mm profile was measured several weeks after the other two with a different filter and different atmospheric conditions. The 51 mm and the 102 mm profiles were taken on sequential days with the same filter and provide nearly identical results. This leads one to believe that this flow field is very near to a fully developed duct flow state.

The humidity was quite low when the 51 mm and 102 mm profiles were measured, so there were very few water particles mixed with the PSL particles. With the 13 mm profile, however, the humidity was very high and many of the Doppler bursts could be attributed to water droplets rather than PSL particles. The water particles can be more massive than the PSL particles. The more massive water particles may reduce turbulence measurements, or the velocity fluctuations about the mean velocity, in the flow by not following swift changes in the flow field. This may be part of the reason for the variance observed when comparing the 13 mm profile to the 51 mm and 102 mm profiles. The 13 mm profile's proximity to the filter is probably the most important reason for its differences from the other two. As the flow approaches the filter, the flow will try to spread out, making the axial component of the velocity more uniform.

All the axial plots have basically the same shape. The axial velocity is low near the walls and reaches a peak near the center. The velocities all have a positive magnitude

indicating that the flow is completely directed into the filter and there is no recirculation. The transverse velocity profiles also show trends of similarity when compared with each other. Transverse velocities on the left side of the filter tend to be negative while those on the right side of the filter tend to be positive. This shows that as the flow nears the filter it fans out, like an impinging jet. However the flow cannot go very far in the transverse direction, but this increase in transverse flow can make the axial component more uniform.

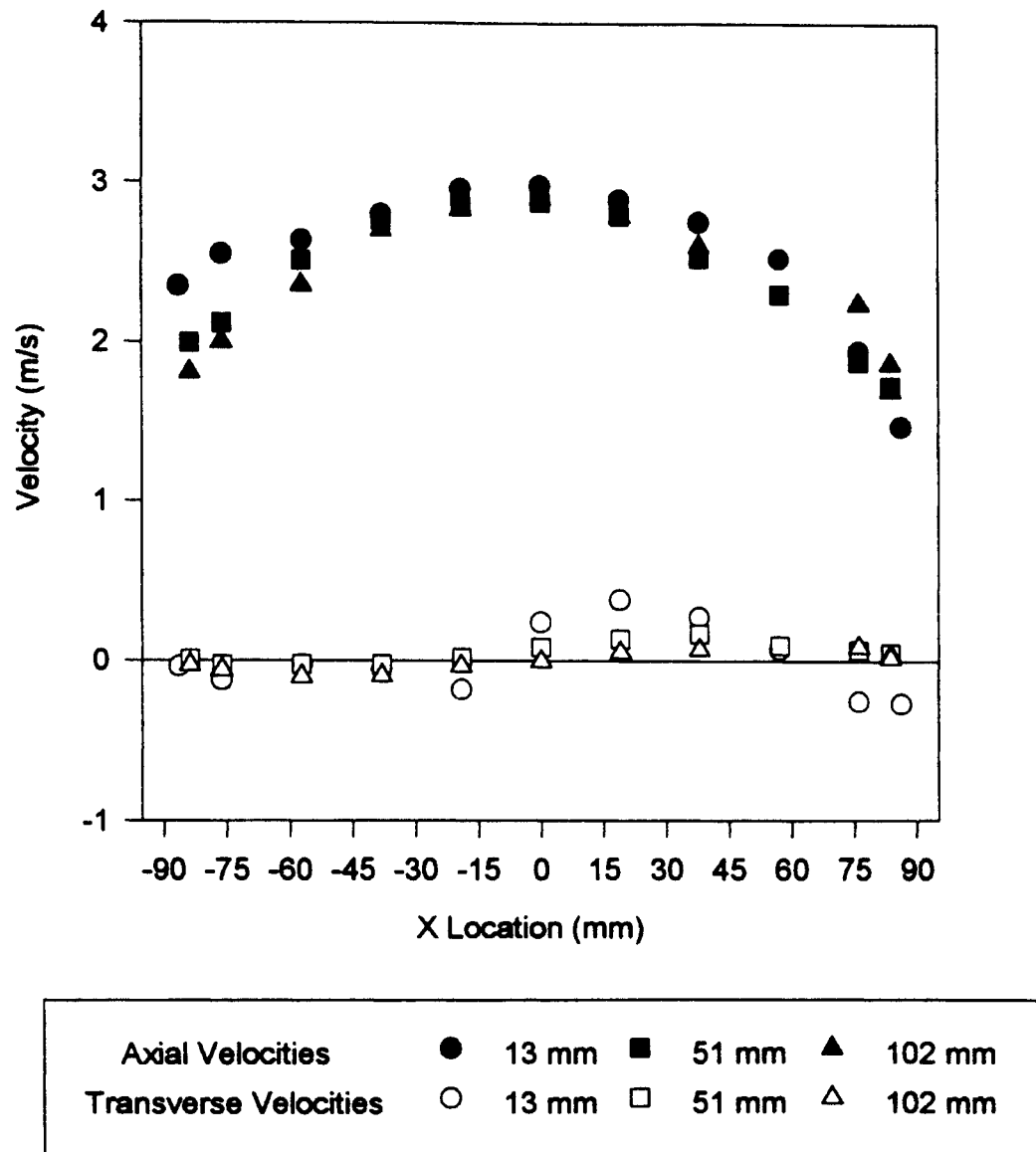


Fig. 3.1 Comparison of axial and transverse velocity profile slices in prototype housing at $y = 0$

3.1.2 Comparison of prototype housing data with J726 housing data in a two-dimensional format

Fig. 3.2 illustrates a comparison of the current axial velocity data collected for the shallow angle diffuser test housing and the axial velocity data collected by Sabnis (1993) for the J726 housing along the y centerline. The data has been non-dimensionalized by dividing each data point by the average of all the axial velocity measurements in the given plane. It is easily seen from this comparison that the prototype housing provides a much more uniform flow upstream of the filter. The prototype axial mean velocity profile is very flat, with the velocity peak at the center of the velocity profile being much less pronounced than the velocity peak at the center of the J726 housing profile.

Fig. 3.3 illustrates a comparison of the transverse y-centerline velocity profile of the prototype housing with that of the J726 housing, both measured in the plane 13 mm upstream of the filter. The data has been non-dimensionalized by dividing each data point by the average of all the transverse velocity measurements in the given plane. This comparison also shows a much more uniform flow field upstream of the filter. Some of the transverse mean velocity magnitudes in the J726 velocity profile approach 75% of the average axial mean velocity, whereas no transverse mean velocity magnitude in the prototype housing profile is greater than 25% of the average axial mean velocity. Both the prototype housing profile and the J726 housing profile are similar in shape being generally negative in magnitude on the left side of the filter and positive in magnitude on the right side of the filter. Both the prototype housing and the J726 housing are providing a flow field that is similar to an impinging jet but the divergence observed in the prototype housing is much more mild than that found in the J726 housing.

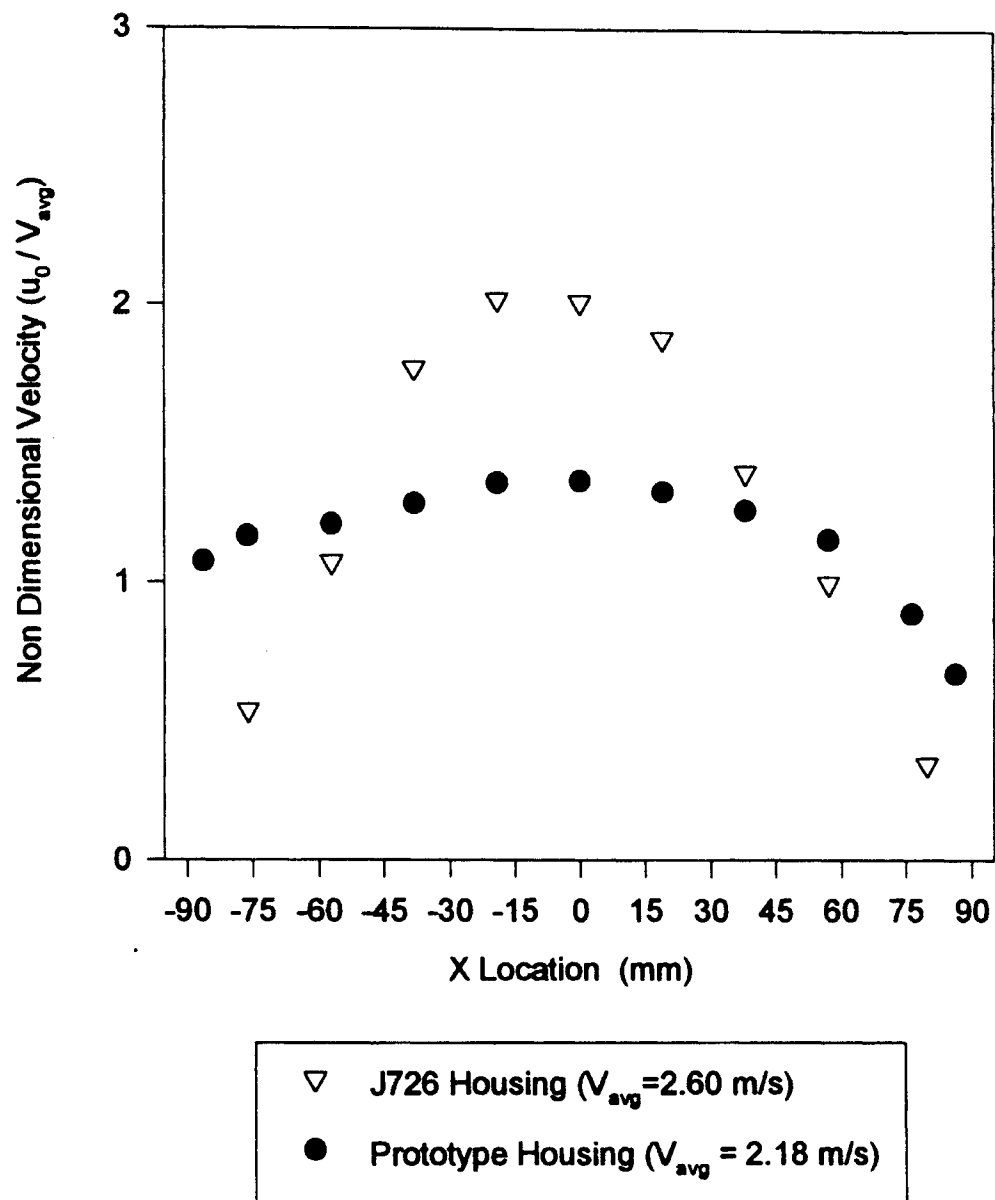


Fig. 3.2 Comparison of the prototype housing axial velocity data with axial velocity data from the J726 housing, 13 mm upstream of the filter

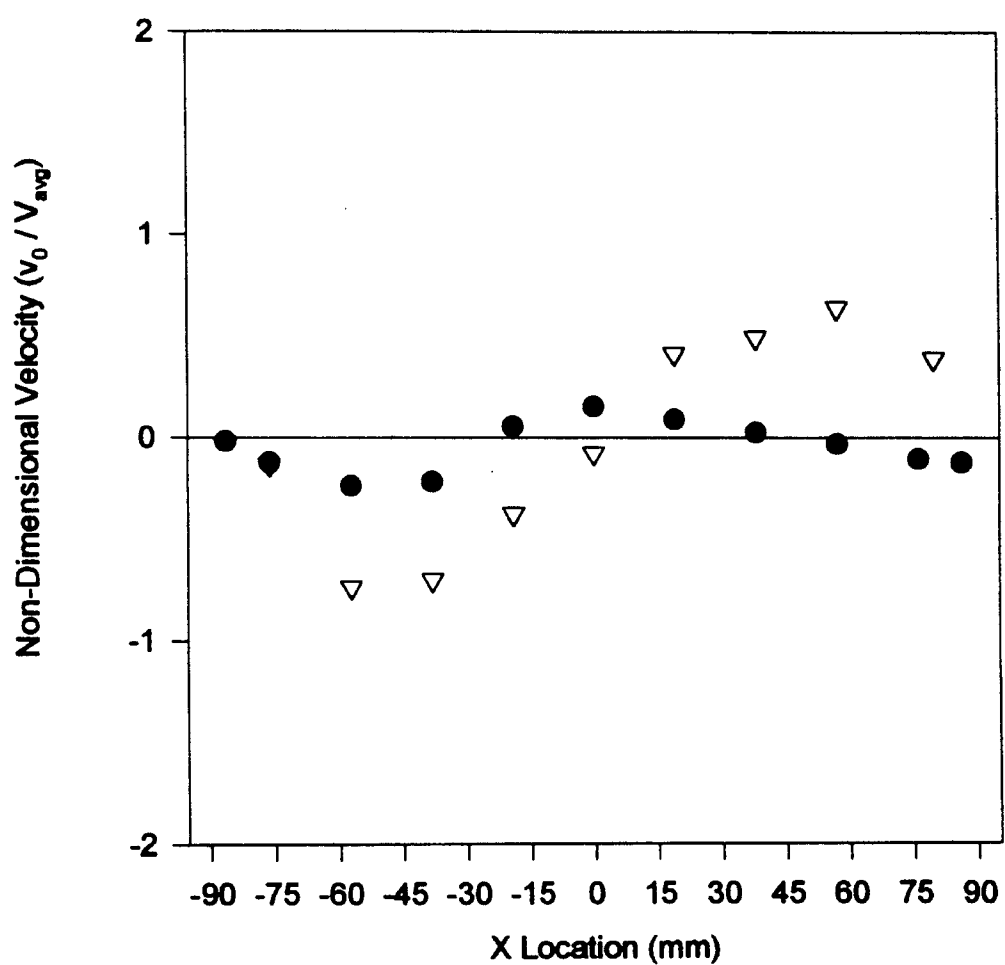


Fig. 3.3 Comparison of the prototype housing transverse velocity data with transverse velocity data from the J726 housing, 13 mm upstream of the filter

3.1.3 Three-dimensional representations of velocity measurements

The collected velocity data can also be represented in a three-dimensional (3-D) form. This form is more readily visualized than a collection of two-dimensional (2-D) plots. The axial and transverse velocity measurements will be presented in separate plots. Fig. 3.4 is a 3-D plot of the axial mean velocities in the prototype housing 102 mm upstream of the filter. The X and Y axes represent the location in the housing with the (0,0) location being the center of the housing. This location is also the center of the filter. The surface representing the axial velocity distribution across the plane is shaped like a shallow dome with the maximum velocity located near the center of the housing. The velocity near the center is 2.9 m/s which tapers off to a minimum measured velocity of 1.2 m/s near the wall of the housing. If we could measure closer to the wall, the velocities should become even lower as the no-slip condition must exist on the wall.

Fig. 3.5 represents a plot of the transverse mean velocities measured in the prototype housing in the same plane, 102 mm upstream of the filter surface. The divergent nature of the flow is easily seen here with the transverse velocities being mostly negative on the left side of the housing and mostly positive on the right side of the housing. The magnitudes of the transverse velocities are very low, with a maximum of 0.10 m/s and a minimum of -0.11 m/s. This indicates that the flow is almost totally axial, but does tend to diverge towards the walls of the housing as it approaches the filter.

Fig. 3.6 and Fig. 3.7 represent the axial and transverse components of the flow in a plane 51 mm upstream of the filter. The axial and transverse plots for the 51 mm plane are almost identical to their respective counterparts in the 102 mm plane. The axial distribution surface plot is shaped like a shallow dome with a maximum velocity near the center of

2.9 m/s and a minimum velocity near the wall of 1.1 m/s. The transverse velocity distribution surface plot for 51 mm has a general trend of very low magnitude velocities with negative velocity values on the left side of the housing and positive velocity values on the right side of the housing, much like the 102 mm velocity distribution. The similarity of the 51 mm velocity distribution surface plots to the 102 mm velocity distribution surface plots provides further evidence that the flow is similar to a fully developed or developing duct flow. The flow cannot be considered truly fully developed because of the relative shortness of the duct, 11 hydraulic diameters based on the straight section dimensions, and the fact that the housing duct is undergoing an area change over most of its length.

The axial velocity distribution for the plane nearest the filter, 13 mm, is represented in Fig. 3.8. It is also quite similar to the other two axial surface plots with the peak velocity coming in at 3.0 m/s and the minimum at 0.88 m/s. Measurements were taken nearer to the wall with this plane and only one half of the plane was measured at one time. The housing had to be rotated 180° to measure the other side without clipping a LDV beam. The two measured halves were then mated to provide this overall view of the velocity distribution. There are subtle differences between this plane and the two previously discussed planes. The velocities appear to drop off much more quickly on the right side of the housing than on the left, and the lowest velocities are lower than those in the 51 mm or 102 mm planes. The lower velocities could be due to some measurements being taken closer to the walls of the housing, and the sharp drop off could be caused by misalignment of the center point of the housing with the LDV system. These discrepancies are more probably due to another factor such as non-symmetry of the exit housing. The sharp

drop-off of velocity magnitude is on the exit side of the housing. The manner in which the filter is installed in the housing also affects the velocity measurements. The AF3192 filter pleats always had a curvature to them. The effect of the curvature of the filter pleats on the flow near the filter was studied before the velocity mapping took place. A short discussion on this topic can be found in the Appendix B. The filter itself may cause some changes in the measured velocities. The same filter was used for the first two tests but was not the same one used for the 13 mm test. The atmospheric conditions could also have played a role in creating the subtle differences between this plane and the others. Relative humidity was much higher on the day the 13 mm test was run. Proximity of the plane to the filter was probably the most important factor in causing the flow field changes. As the flow approaches the filter, it will tend to redistribute itself, creating a more uniform axial velocity profile. This should, and does, show up in the transverse velocity profiles that illustrate the flow tending to move toward the edges of the housing.

While the differences between the 13 mm axial velocity distribution and the other two planes' axial velocity distributions were quite subtle, the differences between the 13 mm transverse velocity distribution and the 51 mm or 102 mm transverse velocity distribution are immediately obvious. The surface plot of the 13 mm, shown in Fig. 3.9, does retain the same shape as the other two transverse velocity surface plots with the left half velocities being mostly negative in magnitude and the right half velocities being mostly positive in magnitude. However, the surface reveals a much greater range of velocities and is not as smooth. This variation is probably due to the proximity of this plane to the filter. As the flow approaches the filter, it will obviously try to diverge from its mostly

axial nature as if it is impinging upon a wall. This wall, however, is porous and does allow the flow to pass through so the divergence is reduced, offering a transverse velocity maximum of 0.5 m/s or less than 25% of the average axial velocity. The flow may be more unsteady near the filter. This unsteadiness will create problems with the DSA settings that were made for the steady flow further upstream. Each 1000 sample data point may not contain enough sample measurements to provide as accurate an average for the flow velocity at that point. This would cause the collected data to look rougher when plotted in a 3-D fashion such as Fig. 3.9. Averaging the collected data over more than 1000 samples this near to the filter might cause the very rough looking plot of Fig. 3.9 to become more smooth. The difference between this surface and the other two could also be related to other reasons stated before: non-symmetry of exit housing, pleat curvature direction, filter change or atmospheric conditions. The transverse velocities, while higher in the 13 mm plane than in the 51 mm or 102 mm planes, are still rather low, with the highest transverse velocity magnitude being less than 25% of the axial velocity average.

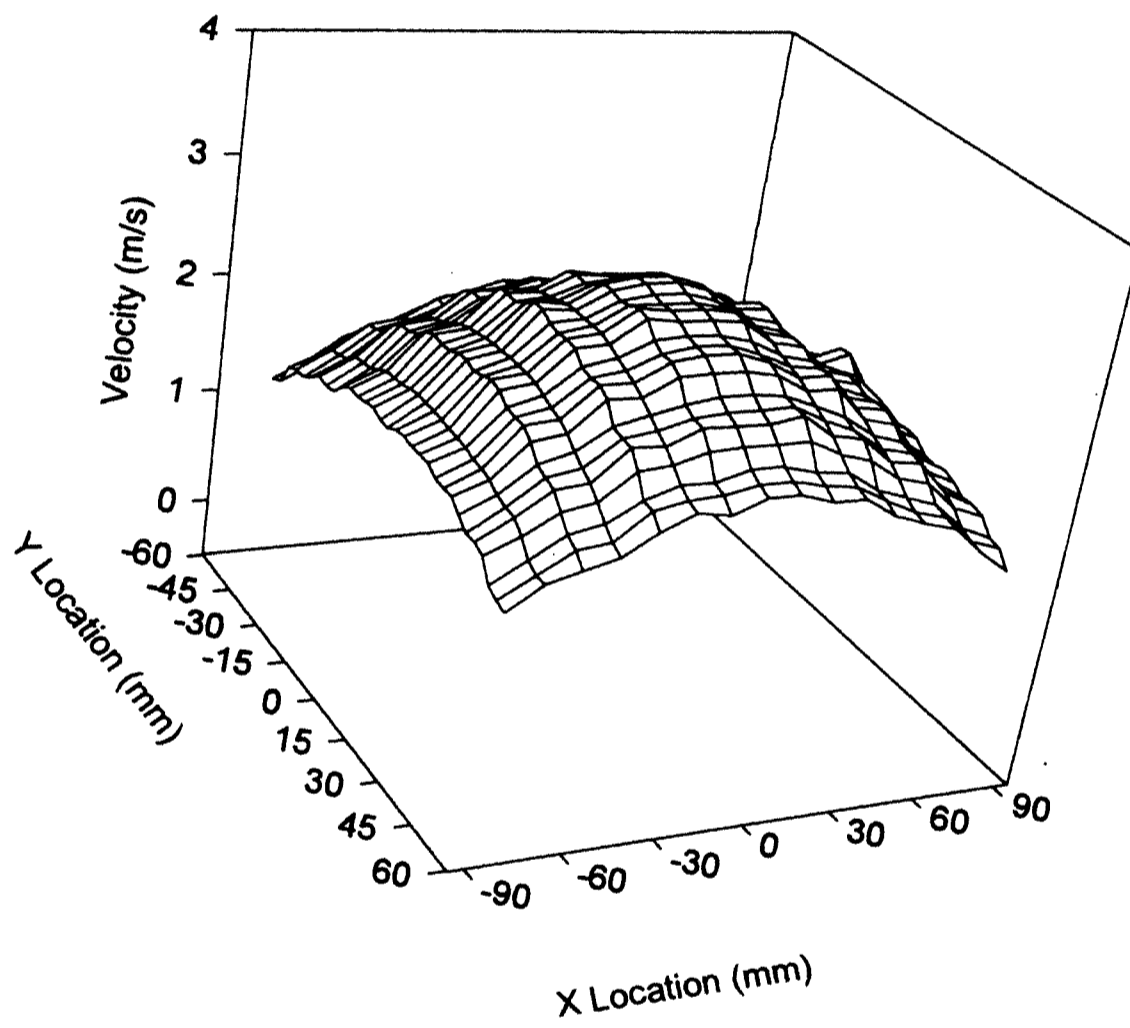


Fig. 3.4 Axial velocity distribution 102 mm upstream of the filter

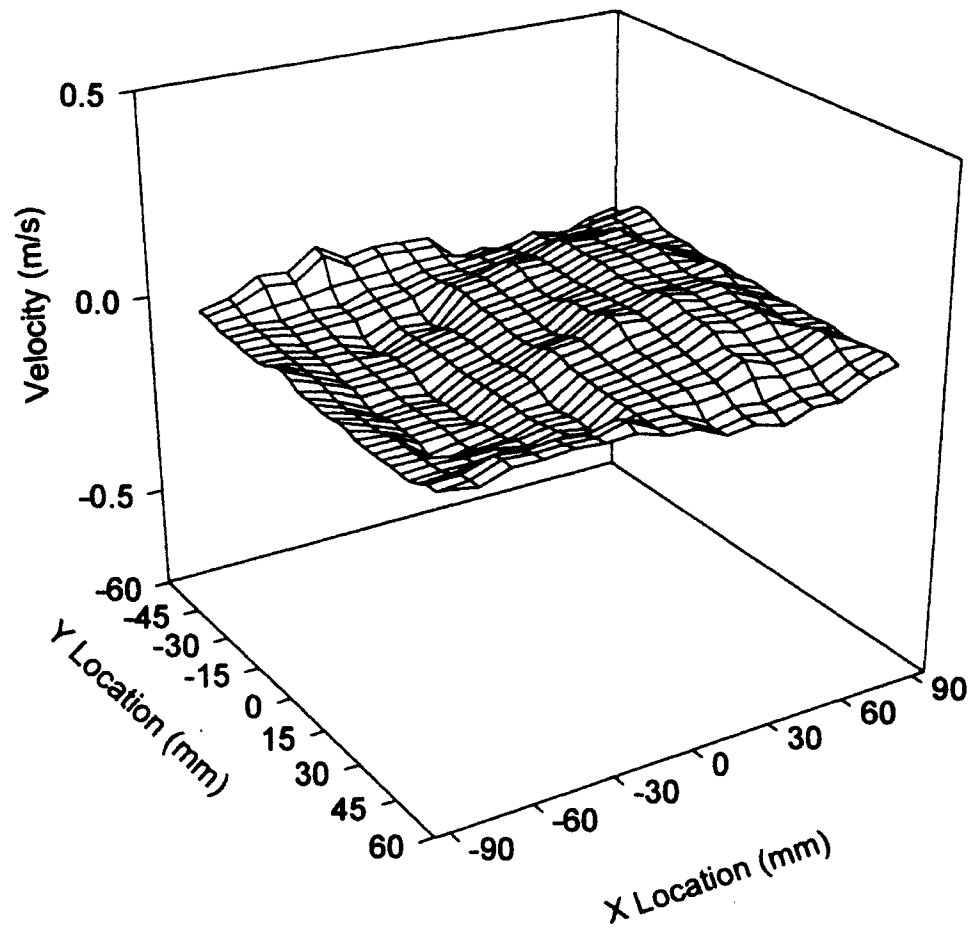


Fig. 3.5 Transverse velocity distribution 102 mm upstream of the filter

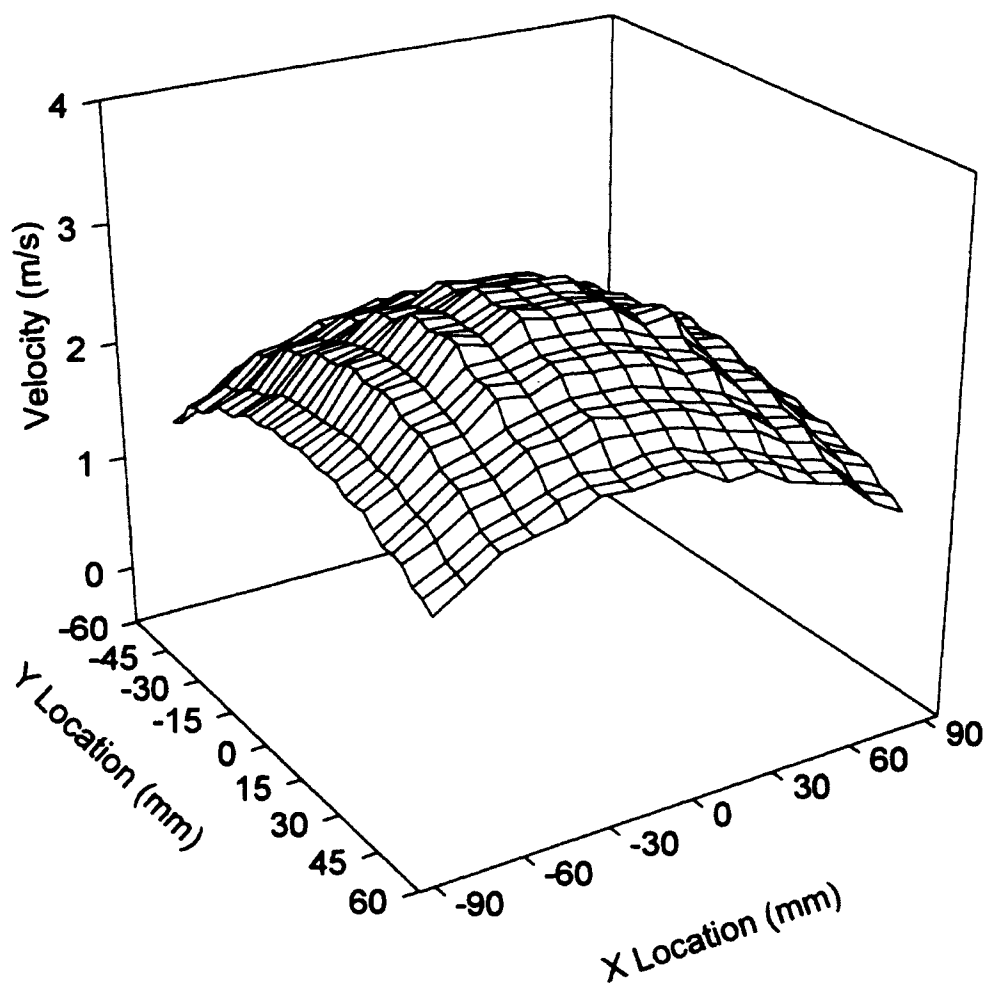


Fig. 3.6 Axial velocity distribution 51 mm upstream of the filter

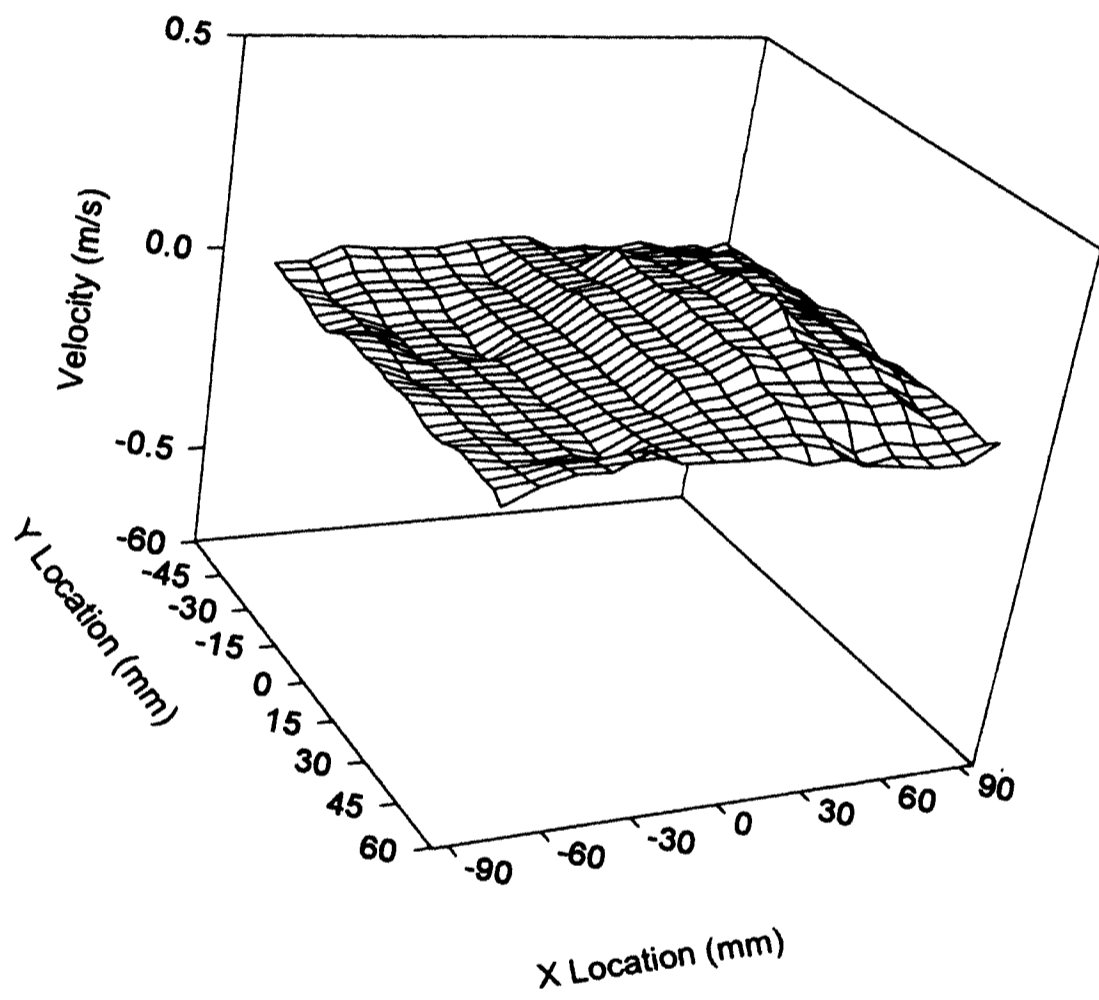


Fig. 3.7 Transverse velocity distribution 51 mm upstream of the filter

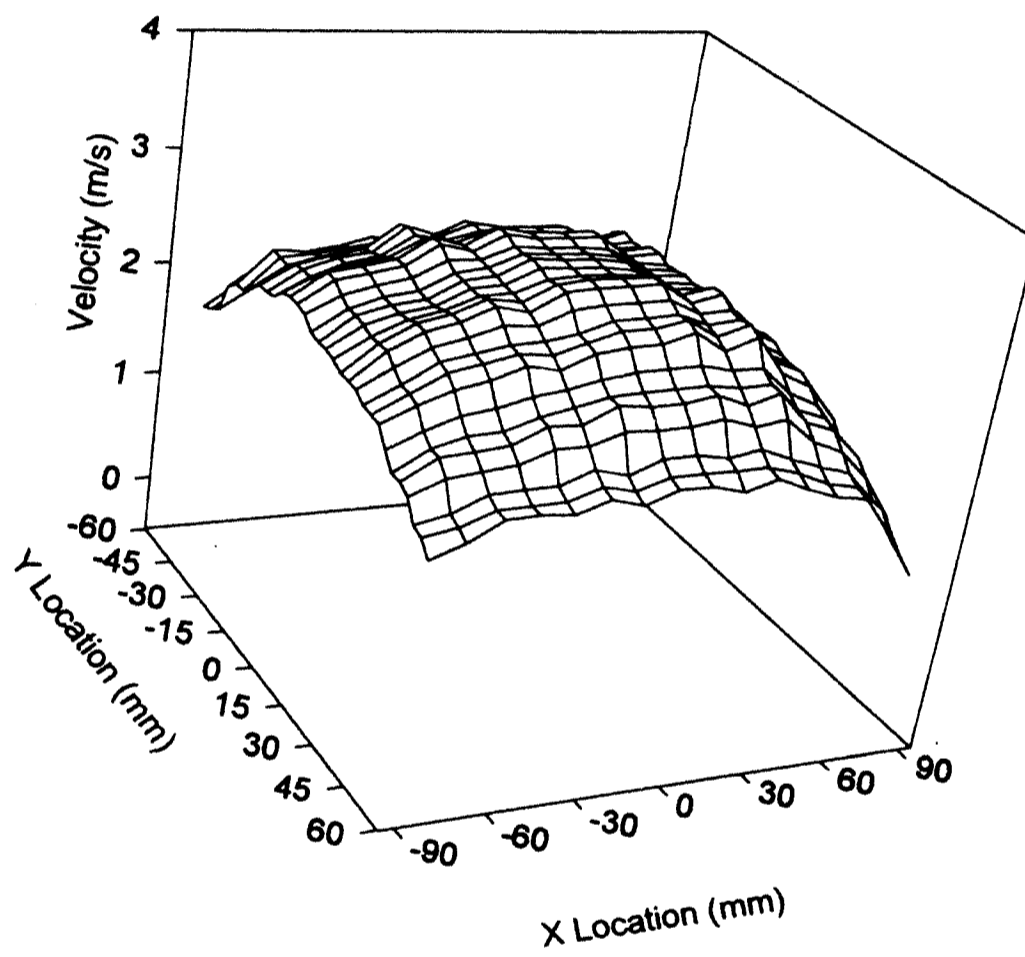


Fig. 3.8 Axial velocity distribution 13 mm upstream of the filter

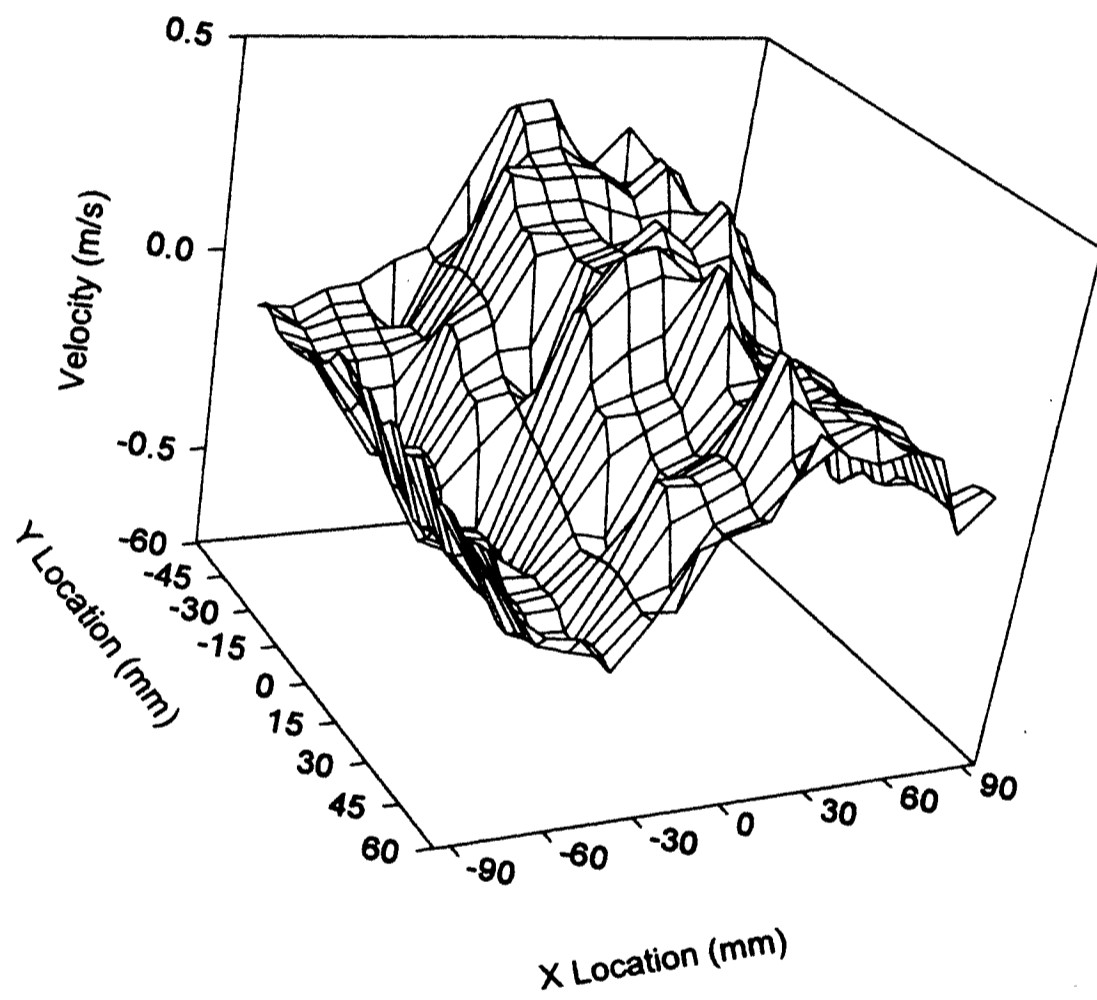


Fig. 3.9 Transverse velocity distribution 13 mm upstream of filter

3.1.4 Comparison of prototype housing data with J726 housing data in a three-dimensional format

By comparing Fig. 3.10 to Fig. 3.11 it is obvious that the prototype housing provides a much more uniform axial velocity distribution to the filter. Fig. 3.10 illustrates the current data collected from the prototype housing in a plane 13 mm upstream of the filter surface, and Fig. 3.11 illustrates data collected by Sabnis (1993) from the J726 housing 13 mm upstream of the filter surface. Sabnis' data only includes points for the front half of the housing, the other half can be assumed to be similar due to symmetry. Only the velocity measurements that are actually over the filter are presented in Fig. 3.11. The velocity distribution surface plot for the J726 housing can be described as a very steeply pitched dome, whereas the similar plot for the prototype housing is quite flat when both are plotted on the same scales.

Fig. 3.12 and Fig. 3.13 illustrate the differences between the transverse velocity distributions in the prototype housing and the J726 housing. Fig. 3.12 offers a look at the transverse velocity distribution 13 mm upstream of the filter surface in the prototype housing. This distribution is obviously quite flat when compared to a similar representation of the transverse velocity distribution in the same plane but in the J726 housing as pictured in Fig. 3.13. However, both distributions are somewhat similar in shape, if not magnitude, with the right side of the distribution offering mostly negative velocities and the left side of the distribution showing generally positive velocities. This illustrates, as noted before, that the flow is attempting to diverge as it strikes the filter. In the J726 housing the filter only comprises a fraction of the exit plane. The flow approaching the filter does not have to

proceed through the filter but can diverge from its path with high transverse velocity magnitudes into the recirculating zones near the walls of the J726 housing.

3.1.5 Turbulence intensities near the filter

The axial turbulence intensity can be found by dividing the local rms value of the axial component of velocity about the local mean axial velocity by the mean axial velocity at the center of the filter. It can be seen from Fig. 3.14 that the J726 housing presents a turbulence intensity profile indicative of a jet, with low turbulence far from the center of the housing increasing to a ringed peak of high turbulence surrounding a central region of somewhat lower turbulence. The prototype housing turbulence intensity profile presented in Fig. 3.15 shows none of these characteristics. For this housing turbulence intensities are quite low all across the housing. This is comparable to duct, or pipe, flow as reported by Hinze (1975) who shows that for duct flow turbulence intensity profiles are quite flat.

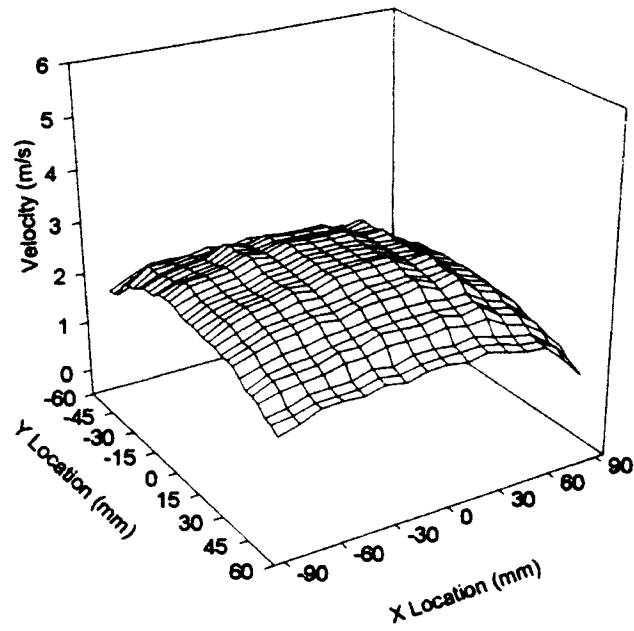


Fig. 3.10 Axial velocity distribution in prototype housing 13 mm upstream of filter

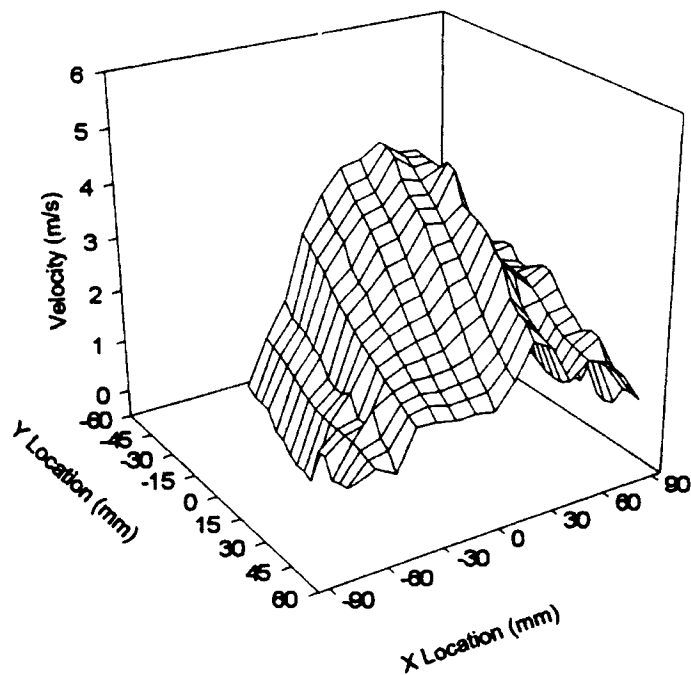


Fig. 3.11 Axial velocity distribution in J726 housing 13 mm upstream of filter

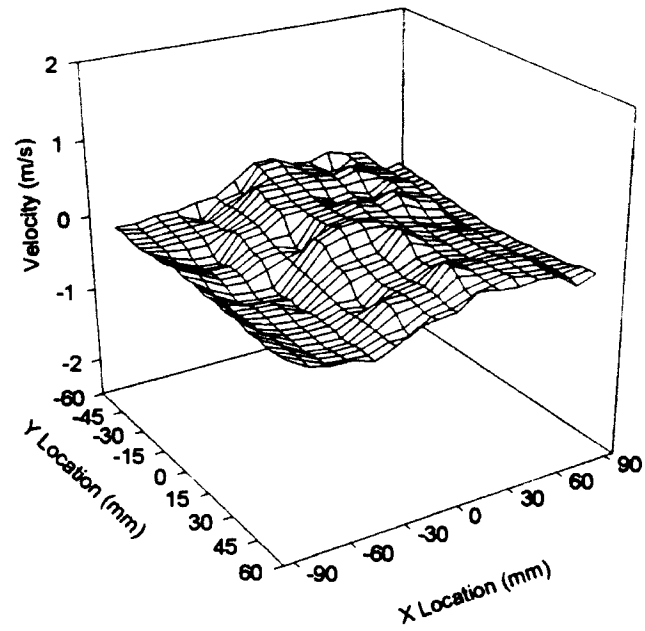


Fig. 3.12 Transverse velocity distribution in prototype housing, 13 mm upstream of filter

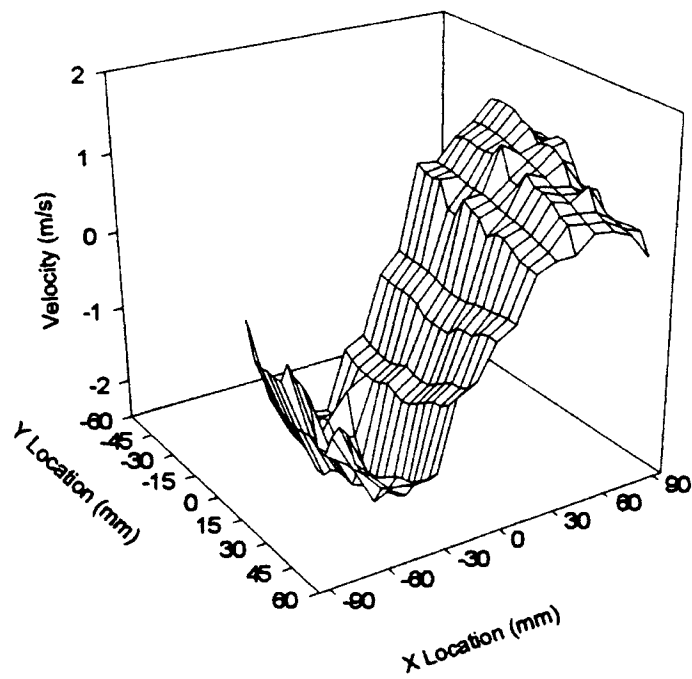


Fig. 3.13 Transverse velocity distribution in J726 housing, 13 mm upstream of filter

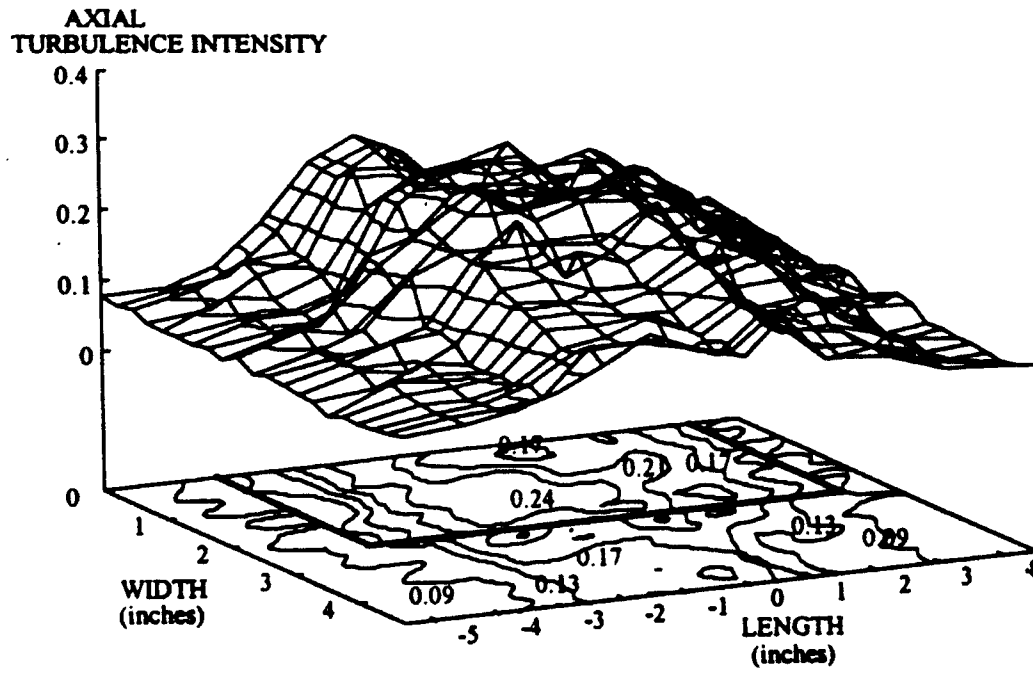


Fig. 3.14 Axial Turbulence Intensity 13 mm upstream of filter for J726 housing (Sabnis 1993)

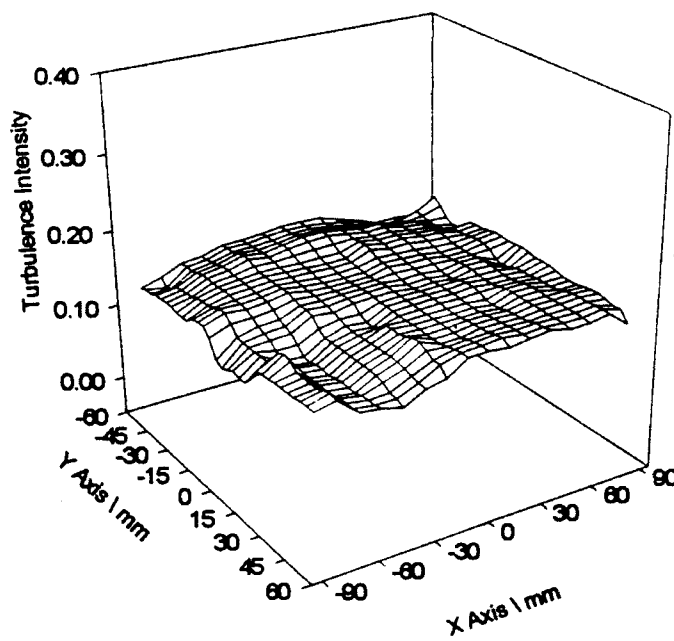


Fig. 3.15 Axial Turbulence Intensity 13 mm upstream of filter in prototype housing

3.2 FLOW VISUALIZATIONS

3.2.1 Laser sheet flow visualization

Fig. 3.16 illustrates a vertical slice of the flow illuminated with laser sheet lighting. The photograph reveals that the flow is very uniform across this cross section of the housing with no separation or zones of recirculation visible. All across the housing the flow followed a similar pattern, or lack of pattern, with uniformity of particle density through the duct and lack of separation at the walls.



Fig. 3.16 Laser sheet lighting of water particles in prototype housing

3.2.2 Flow visualization with tufts

The upstream oriented tufts show that there is a shear stress at the wall and that it points downstream. This suggests that there is no flow separation from the wall or flow recirculation near the wall.

3.3 SUMMARY OF RESULTS

LDV measurements show that the flow in the straight section of the prototype housing near the filter is much like a developed duct flow. The velocity distribution in this section of the housing is shaped like a shallow dome. When compared to the velocity distribution over the filter in the J726 housing, the velocity distribution in the prototype housing can be said to be quite uniform. The peak measured axial velocity of the prototype housing is 104% of its mean axial velocity while the peak axial velocity of the J726 housing is 204% of its mean axial velocity. Flow visualizations revealed no separation at the walls of the prototype housing and no zones of recirculation. The jet flow of the J726 housing, with separation regions between the jet and the walls, is not evident here.

CHAPTER IV

FILTRATION EFFICIENCIES

4.1 EFFICIENCIES OF PLEATED AIR FILTERS

The aerosol velocity inside fibrous filter media is a significant factor in determining the filtration efficiency of that media. Fiber diameters, packing density and particle size are also factors effecting the filtration efficiency. To model the efficiency of our filter media, the fluid velocities of the flow field entering the filter discussed in Chapter III have been used in a computer program to calculate the elemental efficiencies associated with the measured velocities in the area where they were measured, along with the overall efficiency of the filter.

4.1.1 Assumptions

The following assumptions were used in the efficiency calculations:

1. perfect adhesion, $\gamma_o = 1$;
2. no re-entrainment of particles, $\gamma_o = 1$;
3. diffusive filtration mechanisms are not present;
4. particle concentration at filter inlet is uniform, $N_p = Cu_\infty$;
5. the aerosol particles are mono-disperse, $d_p = \text{const.}$;
6. the filter media is packed uniformly, $c = \text{const.}$;
7. the air velocity distribution is uniform through the media, $V_p = \text{const.}$;
8. the filter media contain fibers of a uniform diameter and that diameter is taken to be the weighted average of the fiber diameters found in actual media, $d_f = \text{const.}$; and

9. only initial, clean filter, efficiencies are calculated.

4.1.2 Single fiber efficiencies within pleated fibrous filter media

The single fiber elemental efficiencies calculated for 5 μm particles and 19 μm fiber radii from the velocity distributions measured on the prototype housing are shown in Figure 4.1. The efficiencies are plotted in a 3-D fashion much as the velocity distributions were plotted in Chapter 3, with the borders of the X-Y plane indicating the borders of the filter. The figure shows that single fiber efficiencies are highest near the center of the filter where the velocities are highest and lowest along the edges where the velocities are the lowest. Single fiber efficiencies, even though they vary, can still be considered quite uniform across the filter. This can be compared to the single fiber efficiencies calculated for the J726 housing shown in Figure 4.2. Single fiber efficiencies in the J726 housing fall off quite dramatically on the edges of the filter, but the efficiency peak in the center is greater than 0.7 with the prototype housing never besting 0.6.

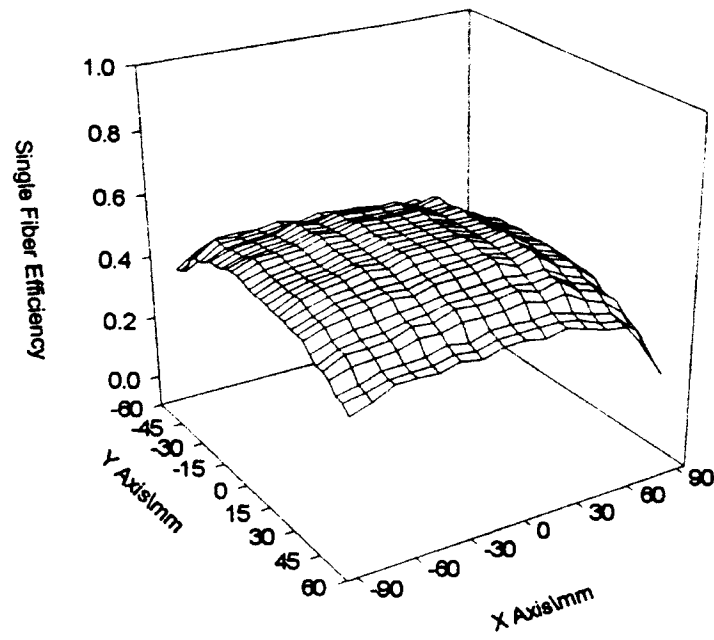


Fig. 4.1 Single fiber efficiencies, prototype housing, 5 μm particles

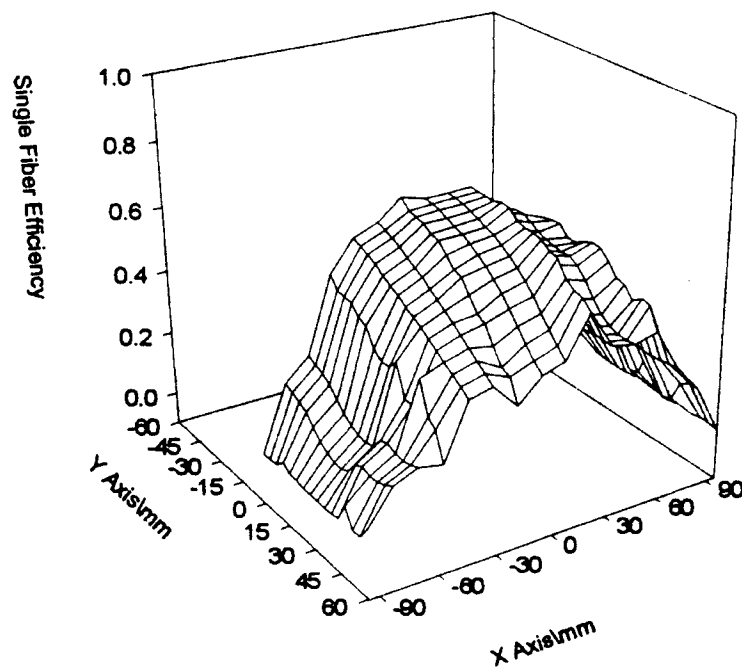


Fig. 4.2 Single fiber efficiencies, J726 housing, 5 μm particles

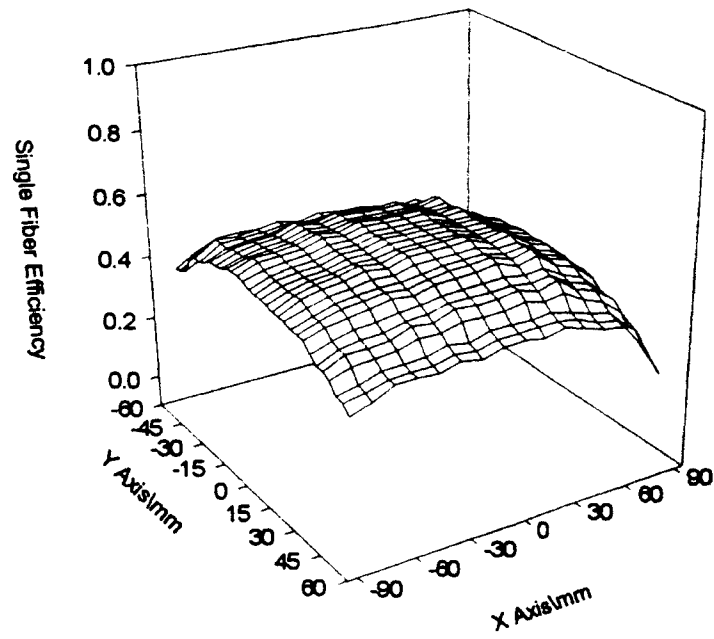


Fig. 4.1 Single fiber efficiencies, prototype housing, 5 μm particles

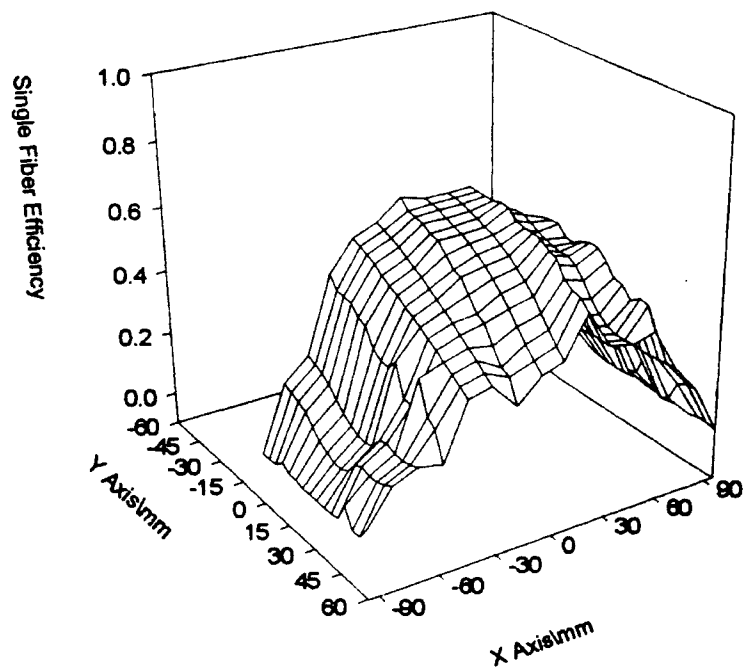


Fig. 4.2 Single fiber efficiencies, J726 housing, 5 μm particles

4.1.3 Bed efficiencies across pleated fibrous filter media

Elemental filter efficiencies for the AF3192 filter mounted in the prototype housing have been obtained by using Equation (1.3) and Equation (1.41). Graphical representation of this data is presented in Fig.'s 4.3 to 4.6.

Figure 4.3 shows that for very small particles, 1 μm in diameter, the filter is very inefficient. The filter's maximum elemental filtration efficiency is only 2.2% with an overall filter efficiency, as obtained from Equation (1.5), of 2.0%. When subjected to 2.5 μm particles, as shown in Figure 4.4, the filter does a much better job of filtration. The effect of fluid velocity on filtration efficiency is clearly visible here with the highest efficiencies in the center of the filter where the velocities are higher. The overall filter efficiency for 2.5 μm particles is 36%. Figure 4.5 illustrates the elemental efficiency profile for a mono-disperse aerosol of 5 μm particles and shows the depth type filter coming into its own with the elemental efficiencies averaging 94.5%. The maximum calculated efficiency was 98% and the minimum was 68%. Clearly most of the filter is operating in an efficiency range greater than 95% giving an overall filter efficiency of 96%. Figure 4.6 provides a view of particle capture efficiency using the prototype housing and the smallest particle, 9.2 μm , that would produce a calculated efficiency of over 99% in each element.

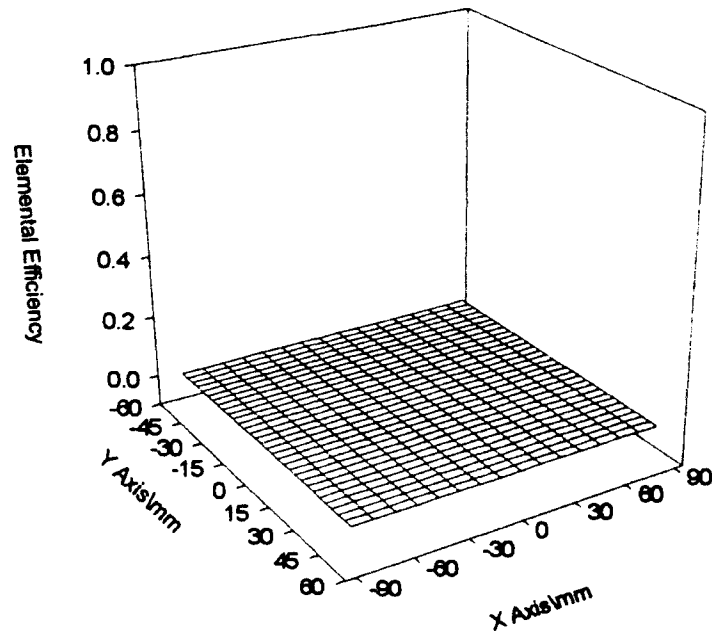


Fig. 4.3 Elemental efficiencies for filter AF3192, prototype housing, 1 µm particle size

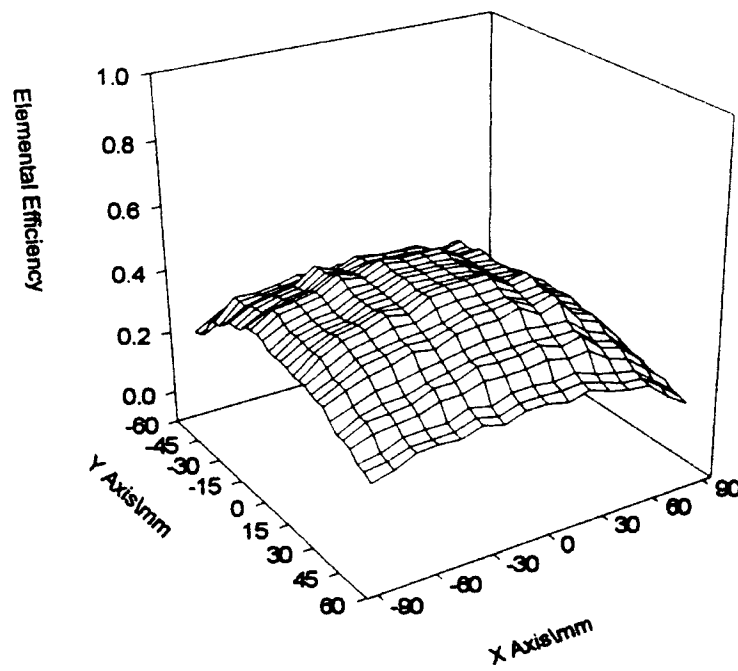


Fig. 4.4 Elemental efficiencies for filter AF3192, prototype housing, 2.5 µm particle size

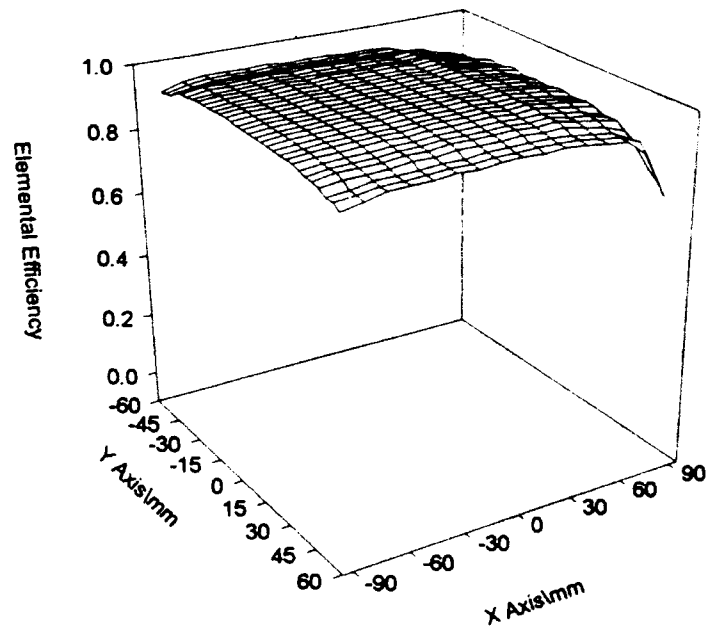


Fig. 4.5 Elemental efficiencies for filter AF3192, prototype housing, 5 μm particle size

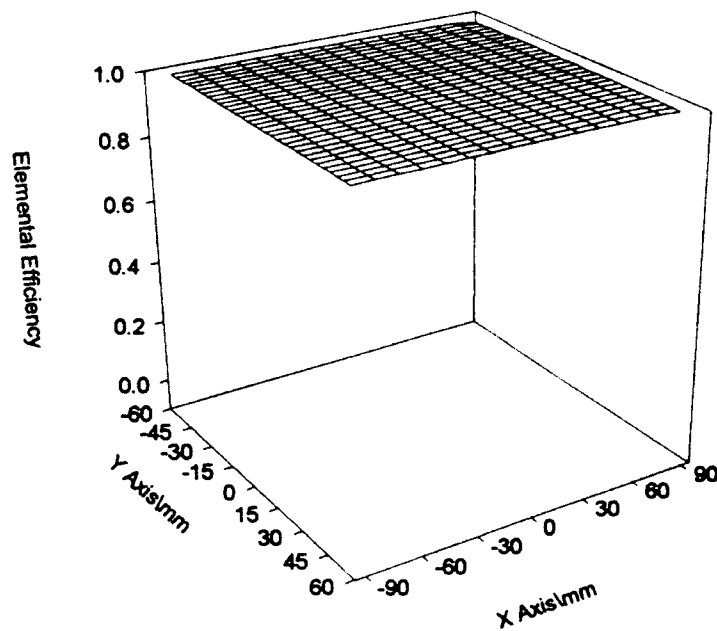


Fig. 4.6 Elemental efficiencies for filter AF3192, prototype housing, 9.2 μm particle size

4.1.4 Comparison of elemental bed efficiencies in the prototype housing to those in the J726 housing

As discussed previously in Section 4.1.3, the elemental efficiencies for 1 μm particles are quite low. This is quite evident in Figs. 4.7 and 4.8. Neither the prototype housing nor the J726 housing can produce an elemental efficiency of greater than 4.5% when using 1 μm particles. The J726 housing has a pronounced efficiency peak in the center of the filter, as compared to the prototype housing, which is quite uniform throughout and never reaches an elemental efficiency of greater than 2.2%. This peak results in the J726 housing having a greater overall efficiency than that of the prototype housing at 2.5% versus 2.0%.

Figure 4.9 and Figure 4.10 compare elemental efficiencies obtained with 2.5 μm particles in the prototype and J726 housing. As with the 1 μm particles, the J726 housing has a pronounced efficiency peak in the center of the filter. Higher efficiencies than the prototype housing are observed in the center of the filter, but lower efficiencies than the prototype housing can be found along the edges of the filter. The aerosol velocity profile provided by the J726 housing creates a significantly better overall filter efficiency at 51% as compared to the prototype housing's 36%.

Beginning with Figs. 4.11 and 4.12, the prototype housing begins to show the benefits of a more uniform velocity profile. The J726 housing still shows an efficiency peak in the center of the filter with sharp drop-offs in efficiency near the edges of the filter. This results in an overall efficiency of 95% for the J726 housing. The more uniform efficiency profile of the prototype housing yields an overall filter efficiency of 96%.

Figure 4.13 and Figure 4.14 compare the elemental efficiency profiles of the prototype housing to that of the J726 housing for the smallest particle, 9.2 μm , in which all the elemental efficiencies calculated for the prototype housing are above 99%. The J726 housing requires a particle size of nearly 20 μm for the elemental efficiencies across the filter to be uniformly above 99%. The overall efficiency of the prototype housing is 99.7% at this particle size compared to the 99.5% efficiency of the J726 housing. This small difference in efficiency means that the J726 housing would allow 67% more of these potentially damaging particles through the filter than would be allowed by the prototype housing.

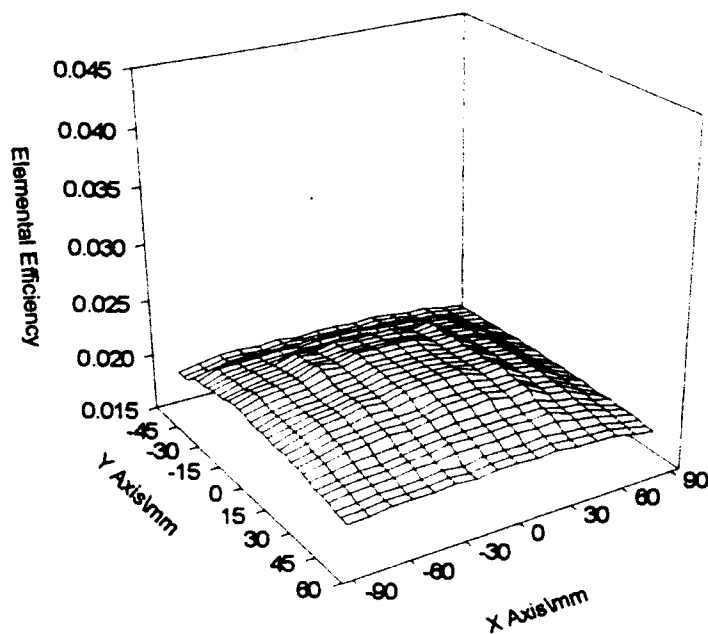


Fig. 4.7 Elemental efficiencies for filter AF3192, prototype housing, 1 μm particle size

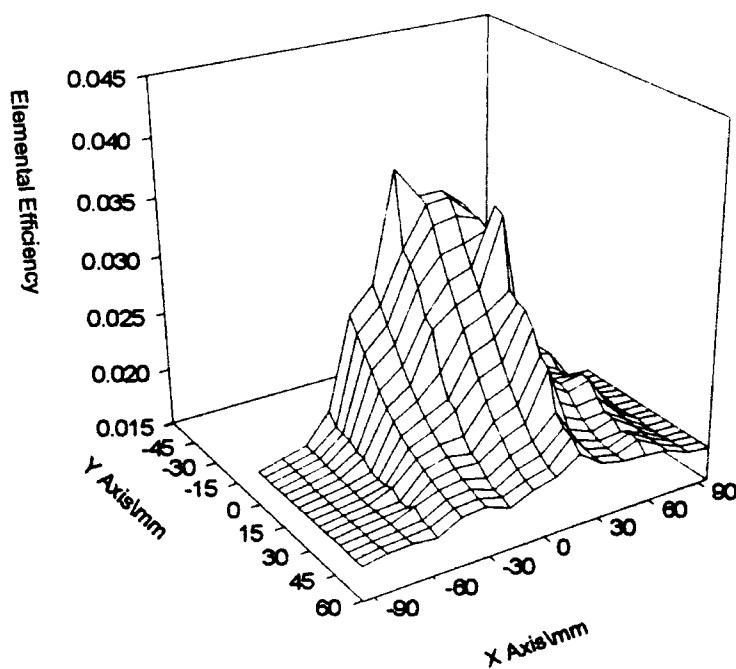


Fig. 4.8 Elemental efficiencies for filter AF3192, J726 housing, 1 μm particle size

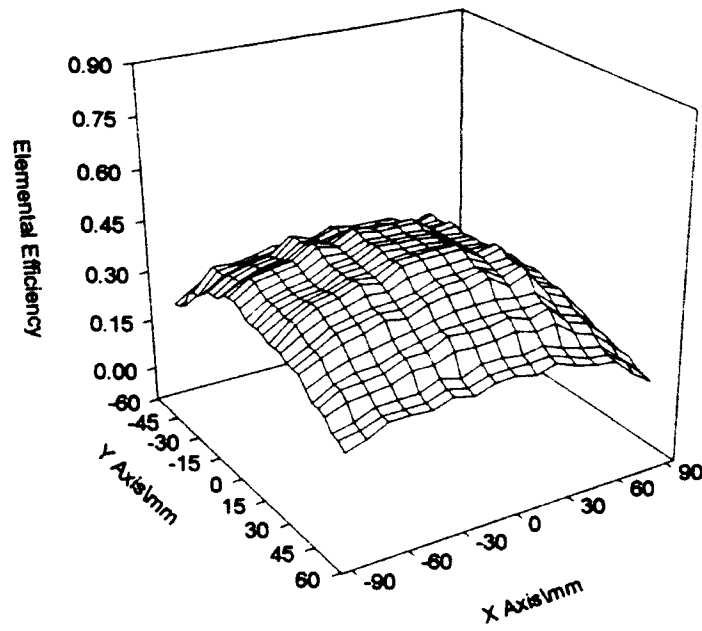


Fig. 4.9 Elemental efficiencies for filter AF3192, prototype housing, 2.5 μm particle size

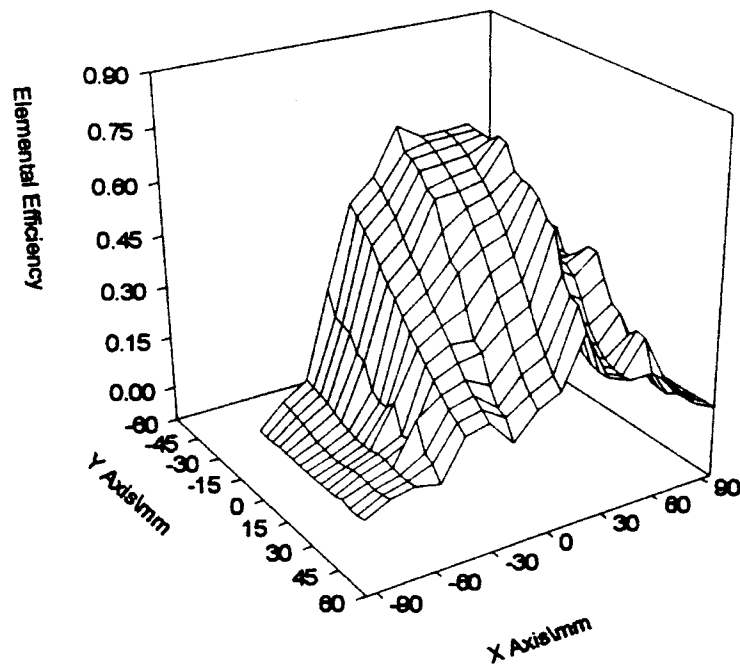


Fig. 4.10 Elemental efficiencies for filter AF3192, J726 housing, 2.5 μm particle size

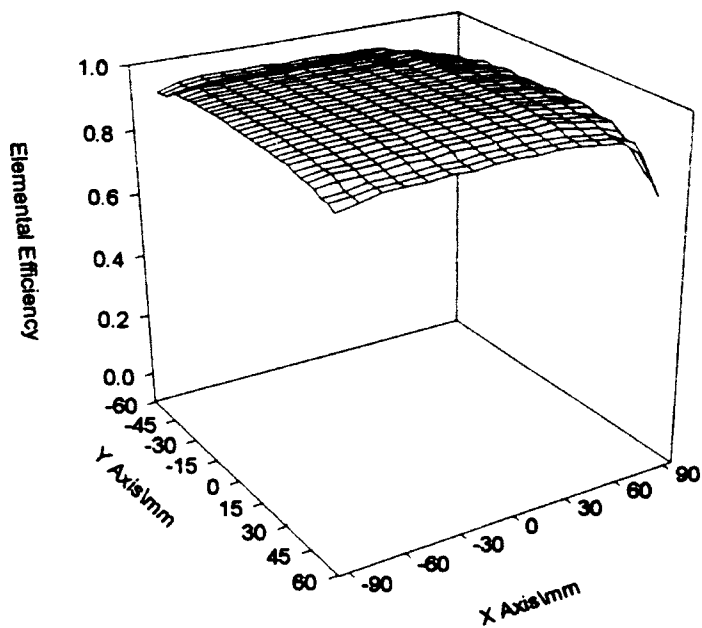


Fig. 4.11 Elemental efficiencies for filter AF3192, prototype housing, 5 μm particle size

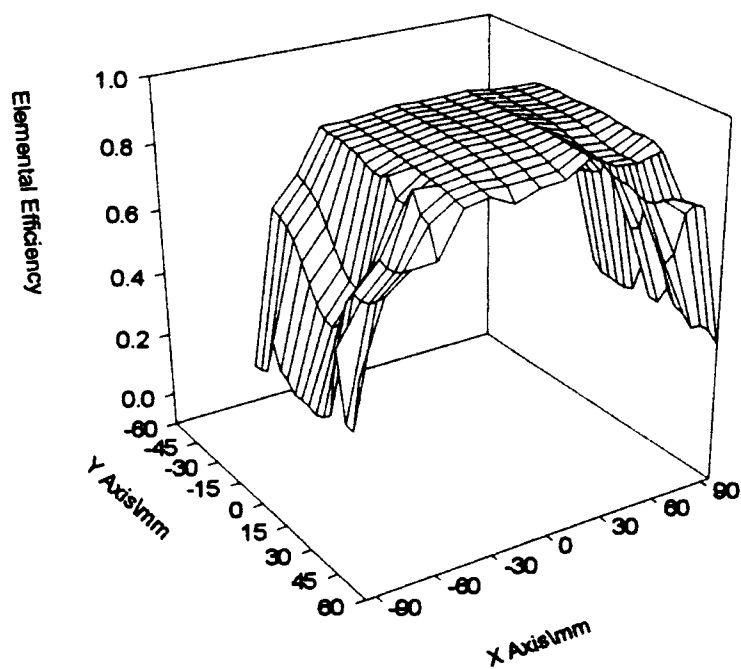


Fig. 4.12 Elemental efficiencies for filter AF3192, J726 housing, 5 μm particle size

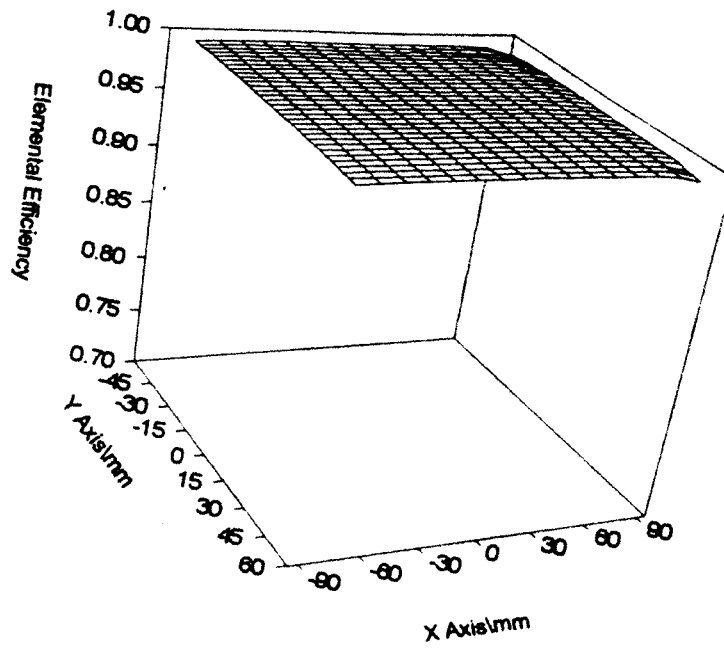


Fig. 4.13 Elemental efficiencies for filter AF3192, prototype housing, 9.2 μm particle size

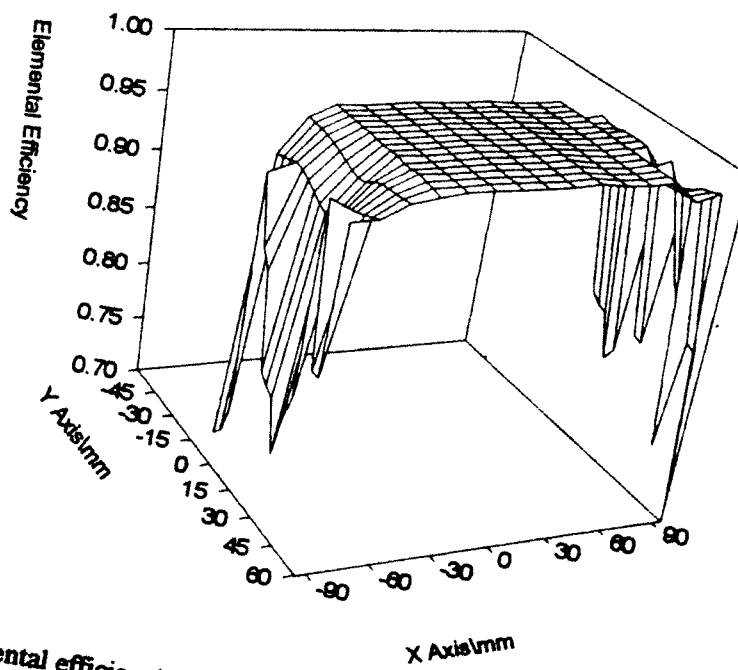


Fig. 4.14 Elemental efficiencies for filter AF3192, J726 housing, 9.2 μm particle size

4.1.5 Overall filter efficiency comparisons

Table 4.1 compares the calculated overall filter efficiencies for the measured velocity distributions found in the prototype housing and the J726 housing to filter efficiencies calculated for a hypothetical uniform velocity distribution. The efficiencies for very small particles are shown to be very low no matter which velocity distribution is chosen, with the efficiency being slightly lower for the more uniform velocity distributions. For all velocity distributions, the efficiency is nearly 100% for particles 20 μm in diameter or larger. It can be seen that the prototype housing creates filtration efficiencies very similar to those forecast for a perfectly uniform velocity profile.

Table 4.1 Overall filter efficiencies calculated for the prototype and J726 housing velocity distributions and a uniform velocity distribution, particle number distribution assumed constant

Particle diameter	Overall filter efficiency, η		
	Prototype housing	J726 housing	Uniform velocity distribution
1.0 μm	0.020	0.025	0.020
2.5 μm	0.356	0.511	0.304
5.0 μm	0.961	0.951	0.961
9.2 μm	0.997	0.995	0.997
20.0 μm	0.999	0.999	0.999
	Overall filter penetration, $1-\eta$		
1.0 μm	0.980	0.975	0.981
2.5 μm	0.644	0.489	0.696
5.0 μm	0.039	0.049	0.039
9.2 μm	0.003	0.005	0.003
20.0 μm	0.001	0.001	0.001

Where my calculations given in Chapter 4 indicate that the overall efficiency for 1 μm particles in the prototype housing should be around 2% at a flow rate of 111 scfm, their measurements indicate an overall efficiency of around 40%. Five micron particles by my calculations give an overall filter efficiency of 96% but measurements by Liang et al. give the filter an efficiency of only 70% with 5.3 μm particles. Reasons for these discrepancies are unclear, but could involve the effects of diffusional filtration for small particles and bounce and reentrainment of particles into the airstream for large particles.

4.1.6 Adhesion considerations

Up to now all efficiency calculations were made assuming that there was no particle bounce upon striking a fiber and no reentrainment of particles into the airstream, i.e., any particle once captured by a fiber is concretely bound to it and cannot be recaptured by the airstream. In practice this is not always the case. At sufficiently high aerosol velocities, particles may bounce away from a fiber due to rebound forces being greater than adhesion forces, and the drag force acting on a particle already stuck to a fiber may become strong enough to overcome the adhesive force that holds the particle to a fiber. Either of these actions would result in reentrainment of the particle into the airstream. Equation (1.49) was used to combine the adhesive probability factor, γ_0 , developed by Ptak & Jaroszczyk (1990), Equation (1.52), with Sabnis' (1993) inertial impaction Equation (1.42). Elemental collection efficiencies along with overall filter collection efficiencies were calculated for both the J726 housing data and the prototype housing data using several different particle sizes.

Table 4.2 Overall filter efficiencies calculated for the prototype and J726 housing velocity distributions and a uniform velocity distribution, accounting for non-perfect adhesion of particles to fiber surfaces, particle number distribution assumed constant

Particle diameter	Overall filter efficiency, accounting for adhesive probability		
	Prototype housing	J726 housing	Uniform velocity distribution
1.0 μm	0.019	0.022	0.019
2.5 μm	0.333	0.480	0.285
5.0 μm	0.944	0.937	0.944
9.2 μm	0.992	0.990	0.992
20.0 μm	0.994	0.992	0.994
	Percent more dust penetrating filter using the assumption of non-perfect adhesion versus the assumption of perfect adhesion, %		
1.0 μm	0.1	0.3	0.0
2.5 μm	3.6	6.3	2.7
5.0 μm	43.6	28.6	43.6
9.2 μm	166.7	100.0	166.7
20.0 μm	500.0	700.0	500.0

Table 4.2 illustrates the calculated overall filter efficiency and difference in the amount of penetrating dust, when accounting for the effects of particle bounce and reentrainment, of the AF3192 filter mounted in either the prototype housing or the J726 housing along with a uniform velocity distribution. For all particle sizes the overall filter efficiency dropped when the effect of non-perfect adhesion was taken into account with the smaller particles showing a more dramatic change than larger ones. With the small particles having such a low collision efficiency, any change in the adhesive probability could have a significant effect upon the overall efficiency of the filter. Changes in the elemental efficiency were too small to be seen in the 3-D representations of filtration

efficiency as shown in section 4.1.3, but Figure 4.15 compares the changes on a slice of the filter in a 2-D form. The differences are obvious yet small and increase with velocity, being most significant in the center of the filter where the velocities are highest and least significant along the edges of the filter where the aerosol velocities are at their lowest magnitude.

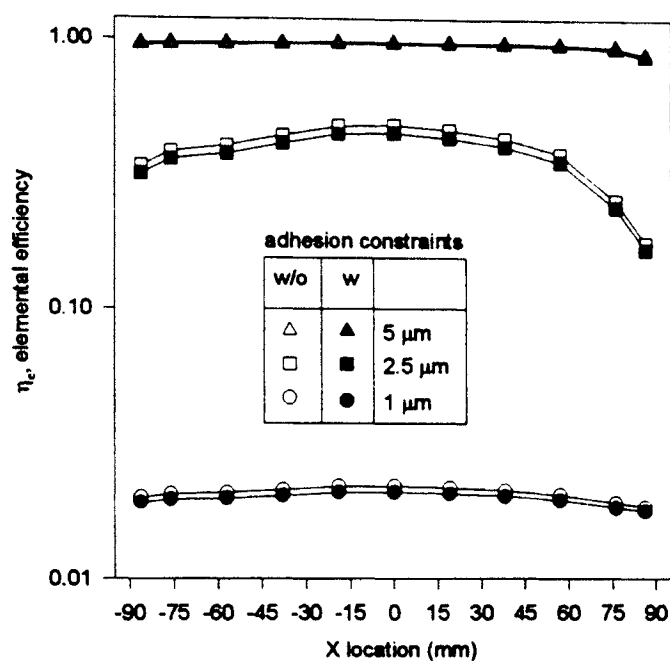


Fig. 4.15 Comparison of elemental efficiencies with consideration and without consideration of the effects of adhesion along the y-centerline of the prototype housing for several different particle sizes

4.1.7 Particle number distribution considerations

By using data gathered by Liang et al. (1994), Figure 4.16, I have produced a second order polynomial function relating the particle number density to the upstream velocity, Equation (4.1). The particle number density at a zero aerosol velocity condition was assumed to be equal to the particle number density measured at the lowest velocity.

$$C = 2.796 \times 10^8 - 3.443 \times 10^6 u_0 + 7.986 \times 10^3 u_0^2 \quad (4.1)$$

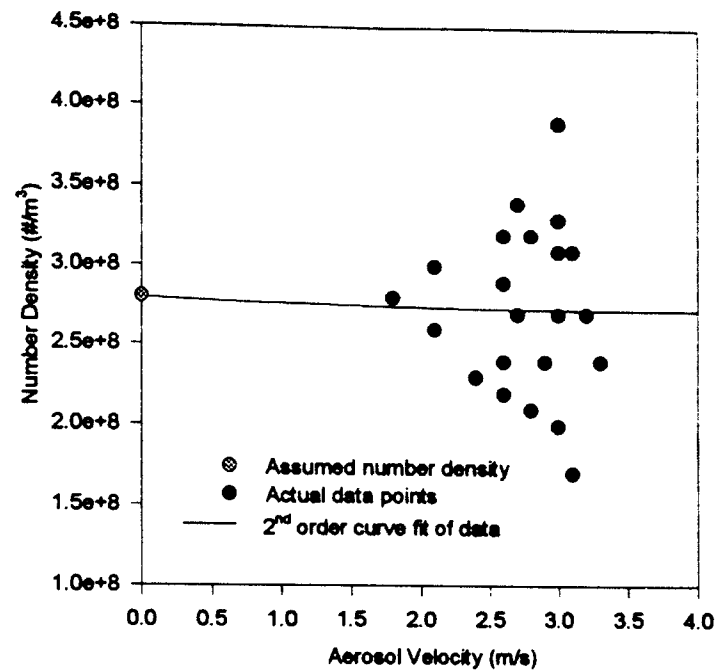


Fig. 4.16 Particle concentration upstream of filter (prototype housing, 0.966 μm particles)

Using Equation (4.1), which is basically a constant, as the weighting function for particle number density in the overall efficiency calculations, I was able to obtain Table 4.3. It should be noted that Equation (4.1) is a curve fit of number density versus velocity data for 1 μm particles. Equation (4.1) is approximate in nature and may not apply to other size particles, as they may have more marked dependencies on aerosol velocity.

Table 4.3 Overall filter efficiencies calculated for the prototype and J726 housing velocity distributions and a uniform velocity distribution, using Equation (4.1) for particle number distribution values

Particle diameter	Overall filter efficiency, η		
	Prototype housing	J726 housing	Uniform velocity distribution
1.0 μm	0.020	0.025	0.020
2.5 μm	0.356	0.510	0.304
5.0 μm	0.961	0.951	0.961
9.2 μm	0.997	0.995	0.997

Obviously the inclusion of Equation (4.1) into the calculation of overall filter efficiencies made little difference to the outcome of the calculations. The only difference that can be seen in Table 4.3 when comparing it to Table 4.1 is the entry for 2.5 μm particles in the J726 housing. Table 4.1 lists the entry as 0.511 and Table 4.3 lists the same entry as 0.510. This difference is insignificant, suggesting that the assumption of constant particle number density distribution may be valid or, at least, that the particle number density distribution is not a function of the measured aerosol velocities.

4.2 SUMMARY

Single fiber elemental efficiencies calculated for the prototype housing flow field and the J726 housing flow field indicate that the efficiencies in the prototype housing are quite uniform, but the J726 housing efficiencies have a definite peak of high efficiency in the center of the filter with lower efficiencies found along the edges of the filter. Elemental bed efficiencies of the filter in both housings indicate similar findings with the prototype housing offering a very uniform efficiency profile with all particle diameter sizes, when compared with the J726 housing's corresponding efficiency profiles which all exhibit very

strong peaks of filtration efficiency in the center of the filter with very low efficiencies along the filter edges. This peakiness tends to help the J726 housing with overall filtration efficiency with small particles, but hurts it with large particles. The smallest particle that will be filtered with more than 99% efficiency in all elements of the J726 housing is 25 μm in diameter. The similar particle in the prototype housing is 9.2 μm in diameter.

The effects of adhesive probability appeared to be almost universal. The J726 housing did not really fare much worse than the prototype housing, except for the very small particle size (1 μm), where the J726 housing was affected more profoundly than the prototype housing and the uniform velocity distribution. This decrease in efficiency would probably not be too noticeable in practice using a polydisperse dust because the filtration efficiency for 1 μm particles is very low.

Study of the particle density distribution effects on the overall filter efficiency suggests that the actual particle density distribution in the housing is not dependent upon velocity and is sufficiently uniform to consider it as uniform.

CHAPTER V

CONCLUSIONS AND RECOMMENDATIONS

5.1 CONCLUSIONS

The following conclusions can be drawn from this work:

1. The flow field inside the prototype housing is much like a developed duct flow and is not separated from the housing walls.
2. When compared to the J726 housing's jet like flow, the prototype housing provides a very uniform flow pattern to the filter.
3. It is satisfactory to treat the interception and inertial impaction models of particle collection efficiency as independent of each other to model the inertial interception and impaction collection efficiency of a single fiber, even though inertial interception and impaction are not independent of each other.
4. Initial particle collection efficiencies are strongly dependent upon both aerosol velocity and particle size. Higher velocities and larger particles generate higher efficiencies than lower velocities and small particles.
5. Fibrous filters offer very low filtration efficiencies for particles 1 μm in diameter or smaller. For these small particles, the J726 housing has a higher, yet still very poor, initial overall filtration efficiency than the prototype housing.
6. Large particles, 5 μm and larger, are filtered more efficiently by the prototype housing. The J726 housing would allow 67% more 9.2 μm particles to pass through the filter than the prototype housing would.

7. For most particle sizes, the effect of adhesive probability on the initial filtration efficiency of the filter is very small, showing less than a 2% difference from the perfect adhesion model, with only very small particles, which are filtered very inefficiently anyway, showing a large difference.
8. Particle number density distribution in the flow field upstream of the filter is not dependent upon velocity. The assumption of uniform particle number density distribution in the calculation of overall filter efficiency may be a valid one.

5.2 RECOMMENDATIONS FOR FUTURE WORK

Further study of fibrous depth filter efficiency could be done in the following areas:

1. Adhesion effects should be studied experimentally using liquid particles, which should have an adhesive probability of $\gamma_0 = 1$, and test dust, which will have an adhesive probability less than one, to more accurately model the effects of adhesion in typical automotive air filtration applications.
2. Experimental values of initial filtration efficiencies should be determined using both the J726 test housing and the prototype test housing for comparison with values presented in this paper.
3. Models could be developed that include the effects of dust loading in the filtration analysis providing a view of filtration efficiency over the life of the filter rather than just the initial efficiency.
4. The effects of non-uniform filter element fiber diameters should be taken into account by possibly modeling the filter as a composite of several layers with each layer containing a different fiber diameter.

REFERENCES

- Aerometrics (1992): Doppler Signal Analyzer for Phase Doppler Particle Sizing Applications User's Manual, Sunnyvale, CA, draft 2.
- Benedict, R.P. (1984): Fundamentals of Temperature, Pressure and Flow Measurements, John Wiley & Sons, Inc., New York, 3rd ed.
- Brach, R.M. & Dunn, P.F. (1992): "A Mathematical Model of the Impact and Adhesion of Microspheres," *Aerosol Science and Technology*, Vol. 16, pp. 51-64.
- Brewer, J.M. & Goren, S.L. (1984): "Evaluation of Metal Oxide Whiskers Grown on Screens for Use as Aerosol Filtration Media," *Aerosol Science and Technology*, Vol. 3, No. 4, pp. 411-429.
- Brown, R.C. (1993): Air Filtration: An Integrated Approach to the Theory and Applications of Fibrous Filters, Pergamon Press, Oxford.
- Burden, R.L. & Faires, J.D. (1993): Numerical Analysis, PWS Publishing Company, Boston, 5th Ed.
- Cai, Q. (1993): "A Study of Air Filter Flow By Computational Fluid Dynamics," M.S. Thesis, Oklahoma State University, Department of Mechanical and Aerospace Engineering, Stillwater, OK.
- Davies, C.N. (1973): Air Filtration, Academic Press, New York.
- Ellenbecker, M.J., Leith, D., & Price, J.M. (1980): "Impaction and Particle Bounce at High Stokes Numbers," *Journal of the Air Pollution Control Association*, November, Vol. 30, No. 11, pp. 1224-1227.
- Fan, K.C., Wamsley, B., & Gentry, J.W. (1977): "The Effect of Stokes and Reynolds Numbers on the Collection Efficiency of Grid Filters," *Journal of Colloid and Interface Science*, Vol. 65, No. 1, pp. 162-173.
- Flagan, R.C. & Seinfeld, J.H. (1988): Fundamentals of Air Pollution Engineering, Prentice Hall, Englewood Cliffs, NJ.
- Gould, R.D. & Loseke, K.W. (1993): "A Comparison of Four Velocity Bias Correction Techniques in Laser Doppler Velocimetry," *Journal of Fluids Engineering*, Vol. 112, pp. 508-514.

- Grant, D.C., Liu, B.Y.H., Fisher, W.G., & Bowling, R.A. (1989): "Particle Capture Mechanisms in Gases and Liquids: An Analysis of Operative Mechanisms in Membrane/Fibrous Filters," *The Journal of Environmental Sciences*, July/August, pp. 43-51.
- Haldhani, M.K. (1993): "Particle Number Density Distribution and Its Time History for an Automotive Air Filter," M.S. Thesis, Oklahoma State University, Department of Mechanical and Aerospace Engineering, Stillwater, OK.
- Harrop, J.A. & Stenhouse, J.I.T. (1969): "The Theoretical Prediction of Inertial Impaction Efficiencies in Fibrous Filters," *Chemical Engineering Science*, Vol. 24, pp. 1475-1481.
- Hinze, J.O. (1975): Turbulence, McGraw Hill, 2nd Ed.
- Hitoshi, E., Okuyama, K., & Adachi, M. (1977): "The Effect of Neighbouring Fibers on the Single Fiber Inertia-Impaction Efficiency of Aerosols," *Journal of Chemical Engineering of Japan*, Vol. 10, No. 2, pp. 148-153.
- Hornbeck, R.W. (1975): Numerical Methods, Prentice Hall, Englewood Cliffs, NJ.
- Jaroszcyk, T. & Wake, J. (1991): "Critical Aerosol Velocity in Nonwoven Filtration," TAPPI Proceedings, Nonwoven Conference, pp. 125-135.
- Jaroszcyk, T., Wake, J., & Connor, M.J. (1993a): "Automotive Engine Air Filter Media Performance," The Filtration Society, Filtech Conference, Karlsruhe, Germany.
- Jaroszcyk, T., Wake, J., & Connor, M.J. (1993b): "Factors Affecting the Performance of Engine Air Filters," American Society of Mechanical Engineers, Energy-Sources Technology Conference & Exhibition, Houston, TX.
- Kays, W.M. & Crawford, M.E. (1993): Convective Heat and Mass Transfer, McGraw-Hill, Inc., New York, 3rd ed.
- Kuwabara, S. (1959): "The Forces Experienced by Randomly Distributed Parallel Circular Cylinders or Spheres in a Viscous Flow at Small Reynolds Numbers," *Journal of the Physical Society of Japan*, April, Vol. 14, No. 4, pp. 527-532.
- Landahl, H.D. & Herrmann, R.G. (1949): "Sampling of Liquid Aerosols by Wires, Cylinders, and Slides, and the Efficiency of Impaction of the Droplets," *Journal of Colloid Science*, April, pp. 103-136.
- Lee, K.W. & Liu, B.Y.H. (1980): "On the Minimum Efficiency and the Most Penetrating Particle Size for Fibrous Filters," *Journal of the Air Pollution Control Association*, Vol. 30, No. 4, April, pp. 377-381.

- Lee, K.W. & Liu, B.Y.H. (1982a): "Experimental Study of Aerosol Filtration by Fibrous Filters," *Aerosol Science and Technology*, Vol. 1, pp. 35-46.
- Lee, K.W. & Liu, B.Y.H. (1982b): "Theoretical Study of Aerosol Filtration by Fibrous Filters," *Aerosol Science and Technology*, Vol. 1, pp. 147-161.
- Liang, F., Natarajan, B., Tian, Y, & Dougherty, R.L. (1994): "Panel Filter Local Efficiency Measurements as Applied to Automotive Engine and Cabin Air Filtration," *Symposium on Automotive Filtration*, 25th Annual Meeting of the Fine Particle Society, East Brunswick, NJ.
- Lilley, D.G. (1993): Computational Fluid Dynamics, Department of Mechanical and Aerospace Engineering, Oklahoma State University, Stillwater, OK.
- Löffler, F. (1970): "Separation Efficiency and Pressure Loss of Filter Materials of Different Structure, at Differing Conditions," *Staub-Reinhalt Luft*, December, Vol. 30, No. 12, pp. 27-31.
- Löffler, F. (1971): "Collection of Particles by Fiber Filters," in Air Pollution Control (Edited by Strauss, W.), John Wiley & Sons, Inc., New York.
- Löffler, F. (1972): "Blow-off of Particles Collected on Filter Fibres," *Filtration & Separation*, Nov./Dec., pp. 688-694.
- Meyers, E. (1994): Personal communication, April 29, Flint, MI.
- Pich, J. (1966): "Theory of Aerosol Filtration by Fibrous and Membrane Filters," in Aerosol Science (Edited by Davies, C.N.), Academic Press, New York.
- Press, W.H., Teukolsky, S.A., Vetterling, W.T., & Flannery, B.P. (1992): Numerical Recipes in C, The Art of Scientific Computing, Cambridge University Press, New York, 2nd ed.
- Ptak, T. & Jaroszczyk, T. (1990): "Theoretical-Experimental Aerosol Filtration Model For Fibrous Filters At Intermediate Reynolds Numbers," *Proceedings of the Fifth World Filtration Congress*, Nice , France, pp. 566-572.
- Ramarao, B.V., Tien, C., & Mohan, S. (1994): "Calculation of Single Fiber Efficiencies for Interception and Impaction with Superposed Brownian Motion," *Journal of Aerosol Science*, Vol. 25, No. 2, pp. 295-313.
- Rao, N. & Faghri, M. (1988): "Computer Modeling of Aerosol Filtration by Fibrous Filters," *Aerosol Science and Technology*, vol. 8, pp. 133-156.

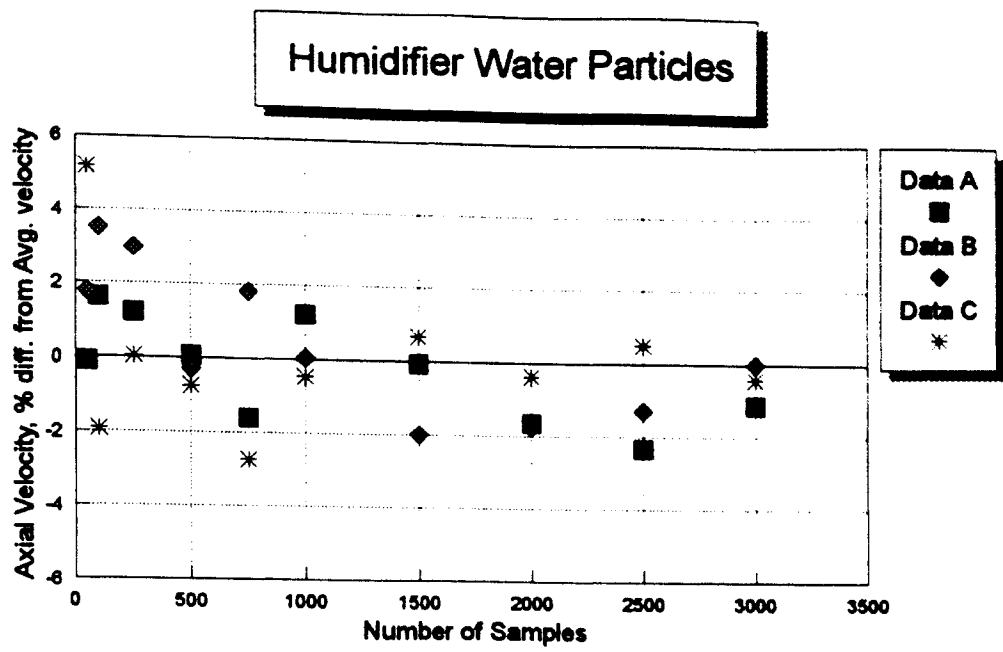
- Rodman, C.A. & Lessmann, R.C. (1988): "Automotive nonwoven filter media: their constructions and filter mechanisms," *TAPPI Journal*, April, pp. 161-168.
- Sabnis, R.D. (1993): "Effects of Non-Uniform Air Flow Through Filters On Filtration Efficiency," M.S. Thesis, Oklahoma State University, Department of Mechanical and Aerospace Engineering, Stillwater, OK.
- Sabnis, R.D., Cai, Q., & Chambers, F.W. (1994a): "Diagnosis of The Flow Fields in a Housing for Automotive Air Filter Performance Testing," American Institute of Aeronautics and Astronautics, 32nd Aerospace Sciences Meeting & Exhibit, Reno, NV, AIAA 94-0117.
- Sabnis, R.D., Cai, Q., & Chambers, F.W. (1994b): "Flow Distribution Effects Upon Air Filter Performance Measurements," Society of Automotive Engineers, Climate Control and Automotive Cabin Air Filtration (SP-1040), pp. 1-12, SAE Paper 940317.
- Seyfert, N. (1988): "Collection, Bouncing, and Adhesion on Crossed Fibers in Mono- and Multilayer Design," *Aerosol Science and Technology*, Vol. 9, pp. 201-212.
- Society of Automotive Engineers (1987): "Air Cleaner Test Code," (J726).
- Suneja, S.K. & Lee, C.H. (1973): "Aerosol Filtration by Fibrous Filters at Intermediate Reynolds Numbers (≤ 100)", *Atmospheric Environment*, Vol. 8, pp. 1081-1094.
- Taborek, J. (1984): "International System of Units (SI): Rules, Practices and Conversion Charts," Heat Exchanger Design Handbook, Hemisphere Publishing Company.
- Thom, A. (1933): "The Flow Past Circular Cylinders at Low Speeds," *Proceedings of the Royal Society of London*, Vol. A141, pp. 651-669.
- Tyyska, S. (1994): AC Delco Systems, August 5, personal communication, Flint MI.
- White, F.M. (1991): Viscous Fluid Flow, McGraw-Hill, Inc., New York, 2nd ed.
- White, P.A.F., & Smith, S.E. (1964): High-Efficiency Air Filtration, Butterworth & Co., London.
- Zimon, A.D. (1982): Adhesion of Dust and Powder, Consultants Bureau, New York, 2nd Ed.

APPENDIX A

COMPARISON OF AEROSOL PARTICLE GENERATION TECHNIQUES AND NUMBER OF SAMPLES PER RUN

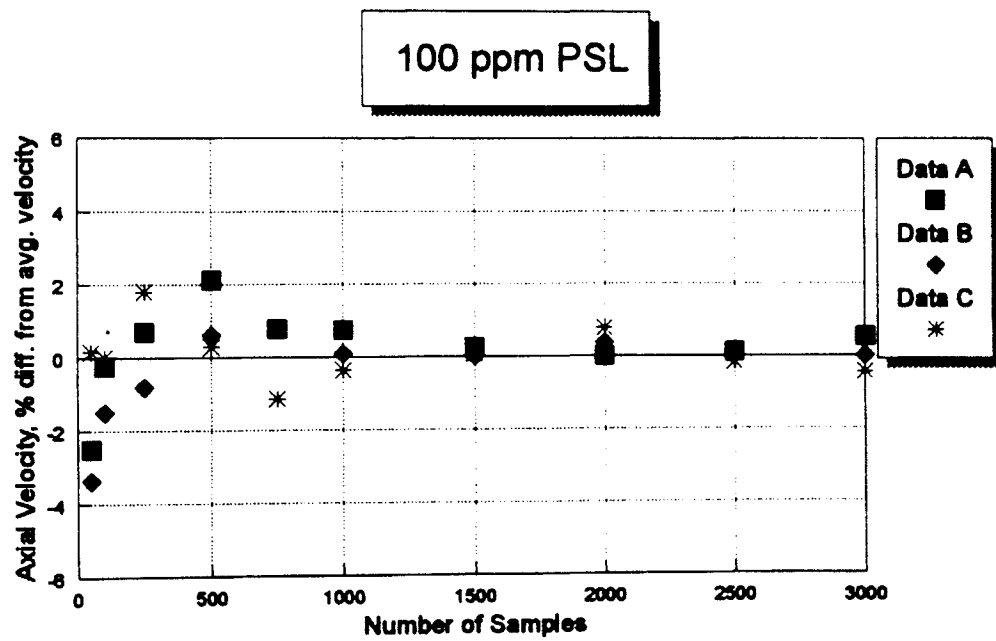
Before actual measurements of the flow field in the prototype housing were attempted several different aerosol particle generation techniques were tested to determine what method would produce the most reliable results. At the same time different number of samples per data point were tried to determine how many samples were required to produce a valid sample. As seen in Fig. A.1 the use of two ultrasonic humidifiers to produce sample particles gave only marginal results. At greater than 3000 samples per data point the repeatability of the data is still only within $\pm 2\%$ of the average velocity. By comparison, tests run with $0.966 \mu\text{m}$ polystyrene latex (PSL) microspheres, as shown in Fig. A.2 and Fig. A.3, produced data within $\pm 1\%$ of the average velocity at only 1000 samples per data point. The choice to use PSL particle was made using this data.

Comparing Fig. A.2 and Fig. A.3 shows that 200 ppm suspensions of PSL particles provided better repeatability than 100 ppm suspensions of PSL particles. The use of 200 ppm suspensions also made the time required to obtain a 1000 sample data point more bearable at 2 to 3 minutes per point. We chose to use a 1000 sample data point because this appeared to be the least number of points that could be used and still obtain a reliable run.



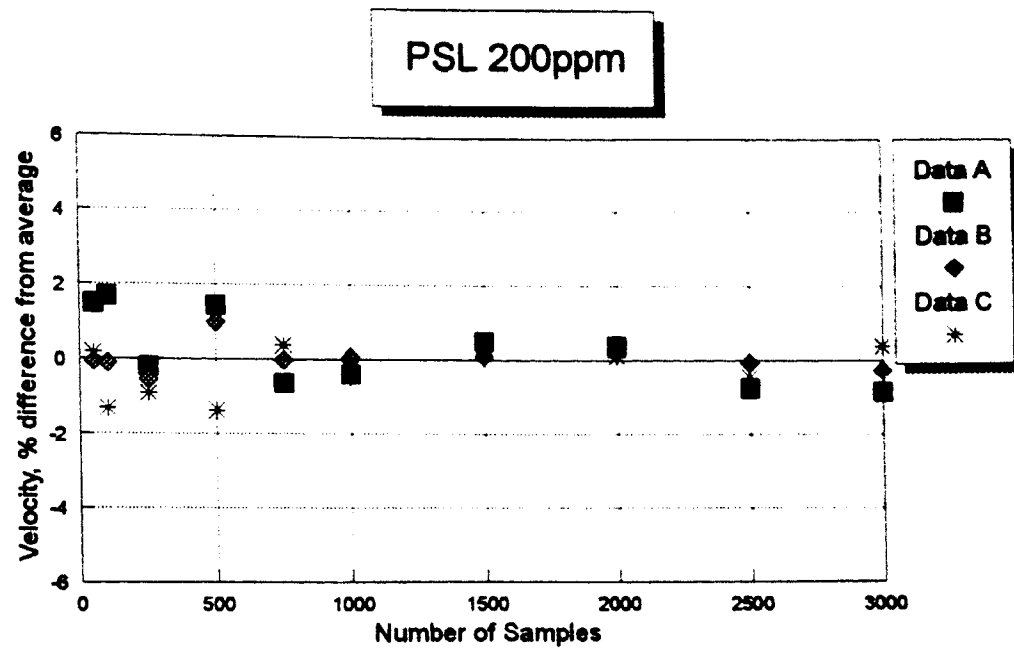
Average Velocity = 2.422

Fig. A.1 Reliability of data, prototype housing, 13 mm upstream of center of the filter, using 2 ultrasonic humidifiers as particle generators



Average Velocity = 2.450

Fig. A.2 Reliability of data, prototype housing, 13 mm upstream of center of the filter, using TSI atomizer loaded with 100 ppm PSL suspension as particle generator



Average Velocity = 2.450

Fig. A.3 Reliability of data, prototype housing, 13 mm upstream of center of the filter, using TSI atomizer loaded with 200 ppm PSL suspension as particle generator

APPENDIX B

SYMMETRY OF VELOCITY PROFILES IN THE PROTOTYPE HOUSING AND ITS RELATIONSHIP TO FILTER PLEAT CURVATURE AND HOUSING EXIT LOCATION

Before measuring the entire flow field inside the prototype housing several tests were performed to determine if the exit location of the housing or the curvature of pleats in the filter had an effect on the symmetry of velocity profiles on the upstream side of the filter. Measurements were taken with a new filter along the y-centerline of the prototype housing 13 mm upstream of the filter. The filter was then turned around in the housing and another set of velocity measurements were taken. This test was then repeated using another filter. Fig. B.1 illustrates the results of these tests. With the filter placed such that the concave side of the pleat curvature pointed towards the right and the exit was situated on the right side, "Run A" was measured. The filter was then turned around so that the concave side of the pleat curvature pointed towards the left side of the test housing with the exit still situated on the left side of the housing to measure "Run B." As can be seen in Fig. B.1 the asymmetrical hump on the right side of run A is on the left side of run B. By reversing the run B data it can be seen that the two runs are now more similar in their asymmetry. Judging from this data I have decided that what asymmetry there is in the measurements is caused mainly by the curvature of the filter pleats. All subsequent measurements were taken with the concave side of the pleat curvature always pointing toward the left end of the test housing.

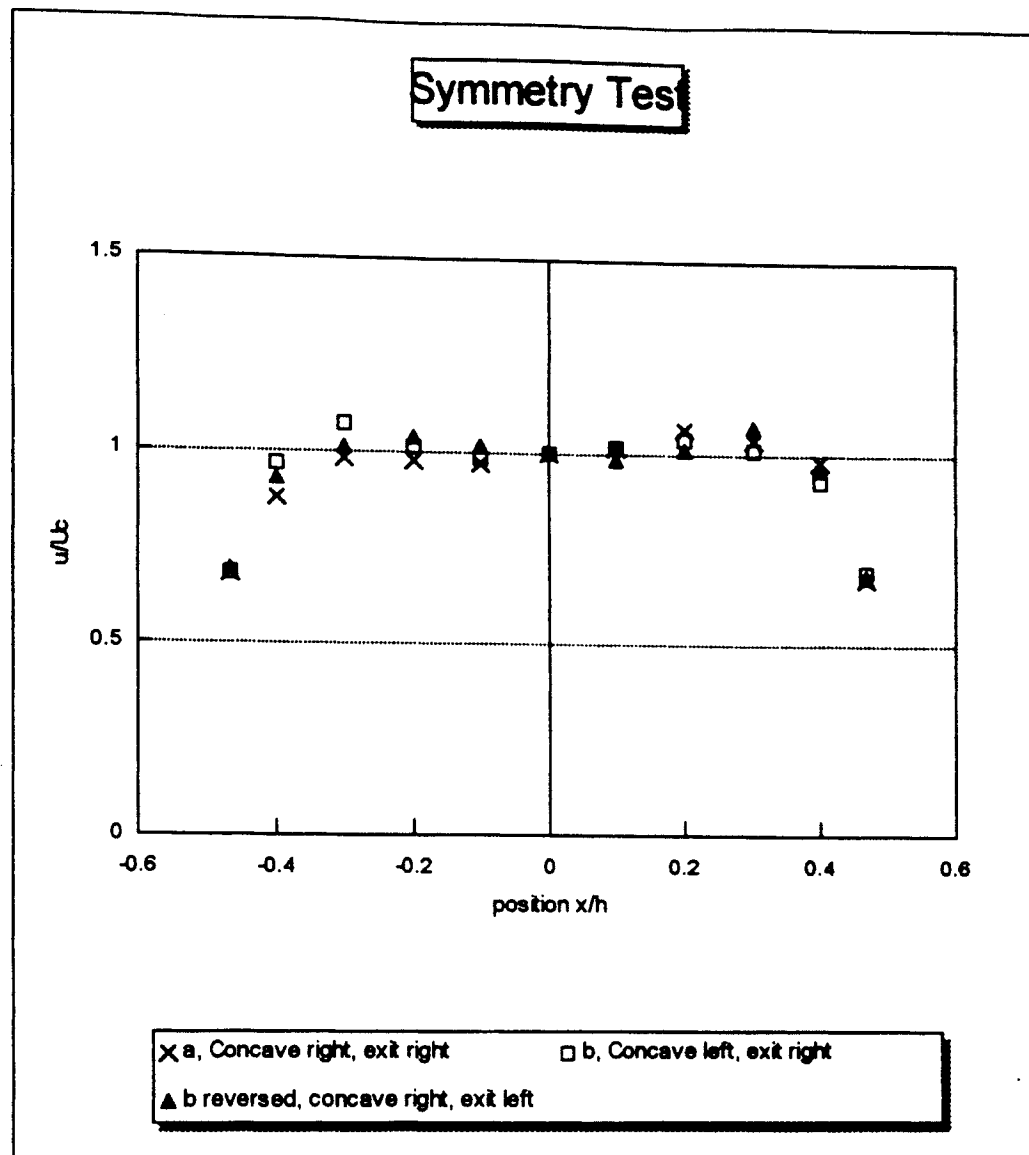


Fig. B.1 Symmetry of data, 200 ppm PSL suspension, TSI atomizer, y-centerline prototype housing, 13 mm upstream of filter

APPENDIX C

COMPUTER PROGRAM FOR THE CALCULATION OF FIBROUS FILTER PARTICLE COLLECTION EFFICIENCIES

This program was written using Borland Turbo C++ v. 3.1 and is based on a similar program found in Sabnis (1993).

```

#include <stdio.h>
#include <math.h>
#include <string.h>
#include <stdlib.h>

#define L1 13.970
#define L2 14.605
#define L3 19.050
#define W1 7.9375
#define W2 7.9375
#define W3 12.700

#define C 0.23 /* packing density */
#define RHO 2723.0 /* particle density (kg/m^3)*/
#define RHOA 1.1374 /* air density (kg/m^3)*/
#define MU 1.837e-5 /* air viscosity (Pa*s) */
#define R 19e-6 /* fiber radius (m) */
#define H 0.0007 /* filter bed thickness (m) */
#define A 0.5e-6 /* particle radius (m) */
#define WF 0.121 /* width of filter pleat (m) */
#define HF 0.03 /* height of filter pleat (m) */
#define PF 0.003125 /* pitch of filter pleat (m) */
#define LAMBDA 6.96e-8 /* mean free path of air (m)*/
#define T 298.15 /* air temperature (K) */
#define K 1.380658e-23 /* Boltzman constant */

#define AAPLAN0
#define SABNIS 1
#define UNIV 2

void Sabnis(double v2, double *efri, double *st, double *eri, double a, double y);
void Sabnis1(double v2, double *efri, double *st, double *eri, double a, double y);
void Landahl(double v2, double *efri, double *st, double *eri, double a);
void Ptak(double v2, double *efri, double *st, double *eri, double a);
void Lee(double v2, double *efri, double *st, double *eri, double a);
void Liu(double v2, double *efri, double *st, double *eri, double a);
void Suneja(double v2, double *efri, double *st, double *eri, double a);
double area12(int *j, int *k, int fl1, double *dx);
void readdata(int fl1, double a);
void stokesdata(int j);

void main(void)
{
    int i,j;

```

```

double a;

for(j=0;j<4;j++)
{
  switch(j)
  {
    case 0 : a=0.50e-6;break;
    case 1 : a=1.25e-6;break;
    case 2 : a=2.50e-6;break;
    case 3 : a=4.6e-6;break;
  }
  for(i=0;i<4;i++)
  {
    realdata(i,a);
  }
}
}
void realdata(int fl1,double a)
{
  int    i=1,j=1,k=1;
  int    dec,sign;
  double v2,x,y;           /* measured aerosol velocity, x-location, y-loc. */
  double area,v2avg;      /* elemental area, average velocity */
  double qtotal=0,qcfm;   /* total flow rate */
  double atotal=0,pen;    /* total area, elemental penetration */
  double pentotal=0,efftotal; /* total penetration, overall efficiency */
  double efri,st,eri,dx;  /* elemental eff., stokes #, fiber eff., width of el. */

  FILE   *in,*out;        /* input, output */
  char   string[80],*bb;
  char   fin[11],fout[11],*fl=fin;

  bb = (char *) malloc(10);

  fl = (char *) malloc(10);

  switch(fl1)             /* use different file names for uniform, J726, and */
                          /* prototype measured velocity profile input names */
  {
    case UNIV      : strcpy(fin,"univ2.txt");
                    strcpy(fout,"uni");
                    break;
    case SABNIS   : strcpy(fin,"sab1.txt");
                    strcpy(fout,"sab");
                    break;
    case AAPLAN   : strcpy(fin,"aaplanv2.txt");
                    strcpy(fout,"aap");
                    break;
    default      : strcpy(fin,"aaplanv2.txt");
                    strcpy(fout,"reen");
                    break;
  }

  in = fopen(fin,"rt");   /* open input file */

  bb = ecvt(2*a,3,&dec,&sign);
  strcat(bb,".txt");
  strcat(fout,bb);

  out = fopen(fout,"wt"); /* open output file */

```

```

fprintf(out, "%4s%8s%7s%7s%7s%7s%8s%7s\n", /* print headers */
"run", "vel.", "x", "y", "area", "efri", "Stc", "Eri");

while(fl!=NULL)
{
fl=fgets(string,80,in); /* read data file */
if(fl==NULL) break;
sscanf(string, "%lf%lf%lf", &v2, &x, &y); /* scan for data */

area = area12(&j, &k, fl1, &dx); /* area of given element (m^2) */
if(fl1==SABNIS) area*=2; /* area of sabnis el. doubled due to symmetry */

qtotal += v2*area*0.00006; /* total flow rate (m^3/m) */
atotal += area; /* total area (m^2) */

switch(fl1)
{
case AAPLAN : Sabnis(v2, &efri, &st, &eri, a, dx); /* sabnis' efficiency subprogram */
break;
case SABNIS : Sabnis(v2, &efri, &st, &eri, a, dx);
break;
case UNIV : Sabnis(v2, &efri, &st, &eri, a, dx);
break;
default : Sabnis1(v2, &efri, &st, &eri, a, dx);
break;
}

pen = (1-efri)*area*v2*0.00006; /* elemental penetration */

pentotal += pen; /* total penetration */

v2avg += v2; /* used to compute average velocity */

j++;
fprintf(out, "%4d%8.5f%7.2f%7.2f%7.4f%8.3f%7.4f\n",
i, v2, x, y, area, efri, st, eri);

i++;
}

v2avg /= i; /* average velocity */

qcfm = qtotal/0.028317; /* total flow rate */
efftotal = 1-(pentotal/qtotal); /* overall efficiency */

atotal /= 645.16;

fprintf(out, "%s%7.3f%s %7.3f%s\n", "Flow Rate == ", qtotal, " m^3/m", qcfm,
" cfm");

fprintf(out, "%s%10.8f%s\n", "Partical Radius == ", a/1e-6, " m");

fprintf(out, "%s%10.8f%s\n", "Partical Diameter == ", 2*a/1e-6, " um");
fprintf(out, "%s%10.8f%s\n", "Fiber Diameter == ", 2*R/1e-6, " um");
fprintf(out, "%s%5.3f%s\n", "Interception Parameter == ", a/R, " ");

```



```

fprintf(out, "r%%8.3f%%s", "Area == ", atotal, " in^2");
fprintf(out, "r%%8.3f%%s", "Avg. Velocity == ", v2avg, " m/s");
fprintf(out, "r%%8.6f%%s", "Filtration Efficiency == ", efftotal, " ");

printf("r%%8.6f%%s", "Filtration Efficiency == ", efftotal, " ");

fclose(out);
fclose(in);
}

double area12(int *j, int *k, int fl1, double *dx)          /* computes elemental areas */
{
    double area, ac1, ac2, al1, aw1, aw2, an1;
    double sac, sal, saw, san;

    ac1    = W1*L1;
    ac2 = W1*L2;
    al1 = W1*L3;
    aw1 = W3*L1;
    aw2 = W3*L2;
    an1 = W3*L3;

    sac = 0.11875*0.375;
    sal = 0.11875*0.75;
    saw = 0.2375*0.375;
    san = 0.2375*0.75;

    sac *= 645.16; sal *= 645.16; saw *= 645.16; san *= 645.16;

    if(fl1==AAPLAN)          /* prototype housing */
    {
        if((*k<3)||(*k>9))
        {
            switch(*j)
            {
                case 1 : area = ac1; *dx=W1; break;
                case 2 : area = ac2; *dx=W1; break;
                case 10 : area = ac2; *dx=W1; break;
                case 11 : area = ac1; *dx=W1; *j=0; *k=*k+1; break;
                default : area = al1; *dx=W1;
            }
        }
        else
        {
            switch(*j)
            {
                case 1 : area = aw1; *dx=W3; break;
                case 2 : area = aw2; *dx=W3; break;
                case 10 : area = aw2; *dx=W3; break;
                case 11 : area = aw1; *dx=W3; *j=0; *k=*k+1; break;
                default : area = an1; *dx=W3;
            }
        }
    }
    else                    /* J726 housing */
    {
        if((*k<2)||(*k>10))
        {

```

```

switch(*j)
{
    case 1 : area = sac;*dx=0.11875*25.4;break;
    case 11 : area = sac;*dx=0.11875*25.4;*j=0;*k=*k+1;break;
    default : area = sal;*dx=0.11875*25.4;
}
}
else
{
    switch(*j)
    {
        case 1 : area = saw;*dx=0.2375*25.4;break;
        case 11 : area = saw;*dx=0.2375*25.4;*j=0;*k=*k+1;break;
        default : area = san;*dx=0.2375*25.4;
    }
}
}
return area;
}

void Sabnis(double v2,double *efri,double *st,double *eri,double a,double y) /* Eq. (1.42) */
{
    double c,r,h,ip,hf,pf,kn,cc;
    double k,vip,er,ei;

    c = C;
    r = R;

    h = H;
    hf = HF;
    pf = PF;

    ip = a/r; /* interception parameter */
    kn = LAMBDA/a; /* knudson number */
    cc = 1.0+1.257*kn; /* slip correction factor */
    k = -0.5*log(c)-0.75+c-0.25*c*c; /* kuwabara hydrodynamic factor */

    vip = v2*y/sqrt(pow(2*hf*y/pf,2)+pow(y,2)); /* velocity inside pleat */
    vip /= 1-c;

    *st = pow(a,2)*RHO; /* stokes number */
    *st *= vip;
    *st *= cc;
    *st /= 9.0*MU*r;

    er = (1-c)/k*ip*ip/(1+ip); /* interception efficiency */

    ei = pow(*st,3)/(pow(*st,3)+0.77*pow(*st,2)+0.22); /* impaction eff. */

    *eri = 1-((1-er)*(1-ei)); /* fiber efficiency */

    *efri = -2*c*(er)*h; /* elemental efficiency */
    *efri/= M_PI*(1-c)*r;
    *efri = 1-exp(*efri);
}

void Sabnis1(double v2,double *efri,double *st,double *eri,double a,double y) /* Eq. (1.42) w/ Eq. (1.52) */
{
    double c,r,h,ip,hf,pf,kn,cc;
    double k,vip,er,ei,yo,Rep;

    c = C;

```

```

r = R;

h = H;
hf = HF;
pf = PF;

ip = a/r;
kn = LAMBDA/a;
cc = 1.0+1.257*kn;
k = -0.5*log(c)-0.75+c-0.25*c*c;

vip = v2*y/sqrt(pow(2*hf*y/pf,2)+pow(y,2));
vip /= 1-c;

*st = pow(a,2)*RHO;
*st *= vip;
*st *= cc;
*st /= 9.0*MU*r;

Rep = RHO*vip*a*2/MU;
yo = 190.0/(pow(*st+Rep,0.68)+190);

er = (1-c)/k*ip*ip/(1+ip);

ei = pow(*st,3)/(pow(*st,3)+0.77*pow(*st,2)+0.22);

*eri = 1-((1-er)*(1-ei));
*eri *= yo; /* adhesive probability */

*efri = -2*c*(1-er)*h;
*efri/= M_PI*(1-c)*r;
*efri = 1-exp(*efri);
}

void Landahl(double v2,double *efri,double *st,double *eri,double a) /* Eq. (1.38) */
{
double c,r,h,hf,pf,kn,cc;
double vip;

c = C;
r = R;

h = H;
hf = HF;
pf = PF;

kn = LAMBDA/a;
cc = 1.0+1.257*kn;

vip = v2*pf/(2*hf);
vip /= 1-c;

*st = pow(a,2)*RHO;
*st *= vip;
*st *= cc;
*st /= 9.0*MU*r;

*eri = pow(*st,3)/(pow(*st,3)+0.77*pow(*st,2)+0.22); /* impaction eff. */

*efri = -2*c*(1-er)*h;
*efri/= M_PI*(1-c)*r;
}

```

```

    *efri = 1-exp(*efri);
}

void Ptak(double v2,double *efri,double *st,double *eri,double a) /* Eq. (1.40) */
{
    double c,r,h,ip,hf,pf,kn,cc;
    double vip,er,ei;
    double Re,Rep,dummy;
    double fc,yo,ko;

    c = C;
    r = R;

    h = H;
    hf = HF;
    pf = PF;

    ip = a/r;
    kn = LAMBDA/a;
    cc = 1.0+1.257*kn;

    vip = v2*pf/(2*hf);
    vip /= 1-c;

    Re = RHOA*vip*r*2/MU; /* fiber reynolds number */
    Rep = RHO*vip*a*2/MU; /* particle reynolds number */

    fc = 0.9/pow(c,0.3); /* interference coeff. */
    yo = 190.0/(pow((*st+Rep),0.68)+190); /* adhesive probability */
    ko = 0.53; /* filter inhomogeneity coeff. */

    *st = pow(a,2)*RHO;
    *st *= vip;
    *st *= cc;
    *st /= 9.0*MU*r;

    dummy = *st-0.75*pow(Re,-0.2);
    *eri = pow(dummy,2);
    dummy = *st+0.4;
    *eri /= pow(dummy,2);
    *eri += pow(ip,2); /* fiber efficiency */
    *eri *= fc*yo*ko;

    *efri = -2*c*(*eri)*h;
    *efri/= M_PI*(1-c)*r; /* elemental efficiency */
    *efri = 1-exp(*efri);
}

void Lee(double v2,double *efri,double *st,double *eri,double a) /* Eq. (1.21) */
{
    double c,r,h,ip,hf,pf,kn,cc;
    double k,vip,er,ei;

    c = C;
    r = R;

    h = H;
    hf = HF;
    pf = PF;

    ip = a/r;

```

```

kn = LAMBDA/a;
cc = 1.0+1.257*kn;
k = -0.5*log(c)-0.75+c-0.25*c*c;

vip = v2*pf/(2*hf);
vip /= 1-c;

*st = pow(a,2)*RHO;
*st *= vip;
*st *= cc;
*st /= 9.0*MU*r;

*eri = (1-c)/k*ip*ip/(1+ip);

*efri = -2*c*(*eri)*h;
*efri/= M_PI*(1-c)*r;
*efri = 1-exp(*efri);
}

void Suneja(double v2,double *efri,double *st,double *eri,double a) /* Eq. (1.39) */
{
double c,r,h,ip,hf,pf,kn,cc;
double vip,er,ei;
double Re,dummy;

c = C;
r = R;

h = H;
hf = HF;
pf = PF;

ip = a/r;
kn = LAMBDA/a;
cc = 1.0+1.257*kn;

vip = v2*pf/(2*hf);
vip /= 1-c;

Re = RHOA*vip*r*2/MU;

*st = pow(a,2)*RHO;
*st *= vip;
*st *= cc;
*st /= 9.0*MU*r;

dummy = (1.53-0.23*log(Re)+0.0167*pow(log(Re),2));
dummy/= (*st);
dummy+= 1;
*eri = 1/pow(dummy,2);
*eri += (2/3)*(ip/*st);

*efri = -2*c*(*eri)*h;
*efri/= M_PI*(1-c)*r;
*efri = 1-exp(*efri);
}

```

APPENDIX D**FILTER SPECIFICATIONS**

Table D.1 Filter specifications

Description	units	AF3192
Length of filter	mm	193
Width of filter	mm	121
Height of pleat	mm	30
Pitch of pleat	mm	3.125
Approx. mean fiber diameter	μm	39
Approx. packing density		0.23

APPENDIX E

TEST DUST SPECIFICATIONS

SAE J726 specifies the use of AC fine and AC course dust in test conducted under the test code.

Table E.1 Test dust specifications, particle size distribution by volume

Size, μm	Fine grade (% less than)	Course grade (% less than)
5.5	38 \pm 3	38 \pm 3
11	54 \pm 3	24 \pm 3
22	71 \pm 3	37 \pm 3
44	89 \pm 3	56 \pm 3
88	97 \pm 3	84 \pm 3
125	100	100

Table E.2 Test dust specifications, particle size distribution by weight

Size, μm	Fine grade (% less than)	Course grade (% less than)
0 - 5	39 \pm 2	12 \pm 2
5 - 10	18 \pm 3	12 \pm 3
10 - 20	16 \pm 3	14 \pm 3
20 - 40	18 \pm 3	23 \pm 3
40 - 80	9 \pm 3	30 \pm 3
80 - 200	—	9 \pm 3

VITA

Robert A. Newman

Candidate for the Degree of

Master of Science

**Thesis: UNIFORMITY OF AIRFLOW IN AUTOMOTIVE FILTER TEST HOUSINGS
AND ITS EFFECTS ON THE EFFICIENCY OF FIBROUS FILTERS**

Major Field: Mechanical Engineering

Biographical:

Personal Data: Born in Stillwater, Oklahoma, June 24, 1966, the son of Robert A. Newman, CPA and Pat Newman

Education: Graduated from Stevens High School, Rapid City, South Dakota, in June 1984; received Bachelor of Science degree in Mechanical Engineering from Oklahoma State University, Stillwater, Oklahoma in May 1990. Completed the requirements for the Master of Science degree with a major in Mechanical Engineering at Oklahoma State University in December 1994.

Experience: Employed by AC Delco Systems, Flint, Michigan, from July 1994 to present as an associate engineer in the air induction systems engineering group; employed by Oklahoma State University from June 1993 to July 1994 as a graduate research assistant and a graduate teaching assistant; employed by the Archer Daniels Midland Company, North Kansas City, Missouri from June 1990 to August 1992 as a project/process engineer in an oilseed solvent extraction plant; employed by John Frick, Morrison, Oklahoma, from June 1980 to May 1990 as a farm laborer.

Professional Memberships: American Society of Mechanical Engineers, Society of Automotive Engineers.